

BOUNDS ON LARGE EXTRA DIMENSIONS FROM THE
SIMULATION OF BLACK HOLE EVENTS AT THE LARGE
HADRON COLLIDER

by

SHAOQI HOU

BENJAMIN C. HARMS, COMMITTEE CHAIR

MARCO CAVAGLIÀ

NOBUCHIKA OKADA

PAOLO RUMERIO

JEREMY BAILIN

A DISSERTATION

Submitted in partial fulfillment of the requirements
for the degree of Doctor of Philosophy
in the Department of Physics and Astronomy
in the Graduate School of
The University of Alabama

TUSCALOOSA, ALABAMA

2016

Copyright Shaoqi Hou 2016
ALL RIGHTS RESERVED

Dedication

To my family

Therefore, in the system of the Yì,
there is the Grand Terminus,
which produced the two elementary Forms.
Those two Forms produced the Four emblematic Symbols,
which again produced the eight Trigrams.
The eight Trigrams served to determine the good and evil issues of events,
and from this determination was produced
the successful prosecution of the great business of life.

from

I Ching

(Translated by James Legge, *The Yi King*. In *Sacred Books of the East*, vol. XVI. 2nd
edition (1899), Oxford: Clarendon Press)

Abstract

Large extra dimensions were originally proposed to solve the hierarchy problem of the Standard Model (SM) of elementary particle physics. The presence of large extra dimensions dilutes gravity, lowering the Planck scale, while SM particles are required to propagate only in the usual 4 dimensional spacetime, leaving the electroweak scale unchanged. If large extra dimensions exist and they are large enough, the Planck scale may be as low as a few TeV's, so that the hierarchy problem is solved. A smaller Planck scale will bring about numerous phenomenological consequences; in particular, microscopic black holes may be produced in high-energy particle collisions at this energy scale. The decay of black holes, via the Hawking effect, into elementary particles enables the detection of the black hole events, which can be used to infer the existence of large extra dimensions. In this work, we simulate microscopic black hole formation at the Large Hadron Collider with the black hole event generator CATFISH, and compare the simulation results with the experimental data published by the Compact Muon Solenoid collaboration in 2013 at a center of mass energy $\sqrt{s} = 8$ TeV, corresponding to an integrated luminosity of 12.1 fb^{-1} . The goal of this work is to test the large extra dimension model and to determine the value of the Planck scale if large extra dimensions exist. The absence of observed black hole events in the experimental data allows us to set lower bounds on the Planck scale and various parameters related to microscopic black hole formation for a number (3 - 6) of large extra dimensions. Assuming no energy loss during high-energy particle collisions, our analysis sets lower bounds on the fundamental Planck scale ranging from 0.8 TeV to 4.9 TeV for black holes fully decaying into SM particles and 0.5 TeV to 3.0

TeV for black holes settling down to a charge neutral, invisible remnant, depending on the minimum allowed black hole mass at formation. Formation of black holes with mass less than 5.2 TeV to 6.5 TeV (SM decay) and 2.2 TeV to 4.0 TeV (remnant) is excluded at 95% C.L. Further investigation takes into account the effects of the Generalized Uncertainty Principle (GUP), which is expected to play an important role because the mass of a microscopic black hole is only a few fundamental Planck masses. An analysis similar to the one carried out without including GUP effects reveals smaller lower bounds on the fundamental Planck scale ranging from 0.8 TeV to 1.4 TeV for black holes fully decaying into SM particles, only when $\alpha \geq 0.9$, depending on the minimum allowed black hole mass at formation. Therefore, this work constrains not only the sizes of the large extra dimensions and the masses of the microscopic black holes, but also sets the lower limits on the energy scale where the effects of quantum gravity start to become significant.

List of Abbreviations and Symbols

c	The speed of light in the vacuum
CERN	Conseil Européen pour la Recherche Nucléaire
LHC	Large Hadron Collider
GR	General Relativity
SM	Standard Model
BH	Black Hole
PDF	Parton Distribution Function
TS	Trapped Surface
BD	Black Disk model
GUP	Generalized Uncertainty Principle
QCD	Quantum Chromodynamics

Acknowledgements

I wish to thank my advisor, Professor Benjamin C. Harms, for finding me this exciting project and for helping me solve the difficulties I encountered throughout my graduate study. His continuous support and encouragement have given me the confidence I needed to finish this dissertation.

I must also thank my important collaborator and also my mentor, Professor Marco Cavaglià, for providing me with CATFISH, the essential tool for this project, and for his patience when answering my many questions. His criticisms and enlightening discussions helped to bring this project to a successful conclusion.

I would like also thank the other dissertation committee members: Professor Nobuchika Okada, Professor Paolo Rumerio, and Professor Jeremy Bailin. I want also to thank Professor Harms, Professor Cavaglià and Professor Okada for writing and sending numerous recommendation letters for me to attend prestigious summer schools, and mostly importantly, to help me obtain a postdoctoral position. Thanks are due also to Professor Paolo Rumerio and Professor Conor Henderson, as CMS members, for providing useful insights during the conduct of my research. I wish to thank all my classmates and colleagues, in particular, Lei Lu, Dr. Arindam Das, Andrew Buccilli, and Roshan Koirala for enjoyable discussions in physics and for listening to my complaints whenever bugs in my computer programs frustrated me. I appreciate the help of Professor Greg Landsberg and the CMS Exotica conveners. I would like also to gratefully acknowledge RC2 [1] at the University of Alabama and to thank the Alabama Supercomputer Authority [2] for providing the computing infrastructure essential to this project.

Finally, I must thank my family for their past, present and future support, love and company.

Contents

DEDICATION	i
ABSTRACT	ii
LIST OF ABBREVIATIONS AND SYMBOLS	v
ACKNOWLEDGEMENTS	vi
CONTENTS	viii
LIST OF FIGURES	xii
1 INTRODUCTION	1
2 GENERAL RELATIVITY	3
2.1 Introduction	3
2.1.1 Metric Tensor	5
2.2 Covariant Derivative	6
2.2.1 Symmetries and Killing Vectors	8
2.2.2 Parallel transport	9
2.3 Curvature Tensor	10
2.4 Einstein's Equation	12
2.4.1 Conserved quantities in GR	13
3 STANDARD MODEL AND BEYOND	15
3.1 Particle content	15
3.2 Interactions in the SM	17
3.3 Hierarchy Problem	18

3.4	Large Extra Dimensions	20
4	BLACK HOLES	23
4.1	<i>D</i> Dimensional Static, Spherical Symmetric Black Holes	23
4.1.1	4D Schwarzschild Black Holes	23
4.1.2	Higher Dimensional Case	30
4.2	Four Laws of Black Hole Mechanics	32
4.2.1	Raychaudhuri's Equation & the 2nd Law	33
4.2.2	The 0th Law	35
4.2.3	The 1st Law	37
4.2.4	The 3rd Law	38
4.3	Black Holes in Particle Collisions	39
4.3.1	Black Hole Production	39
4.3.2	Black Hole Decay	40
5	HAWKING RADIATION	42
5.1	Unruh Effect	42
5.2	Hawking Radiation	46
5.2.1	Hawking Radiation on the Brane	48
5.2.2	Hawking Radiation in the Bulk	56
6	BLACK HOLE EVENT SIMULATION	60
6.1	CATFISH: A Black Hole Event Generator	60
6.1.1	Black Hole Production in CATFISH	61
6.1.2	Black Hole Decay in CATFISH	62
6.1.3	Some Simulation Results	65
6.1.4	Other Black Hole Event Generators	67

6.2	Lower Limits on M_* and M_{\min}	68
6.2.1	Model-Independent Cross Section Limits	69
6.2.2	Results from CATFISH	73
7	GENERALIZED UNCERTAINTY PRINCIPLE AND BLACK HOLES	86
7.1	Generalized Uncertainty Principle	86
7.1.1	Implications for Black Hole Physics	87
7.2	GUP and CATFISH	92
7.2.1	Simulating GUP Effects	93
7.2.2	Upper Bounds on α	94
7.3	Lower Bounds on M_* and M_{\min} from the GUP	97
7.3.1	Delphes: A Fast Detector Simulator	97
7.3.2	The S_T Spectra	98
7.3.3	Lower Bounds on M_* and M_{\min} for Various α 's	98
8	Conclusion	105
	REFERENCES	106
A	Differential Geometry	115
A.1	Invariant Objects: Tensors	115
A.2	Invariant Operations: Lie Derivative & Covariant Derivative	118
A.2.1	Lie Derivative	118
A.2.2	Covariant Derivative	120
B	Geodesic Congruences	123
B.1	Timelike geodesic congruence	123

List of Figures

3.1	Feynman diagrams for quantum corrections to scalar mass squared at 1-loop level. Left: Scalar loop contribution. Middle: Fermion loop contribution. Right: Gauge boson loop contribution.	19
4.1	Null geodesics in the Eddington-Finkelstein coordinates (v, r) .	27
4.2	Null geodesics in the Eddington-Finkelstein coordinates (u, r) .	28
5.1	The Rindler coordinate system (ξ, η) covers region I of the Minkowski spacetime. Region II is another copy of region I, whose coordinates are still called (ξ, η) but pointing in the opposite directions.	44
5.2	Graybody factor $\sigma_{abs}^{(s)}(\omega)$ vs energy ω at different n . $\sigma_{abs}^{(s)}(\omega)$ is actually summed over j upto the third partial waves. Color code: $n = 0$ - Blue; $n = 2$ - Brown; $n = 4$ - Red Solid; $n = 6$ - Red Dashed.	52
5.3	The power spectra for spin-0 (top left), 1/2 (top right), 1 (bottom) fields. The color code is the same as Fig.(5.2)	53
5.4	Numerical results for graybody factors for scalars (top left), fermions (top right) and gauge bosons (bottom). These are taken from Ref.[3].	54
5.5	Numerical results for power emission rates for scalars (top left), fermions (top right) and gauge bosons (bottom). These are taken from Ref.[3].	55
5.6	Graybody factors (left) and energy emission rates (right) for bulk scalar mode as functions of energy ω for different n 's. Figures are taken from Ref.[3]	57
6.1	Left: The differential cross section $d\sigma/dM_{BH}$ v.s. M_{BH} . Right: The total cross section σ v.s. M_{BH} . M_* varies from 1 TeV to 4 TeV.	62
6.2	Left: The coordinate system of the CMS detector. The beam direction is parallel or anti-parallel to the z direction. y is pointing upward and x is pointing into the center of the LHC ring. Right: The diagram showing the cone used to define the variable $Iso(\iota)$.	70

- 6.3 Figure 1 in Ref.[4]. The S_T spectra for events with (left) $N = 2$ and (right) $N \geq 2$. Observed data are depicted as points with statistical error bars; the solid line with a shaded band is the multijet background prediction from $N = 2$ fit and its systematic uncertainty. Colored histograms represent small backgrounds. Also shown are the expected BH signals for 3 parameter sets of the BlackMax nonrotating BH model. Here, $M_{\text{BH}}^{\text{min}}$ is M_{min} in Section 6.1. The bottom panels in each plot show the pull distribution (defined as (data-background)/ σ (data-background)) based on combined statistical and systematic uncertainty. For more detail, please refer to Ref.[4]. 72
- 6.4 Model-independent 95% CL cross section times acceptance (A) upper limits for counting experiments with $S_T > S_T^{\text{min}}$ as a function of S_T^{min} for events with multiplicity: (top left) $N \geq 3$, (top right) $N \geq 4$, (bottom left) $N \geq 5$, and (bottom right) $N \geq 6$. The blue solid (red dotted) lines correspond to an observed (expected) limit. The green (dark) and yellow (light) bands represent one and two standard deviations from the expected limits. Graphs are taken from Figure 6 in Ref.[4]. 74
- 6.5 Model-independent 95% CL cross section times acceptance (A) upper limits for counting experiments with $S_T > S_T^{\text{min}}$ as a function of S_T^{min} for events with multiplicity: (top left) $N \geq 7$, (top right) $N \geq 8$, (bottom left) $N \geq 9$, and (bottom right) $N \geq 10$. The blue solid (red dotted) lines correspond to an observed (expected) limit. The green (dark) and yellow (light) bands represent one and two standard deviations from the expected limits. Graphs are taken from Figure 7 in Ref.[4]. 75
- 6.6 The 95% CL lower limits on the BH mass derived from the upper 95% CL limits on cross section times branching fraction as a function of M_D for various models. The areas below each curve are excluded. Graph are taken from Figure 4 in Ref.[4]. 76
- 6.7 The S_T for events with different multiplicities. Dots represent observed spectra and the green solid lines represent the predicted background distributions, which are taken from Figure 2 in Ref.[4]. The BH signals are also shown. 77
- 6.8 The S_T for events with different multiplicities. Dots represent observed spectra and the green solid lines represent the predicted background distributions, which are taken from Figure 2 in Ref.[4]. The BH signals are also shown. 78

6.9	$\sigma(S_T > S_T^{\min}) \times A$ as a function of M_* (Upper two graphs, numbers being M_* 's chosen in units of TeV) or X_{MIN} (Lower two graphs, numbers being X_{MIN} 's) at $\text{NP} = 0$ (Left two graphs) and $\text{NP} = 4$ (Right two graphs). The model-independent 95% CL experimental upper limits for counting experiments from CMS Collaboration are also shown. The multiplicity is $N \geq 3$.	80
6.10	Simulated lower limit on M_* vs. X_{MIN} as a function of NP and $\text{NEXTRADIM} = 3$ (top left), 4(top right), 5 (bottom left), and 6 (bottom right).	82
6.11	Simulated lower limit on X_{MIN} vs. M_* as a function of NP and $\text{NEXTRADIM} = 3$ (top left), 4(top right), 5 (bottom left), and 6 (bottom right).	83
6.12	Comparison of the predictions on lower limits of M_{min} from CATFISH with those from BlackMax and CHARYBDIS2 at $\text{NEXTRADIM} = 4$ (left) and 6 (right). The results of BlackMax and CHARBDIS are extracted from Fig. 4 in Ref.[4].	84
6.13	Comparison of the predictions on lower limits of M_{min} from CATFISH with those from BlackMax and CHARYBDIS2 at $\text{NEXTRADIM} = 4$ (left) and 6 (right). The results of BlackMax and CHARBDIS are extracted from Fig.'s 8 and 10 in Ref.[5].	85
7.1	The minimal mass M_{ml} in units of M_* v.s. α for different n . The left graph is in linear scale and the right graph is in log scale.	88
7.2	The ratio T'_H/T_H varies as a function of M_{BH}/M_* and n .	90
7.3	The Ratio S'_0/S_0 as a function of n at different M_{BH}/M_* .	91
7.4	The differential cross section $\frac{d\sigma}{dM_{\text{BH}}}$ and the total cross section σ as functions of M_{BH} . Curves for $\alpha = 0.8$ (Blue ones) overlap with those for $\alpha = 0.2$ (Cyan ones) partially.	94
7.5	Maximum α_m that still allows BHs to form at $\sqrt{s} = 8$ TeV at the LHC. Marked points represent results from simulation, and are linked by dashed lines. The solid curves are predicted α_m 's according to Eq.(7.15).	96
7.6	The S_T for events with different multiplicities. Dots represent observed spectra and the green solid lines represent the predicted background distributions, which are taken from Figure 2 in Ref.[4]. The BH signals are also shown.	99
7.7	The S_T for events with different multiplicities. Dots represent observed spectra and the green solid lines represent the predicted background distributions, which are taken from Figure 2 in Ref.[4]. The BH signals are also shown.	100

7.8	$\sigma(S_T > S_T^{\min}) \times A$ as a function of M_* (Upper two graphs, numbers being M_* 's chosen in units of TeV) or X_{\min} (Lower two graphs, numbers being X_{\min} 's) at $\alpha = 0.7$ (Left two graphs) and $\alpha = 0.9$ (Right two graphs). The model-independent 95% CL experimental upper limits for counting experiments from CMS Collaboration are also shown. The multiplicity is $N \geq 3$.	101
7.9	Simulated lower limit on M_* vs. X_{\min} as a function of α , NP and NEXTRADIM = 4(left), and 6 (right). The limits first discussed in Section (6.2.2.2) are also shown ($\alpha = 0$).	102
7.10	Simulated lower limit on X_{\min} vs. M_* as a function of α , NP and NEXTRADIM = 4(right), and 6 (left). The limits first discussed in Section (6.2.2.2) are also shown ($\alpha = 0$).	103
7.11	Simulated lower limit on M_{\min} vs. M_* as a function of α , NP and NEXTRADIM = 4(right), and 6 (left).	103
7.12	Comparison of the predictions on lower limits of M_{\min} from CATFISH with those from BlackMax and CHARYBDIS2 at NEXTRADIM = 4 (left) and 6 (right). The results of BlackMax and CHARBDIS are extracted from Fig. 4 in Ref.[4].	104
7.13	Comparison of the predictions on lower limits of M_{\min} from CATFISH with those from BlackMax and CHARYBDIS2 at NEXTRADIM = 4 (left) and 6 (right). The results of BlackMax and CHARBDIS are extracted from Fig.'s 8 and 10 in Ref.[5].	104

1 INTRODUCTION

Quantum mechanics and relativity are the two cornerstones of modern physics. The union of quantum mechanics and special relativity gives birth to the Standard Model (SM) of elementary particle physics, which is one of the most successful theories in physics [6]. However, the SM fails to explain the *hierarchy problem*, i.e., the huge gap between the *electroweak scale* $M_{\text{EW}} \sim 1 \text{ TeV}$ and the *Planck scale* $M_{\text{Pl}} \sim 10^{16} \text{ TeV}$. One of the possible solutions to the hierarchy problem is to introduce large extra dimensions (LEDs). This makes the gravitational interaction stronger and the Planck scale, or rather, the *fundamental* Planck scale M_* , smaller. Assuming large enough extra dimensions, it is possible to make $M_* \sim 1 \text{ TeV}$ and thus hierarchy problem is solved. This is the LED model [7, 8, 9].

However, LEDs are in fact very small, compared to macroscopic lengths, in order that the usual laws of physics at the macroscopic scale are not significantly altered, which also means that it is difficult to detect LEDs at the macroscopic scale. However, the smaller Planck scale has important consequences, because it is possible to observe gravitational effects at high energy colliders, in particular, at CERN's Large Hadron Collider (LHC). The production of microscopic black holes (BHs) during high energy particle collisions is among various interesting gravitational effects, and their decay into elementary particles via the Hawking effect enables their observation at colliders. Therefore, it is possible to detect the existence of LEDs by detecting whether BHs are produced.

Up to now, the Compact Muon Solenoid (CMS) collaboration [10, 11, 12, 4, 13] and A Toroidal LHC ApparatuS (ATLAS) collaboration [14, 15, 5] have not

observed any BH events. Nevertheless, the CMS collaboration derived model-independent cross section limits for BH production by analyzing a data sample of proton-proton (pp) collisions at the center of mass energy $\sqrt{s} = 8$ TeV and the most recent results were published in Ref.[4]. These limits can be used to restrict the values of M_* and BH mass M_{\min} . So this dissertation reports these restrictions, i.e., lower bounds on M_* and M_{\min} .

The structure of the dissertation is the following: Chapters 2 and 3 briefly review General Relativity (GR), the SM and Beyond, and the hierarchy problem. The idea of LEDs is also discussed in detail. Chapter 4 discusses the basic properties of Schwarzschild BHs in D -dimensional spacetime in the context of GR. After the account of the four laws of BH mechanics in Chapter 4, the semi-classical treatment of Hawking radiation and its properties will be the main topic of Chapter 5. Chapter 6 is devoted to the simulation of BH events and presents bounds on M_* and M_{\min} . The models considered in this chapter assume that BHs are produced in the elastic collisions of gluons and quarks, and in their final evolution phase, they either decay into a number of elementary particles, or settle down to an invisible BH remnant. Following that, in Chapter 7, General Uncertainty Principle (GUP) is introduced and its effects on BH evaporation are discussed. Since GUP is a common implication of various quantum gravity candidates, it is expected to take place in the process of BH formation and decay. So Chapter 7 presents the simulation of BH events with GUP effects and lower limits on M_* and M_{\min} . The lower bounds on M_* and X_{\min} (or equivalently, M_{\min}) presented in Chapters 6 and 7 are the original work.

The natural units ($\hbar = c = k_B = 1$) is used in this dissertation.

2 GENERAL RELATIVITY

A black hole (BH) is a spacetime region from which even light cannot escape. Although using Newtonian gravitational theory, the size of a BH can be determined by equating the first escape speed to c , and it is exactly equal to the one obtained using General Relativity (GR), to fully understand BH physics, GR is required. In this chapter, the basic concepts of GR will be briefly discussed to set the conventions used for this dissertation. The emphasis focuses on the differences between physics in a flat spacetime and physics in a general, especially curved, spacetime. New mathematical concepts (e.g., covariant derivatives and geodesics) are constructed to make the laws of physics independent of the choice of reference frames, while other quantities (e.g., Riemann tensor and Ricci tensor/scalar) characterize curved spacetime. Finally, Einstein's equation is written down, to which a BH is one of the solutions. The discussion tends to be more general, and the spacetime is assumed to be D -dimensional with $D \geq 4$, although some specific examples use 4-dimensional spacetime. In addition, Section 2.4 assumes 4-dimensional spacetime, since the Einstein's equation was originally written for a 4-dimensional spacetime [16]. The generalization of results in 4-dimensional spacetime to higher dimensional spacetime is straightforward.

This chapter is based on the Ref.'s [17, 18].

2.1 Introduction

GR describes gravity as the manifestation of spacetime curvature. It has two basic principles: 1) *General covariance* states that all laws of physics take the same forms for different observers; 2) The *Equivalence principle* states that in a

small enough region of spacetime, the laws of physics reduce to those of special relativity. The departure from special relativity is attributed to gravity, and the principle of general covariance relates observations made in one reference frame to those made in other reference frames. These two principles are accurately captured by describing the spacetime as a Lorentzian manifold, which locally looks like flat spacetime, i.e., Minkowski spacetime. A metric is also an essential ingredient and can be diagonalized into the form of $\text{diag}(-1, 1, \dots, 1)$ (there are $D - 1$ ones for a D dimensional spacetime).

Physical quantities appearing in the laws of physics are various types of tensors, which are scalars, vectors, dual vectors and general types of tensors. These all satisfy distinct transformation rules under the exchange of coordinates $x^\mu \rightarrow y^\mu$, $\mu = 0, 1, \dots, D - 1$. The simplest tensors defined on a manifold are scalars $f(x)$, which does not change under coordinate transformations, i.e.,

$$f(x) = f'(y). \quad (2.1)$$

Vectors v^μ are slightly more complicated objects, which have D components, and these components transform covariantly in the following way,

$$v'^\mu = \frac{\partial y^\mu}{\partial x^\nu} v^\nu, \quad (2.2)$$

where the Einstein Summation Rule is assumed, and v'^μ are the components in the new coordinates y^μ , so that the vector does not change under coordinate transformations. Dual vectors, also called covectors, ω_μ can be contracted with any vector v^μ to give a scalar $v^\mu \omega_\mu$. The invariance of a scalar and the covariance of vector components give rise to the transformation law of the covector,

$$\omega'_\mu = \omega_\nu \frac{\partial x^\nu}{\partial y^\mu}. \quad (2.3)$$

Generalizing the transformation laws of vectors and covectors, a general tensor $T^{\nu_1, \dots, \nu_l}_{\mu_1, \dots, \mu_k}$ transforms in the following way,

$$T^{\nu_1, \dots, \nu_l}_{\mu_1, \dots, \mu_k} = \frac{\partial x^{\rho_1}}{\partial y^{\mu_1}} \cdots \frac{\partial x^{\rho_k}}{\partial y^{\mu_k}} \frac{\partial y^{\nu_1}}{\partial x^{\sigma_1}} \cdots \frac{\partial y^{\nu_l}}{\partial x^{\sigma_l}} T^{\sigma_1, \dots, \sigma_l}_{\rho_1, \dots, \rho_k}. \quad (2.4)$$

This tensor carries k contravariant indices μ_i , $i = 1, \dots, k$ and l covariant indices ν_j , $j = 1, \dots, l$, so it is called a (k, l) type tensor. Therefore, a scalar is a $(0, 0)$ type tensor, a vector is a $(1, 0)$ type tensor, and a covector is a $(0, 1)$ type tensor.

2.1.1 Metric Tensor

A special and very important tensor is called the metric tensor $g_{\mu\nu}$ which is a nondegenerate, symmetric $(0, 2)$ type tensor. It is used to define distances: $g_{\mu\nu}v^\mu v^\nu$ is called the length squared of vector v^μ . Since $g_{\mu\nu}$ is not positive-definite, vectors can be categorized into three types: 1) Timelike vectors, whose length squared is negative; 2) Null vectors, whose length squared is zero; and 3) Spacelike vectors, whose length squared is positive. A different way to represent the metric tensor is to use the infinitesimal invariant interval squared,

$$ds^2 = g_{\mu\nu} dx^\mu dx^\nu. \quad (2.5)$$

This is also called the line element. By Eq.(2.4), the coordinate transformation law of metric components is

$$g'_{\mu\nu} = \frac{\partial x^\rho}{\partial y^\mu} \frac{\partial x^\sigma}{\partial y^\nu} g_{\rho\sigma}. \quad (2.6)$$

This transformation makes sure that the line element ds^2 is invariant.

The inverse of $g_{\mu\nu}$ is denoted as $g^{\mu\nu}$, so that

$$g_{\mu\rho} g^{\rho\nu} = \delta_\mu^\nu, \quad (2.7)$$

where the right hand side is the Kronecker symbol. The transformation law of $g^{\mu\nu}$ can be easily written down according to Eq.(2.4),

$$g'^{\mu\nu} = \frac{\partial y^\mu}{\partial x^\rho} \frac{\partial y^\nu}{\partial x^\sigma} g^{\rho\sigma}. \quad (2.8)$$

$g_{\mu\nu}$ and $g^{\mu\nu}$ can be used to lower and raise indices of tensors. For example, v^μ 's index μ can be lowered via $v_\mu = g_{\mu\nu}v^\nu$, and becomes a covector. In addition, ω_μ 's index μ can be raised, i.e., $\omega^\mu = g^{\mu\nu}\omega_\nu$ to give a vector.

For example, the metric of the 4-dimensional Minkowski spacetimes is called $\eta_{\mu\nu} = \text{diag}(-1, 1, 1, 1)$, or,

$$ds^2 = -dt^2 + dx^2 + dy^2 + dz^2, \quad (2.9)$$

in a Lorentzian coordinate system. Therefore, the Minkowski spacetime is said to be flat. In a curved spacetime, the components of a metric are functions of coordinates. However, the quantity characterizing whether a spacetime is curved or not is the Riemann tensor. To discuss it, it is necessary to introduce the concept of *covariant derivative*.

2.2 Covariant Derivative

In the Minkowski spacetime, the partial derivative $\partial_\mu v^\nu = \partial v^\nu / \partial x^\mu$ of a vector v^ν field is also a tensor, because in a different Lorentz coordinates,

$$\frac{\partial v'^\nu}{\partial y^\mu} = \frac{\partial x^\rho}{\partial y^\mu} \frac{\partial y^\nu}{\partial x^\sigma} \frac{\partial v^\sigma}{\partial x^\rho}, \quad (2.10)$$

satisfying tensor transformation rule Eq.(2.4). But in a curved spacetime, this is not necessarily true, because $\partial y^\nu / \partial x^\sigma$ also depends on coordinates,

$$\frac{\partial v'^{\nu}}{\partial y^\mu} = \frac{\partial x^\rho}{\partial y^\mu} \frac{\partial y^\nu}{\partial x^\sigma} \frac{\partial v^\sigma}{\partial x^\rho} + \frac{\partial x^\rho}{\partial y^\mu} \frac{\partial^2 y^\nu}{\partial x^\rho \partial x^\sigma} v^\sigma \quad (2.11)$$

In order to remove the second term on the right hand side of above expression, a quantity $\Gamma^\nu_{\rho\mu}$ can be introduced to define the covariant derivative in the following way,

$$\nabla_\mu v^\nu = \partial_\mu v^\nu + \Gamma^\nu_{\rho\mu} v^\rho, \quad (2.12)$$

requiring that,

$$\nabla_\mu v'^{\nu} = \frac{\partial x^\rho}{\partial y^\mu} \frac{\partial y^\nu}{\partial x^\sigma} \nabla_\rho v^\sigma. \quad (2.13)$$

Here, $\Gamma^\mu_{\nu\rho}$ are called Christoffel symbols, and are related to $g_{\mu\nu}$ via,

$$\Gamma^\rho_{\mu\nu} = \frac{1}{2} g^{\rho\sigma} (\partial_\nu g_{\sigma\mu} + \partial_\mu g_{\sigma\nu} - \partial_\sigma g_{\mu\nu}), \quad (2.14)$$

which are symmetric in exchanging μ and ν , and therefore,

$$\nabla_\rho g_{\mu\nu} = 0. \quad (2.15)$$

For a covector ω_μ , the covariant derivative is defined as

$$\nabla_\mu \omega_\nu = \partial_\mu \omega_\nu - \Gamma^\rho_{\mu\nu} \omega_\rho, \quad (2.16)$$

and the covariant derivative of a scalar $f(x)$ is the ordinary partial derivative,

$$\nabla_\mu f = \partial_\mu f. \quad (2.17)$$

Finally, the covariant derivative of an arbitrary tensor $T_{\nu_1, \dots, \nu_l}^{\mu_1, \dots, \mu_k}$ is

$$\nabla_\rho T_{\nu_1, \dots, \nu_l}^{\mu_1, \dots, \mu_k} = \partial_\rho T_{\nu_1, \dots, \nu_l}^{\mu_1, \dots, \mu_k} + \sum_{i=1}^k \Gamma^{\mu_i}_{\sigma\rho} T_{\nu_1, \dots, \nu_l}^{\mu_1, \dots, \sigma, \dots, \mu_k} - \sum_{j=1}^l \Gamma^{\sigma}_{\rho\nu_j} T_{\nu_1, \dots, \sigma, \dots, \nu_l}^{\mu_1, \dots, \mu_k}. \quad (2.18)$$

2.2.1 Symmetries and Killing Vectors

A symmetry of a spacetime manifold is a particular kind of smooth map (Appendix A.2.1.1), which preserves the metric tensor $g_{\mu\nu}$. The generator of a symmetry is called a Killing vector field χ^μ , which satisfies the following relation,

$$\nabla_\mu \chi_\nu + \nabla_\nu \chi_\mu = 0. \quad (2.19)$$

Take the symmetries in Minkowski spacetime for example. Poincaré transformations preserve the Minkowski metric $\eta_{\mu\nu}$. Translations are induced by the linear combinations of the following vector fields,

$$\chi_0 = \partial_t, \quad \chi_1 = \partial_x, \quad \chi_2 = \partial_y, \quad \chi_3 = \partial_z. \quad (2.20)$$

Lorentz transformations are induced by the linear combinations of the following vector fields,

$$\chi_{12} = y\partial_x - x\partial_y, \quad \chi_{23} = z\partial_y - y\partial_z, \quad \chi_{31} = x\partial_z - z\partial_x; \quad (2.21)$$

$$\chi_{01} = t\partial_x + x\partial_t, \quad \chi_{02} = t\partial_y + y\partial_t, \quad \chi_{03} = t\partial_z + z\partial_t. \quad (2.22)$$

Eq.(2.21) are generators of rotations, and Eq.(2.22) are generators of boosts. These 10 vector fields are all Killing vectors for the Minkowski spacetime. Therefore, the Minkowski spacetime is a maximal symmetric spacetime.

If a spacetime has a timelike Killing vector field, it is called *stationary*. Furthermore, if the Killing vector field is orthonormal to spacelike hypersurfaces,

the spacetime is said to be *static*. The Minkowski spacetime is stationary, since the Killing vector ∂_t is timelike, and static, since ∂_t is perpendicular to the constant time hypersurfaces everywhere. Curved stationary/static spacetimes will be discussed in Chapter 4.

2.2.2 Parallel transport

In the Minkowski spacetime, a parallel transported vector v^μ along a closed curve will coincide with itself. However, if the spacetime is curved, the vector v^μ will not return to its original value. This is one characteristic of a curved spacetime. In the Minkowski spacetime, parallel transport is independent of paths. However, it is nontrivial to define the parallel transport in a curved spacetime.

Let $\gamma(t)$ be a smooth curve parametrized by t , whose tangent is $v^\mu = dx^\mu/dt$, where $x^\mu(t)$ is a point along the curve. Let u^μ be another vector field, and the rate of its variation along the curve $\gamma(t)$ is

$$\nabla_v u^\mu = v^\mu \nabla_\mu u^\nu = \frac{du^\nu}{dt} + \Gamma^\nu_{\rho\mu} v^\mu dt u^\rho. \quad (2.23)$$

If $v^\mu \nabla_\mu u^\nu = 0$, u is said to be parallel transported along v . The parallel transported vector fields satisfy an important result due to Eq.(2.15) as well as Leibniz rule: $v^\mu \nabla_\mu (g_{\rho\sigma} u^\rho w^\sigma) = 0$ if u and w are both parallel transported. This result states that parallel transportation preserves the lengths and angles. A special case happens letting $u^\mu = v^\mu$, that is, v^μ is invariant along itself. $\gamma(t)$ is called a *geodesic* which satisfies the *geodesic equation*,

$$\frac{d^2 x^\mu}{dt^2} + \Gamma^\mu_{\rho\sigma} \frac{dx^\rho}{dt} \frac{dx^\sigma}{dt} = 0. \quad (2.24)$$

Geodesics are the “straight lines” in a generic manifold.

2.3 Curvature Tensor

As discussed in the last section, a parallel transported vector along a closed curve might not return to its original value. The failure of parallel transporting a vector to itself along a closed loop is measured by the curvature tensor, also known as the Riemann tensor.

To understand this point, let Σ be a 2 dimensional surface embedded in the spacetime, and it is charted by a coordinate system $\{t, s\}$. The tangent vectors to the coordinate lines are v^μ and u^μ . Let a point p in Σ be the origin of the coordinate system and suppose there is a vector w^μ at p . w^μ can be firstly parallel transported along the constant s coordinate line by a small parameter distance Δt , becoming $\tilde{w}^\mu \approx w^\mu + \nabla_v w^\mu \Delta t$. Then parallel transport it to point q along the constant t coordinate line by Δs , becoming $w'^{\mu} \approx \tilde{w}^\mu + \nabla_u \tilde{w}^\mu \Delta s \approx w^\mu + \nabla_v w^\mu \Delta t + \nabla_u w^\mu \Delta s + \nabla_u \nabla_v w^\mu \Delta t \Delta s$. w can also be parallel transported to q in the reversed order, ending with $w''^\mu \approx w^\mu + \nabla_u w^\mu \Delta s + \nabla_v w^\mu \Delta t + \nabla_v \nabla_u w^\mu \Delta s \Delta t$. The difference between w' and w'' is

$$w'^{\mu} - w''^{\mu} = (\nabla_u \nabla_v w^\mu - \nabla_v \nabla_u w^\mu) \Delta t \Delta s, \quad (2.25)$$

which is not vanishing in general. The term in the brackets characterize the difference between w'^{μ} and w''^{μ} , and defines *curvature tensor* $R_{\mu\nu\sigma}{}^{\rho}$:

$$(\nabla_\mu \nabla_\nu - \nabla_\nu \nabla_\mu) w^\rho = -R_{\mu\nu\sigma}{}^{\rho} w^\sigma. \quad (2.26)$$

The curvature tensor $R_{\mu\nu\sigma}{}^{\rho}$ has the following properties:

1. $R_{\mu\nu\rho\sigma} = -R_{\nu\mu\rho\sigma} = -R_{\mu\nu\sigma\rho} = R_{\rho\sigma\mu\nu}$, with $R_{\mu\nu\rho\sigma} = g_{\sigma\lambda} R_{\mu\nu\rho}{}^{\lambda}$;
2. $R_{\mu\nu\rho\sigma} + R_{\rho\mu\nu\sigma} + R_{\nu\rho\mu\sigma} = 0$;
3. The Bianchi identity: $\nabla_\lambda R_{\mu\nu\rho\sigma} + \nabla_\nu R_{\lambda\mu\rho\sigma} + \nabla_\mu R_{\nu\lambda\rho\sigma} = 0$.

These properties decrease the number of independent components of R to $D^2(D^2-1)/12$, so there are 20 independent components of $R_{\mu\nu\sigma}{}^\rho$ in the 4 dimensional spacetime.

Contracting ν and λ in $R_{\mu\nu\rho}{}^\lambda$ gives the symmetric *Ricci tensor* $R_{\mu\rho}$. Further contracting the remaining indices with those of $g^{\mu\rho}$ results in *Ricci scalar* R . Property 3 plays an important rule in constructing GR, because after being contracted with $g^{\lambda\rho}g^{\nu\sigma}$ and rearranged, it becomes

$$\nabla_\nu \left(R^\nu{}_\mu - \frac{1}{2} \delta_\mu^\nu R \right) = 0. \quad (2.27)$$

Einstein tensor $G_{\mu\nu}$ is thus introduced as

$$G_{\mu\nu} = R_{\mu\nu} - \frac{1}{2} g_{\mu\nu} R, \quad (2.28)$$

satisfying

$$\nabla^\nu G_{\mu\nu} = 0. \quad (2.29)$$

Eq.(2.26) also determines the Riemann tensor in terms of Christoffel symbols by replacing covariant derivatives with partial derivatives and Christoffel symbols, and the result is,

$$R_{\mu\nu\rho}{}^\sigma = \partial_\nu \Gamma^\sigma{}_{\mu\rho} - \partial_\mu \Gamma^\sigma{}_{\nu\rho} + \Gamma^\lambda{}_{\mu\rho} \Gamma^\sigma{}_{\lambda\nu} - \Gamma^\lambda{}_{\nu\rho} \Gamma^\sigma{}_{\lambda\mu}. \quad (2.30)$$

Contracting ν and σ gives the Ricci tensor,

$$R_{\mu\rho} = \partial_\nu \Gamma^\nu{}_{\mu\rho} - \partial_\mu \Gamma^\nu{}_{\nu\rho} + \Gamma^\lambda{}_{\mu\rho} \Gamma^\nu{}_{\lambda\nu} - \Gamma^\lambda{}_{\nu\rho} \Gamma^\nu{}_{\lambda\mu}. \quad (2.31)$$

2.4 Einstein's Equation

In 1905, Einstein established the foundations of GR and proposed the equation governing the interactions between matter and the gravity, i.e., *Einstein's equation*, [16]

$$G_{\mu\nu} = \frac{1}{8\pi G_4} T_{\mu\nu}. \quad (2.32)$$

On the left hand side, the spacetime geometry is encoded in $G_{\mu\nu}$. On the right hand side, G_4 is the gravitational constant, and $T_{\mu\nu}$ is the energy-momentum tensor of all matter fields, such as the electromagnetic field. So the right hand side contains the contribution to the spacetime geometry of matter. The conservation of energy $\nabla^\nu T_{\mu\nu} = 0$ is automatically satisfied by Eq.(2.29), which in turn states that the spacetime geometry influences the motion of the matter. Therefore, the spacetime geometry and the matter are intimately related via Einstein's equation.

The energy-momentum tensor takes different form depending on the type of the matter field. For an electromagnetic field, the energy momentum tensor is given by,

$$T_{\mu\nu} = F_\mu{}^\rho F_{\rho\nu} - \frac{1}{4} g_{\mu\nu} F_{\rho\sigma} F^{\rho\sigma}, \quad (2.33)$$

with $F_{\mu\nu}$ the field strength (refer to Section (3.2)), while for a perfect fluid,

$$T_{\mu\nu} = (\rho + p)U_\mu U_\nu + pg_{\mu\nu}. \quad (2.34)$$

Here, U^μ is the 4 velocity of the perfect fluid, and ρ and p are the density and pressure measured by the comoving observer with 4 velocity U^μ , respectively. There are several energy conditions imposed on $T_{\mu\nu}$, which are useful for discussion of BH mechanics in Section 4.2. Usually, these energy conditions are also expressed in terms of the energy-momentum tensor of a perfect fluid. These are (in the following, t^μ is an arbitrary timelike vector, and k^μ is an arbitrary null vector),

Weak energy condition states that $T_{\mu\nu}t^\mu t^\nu \geq 0$, or equivalently, $\rho \geq 0$ and $\rho + p \geq 0$.

Null energy condition states that $T_{\mu\nu}k^\mu k^\nu \geq 0$, or equivalently $\rho + p \geq 0$.

Dominant energy condition states that $T_{\mu\nu}t^\mu t^\nu \geq 0$ and $T^{\mu\nu}t_\nu$ is a nonspacelike vector. Equivalently, $\rho \geq |p|$.

Null dominant energy condition states that $T_{\mu\nu}k^\mu k^\nu \geq 0$ and $T^{\mu\nu}k_\nu$ is a nonspacelike vector. This implies that $\rho \geq |p|$ or $p = -\rho$.

Strong energy condition states that $T_{\mu\nu}t^\mu t^\nu > \frac{1}{2}T^\lambda{}_\lambda t^\sigma t_\sigma$, or equivalently, $\rho + p \geq 0$ and $\rho + 3p \geq 0$.

2.4.1 Conserved quantities in GR

Einstein's equation (2.32) ensures that $\nabla_\mu T^\mu{}_\nu = 0$, which states the conservation of energy, but it is not trivial to define the conserved energy and angular momentum observed by an observer with 4-velocity U^μ in a generic spacetime. However, if the spacetime has a certain symmetry, whose Killing vector field is ξ^μ , it can be shown that the vector field $T^\mu{}_\nu \xi^\nu$ gives a conserved quantity W^μ :

$$\nabla_\mu W^\mu = \nabla_\mu (T^\mu{}_\nu \xi^\nu) = T^{\mu\nu} \nabla_\mu \xi_\nu = 0, \quad (2.35)$$

since $T^{\mu\nu}$ is symmetric, but $\nabla_\mu \xi_\nu$ is antisymmetric. Integrating $\nabla_\mu W^\mu$ in a spacetime region V bounded by two spacelike, infinite hypersurfaces Σ_1, Σ_2 , whose unit normal vectors are n^μ , gives

$$\int_V \nabla_\mu W^\mu \sqrt{-g} d^4x = \int_{\Sigma_2} W^\mu n_\mu \sqrt{h} d^3x - \int_{\Sigma_1} W^\mu n_\mu \sqrt{h} d^3x = 0. \quad (2.36)$$

Here, Stoke's theorem has been used, and h is the determinant of the induced metric $h_{\mu\nu} = g_{\mu\nu} + n_\mu n_\nu$ on the hypersurfaces. From this equation, the conserved

quantity Q can be read off:

$$Q = \int_{\Sigma} T^{\mu}_{\nu} \xi^{\nu} n_{\mu} \sqrt{h} \, dx^3. \quad (2.37)$$

So for a spacetime which possess a timelike Killing χ^{μ} , the energy M can be defined,

$$M = \frac{1}{4\pi G_4} \int_K (\nabla^{\mu} \chi^{\nu}) n_{\mu} N_{\nu} \sqrt{q} \, d^2x, \quad (2.38)$$

where K is a 2 dimensional, compact spacelike surface enclosing matter, and N_{ν} is its unit normal. n_{μ} is the unit normal to a spacelike hypersurface Σ in which K is embedded. This formula is called the *Komar energy*, which is the total energy of the matter field and the BHs inside of K . Similarly, the angular momentum can be obtained via,

$$J = -\frac{1}{8\pi G_4} \int_K (\nabla^{\mu} \phi^{\nu}) n_{\mu} N_{\nu} \sqrt{q} \, d^2x. \quad (2.39)$$

If K is chosen to be at infinity, M represents the total energy of the spacetime.

If K is the horizon, J is the angular momentum of the BH and is denoted by J_H .

3 STANDARD MODEL AND BEYOND

The SM of elementary particle physics is a Quantum Field Theory (QFT) with gauge group $SU(3)_C \times SU(2)_L \times U(1)_Y$. It describes the three basic gauge interactions among particles: electromagnetic, weak and strong interactions. Although, the SM is a very successful theory [6], it suffers from some problems. One of them is the *Hierarchy Problem*. In this chapter, the SM will be briefly reviewed and the hierarchy problem is then discussed. In the final section, the ADD model, as a possible solution to the hierarchy problem, is introduced. The current experimental bounds on the sizes of the large extra dimensions are also presented.

3.1 Particle content

In QFT, particles are excitations of quantum fields, and classified according to their transformation properties. There are Higgs boson, fermions and gauge bosons, which are different representations of the Lorentz group. Fermions (and Higgs) can also be further grouped into subclasses by their transformation properties under $SU(3)_C \times SU(2)_L \times U(1)_Y$ transformations, as shown in Table.(3.1). The left-handed doublet l_L^i and right-handed e_R^i are both called lepton, which do not participate strong interactions. The index i labels generations and takes 3 values: electron type e , muon type μ and tau type τ . l_L^i consist of two particles: left-handed neutrino ν_L^i and electron e_L^i ,

$$l_L^i = \begin{pmatrix} \nu_L^i \\ e_L^i \end{pmatrix}. \quad (3.1)$$

	SU(3) _C	SU(2) _L	U(1) _Y
l_L^i	1	2	-1/2
e_R^i	1	1	-1
q_L^i	3	2	+1/6
u_R^i	3	1	+2/3
d_R^i	3	1	-1/3
H	1	2	+1/2

Table 3.1. Fermions and Higgs boson in the SM. i is the generation label, ranging from 1 to 3. This table gives the gauge quantum numbers, indicating the representations to which particles belong and in particular, the last column displays the hypercharge.

So l_L^i is a SU(2)_L doublet.

Similarly, q_L^i is also a SU(2)_L doublet,

$$q_L^i = \begin{pmatrix} u_L^i \\ d_L^i \end{pmatrix}. \quad (3.2)$$

In addition, q_L^i , u_R^i and d_R^i carry 3 different SU(3)_C colors: Red, Green and Blue. Therefore, they are SU(3)_C color triplets, called quarks. Their indices i also label generations and there are 3 generations and 6 quarks: u, d, c, s, b, t . Higgs boson H is also listed in Table (3.1) as a SU(2)_L doublet, consisting of a chargeless component H_0 and a charged one H_+ :

$$H = \begin{pmatrix} H_+ \\ H_0 \end{pmatrix}. \quad (3.3)$$

On July 4th, 2012, the CMS and ATLAS collaborations [19, 20] both discovered a new boson believed to be the Higgs boson, independently. The masses measured by the two groups are 125.3 GeV at 5.8σ and 126.0 GeV at 5.9σ , respectively.

Gauge (vector) bosons mediate interactions. Photons γ mediate electromagnetic interaction and are massless. W^\pm and Z bosons mediate weak interaction

and are massive. Finally, 8 gluons g are the mediators of strong force, and massless.

The gravitational interaction is believed to be mediated by gravitons G , the excitations of the metric tensor, whose spin is thus 2 and mass is zero. So far, it is a hypothetical particle and not included in the SM. But it is believed to exist in Nature.

3.2 Interactions in the SM

There are 4 fundamental interactions in Nature, 3 of which are described in the SM as gauge interactions. Gauge interactions arise upon the requirement of the invariance of Lagrangian $\mathcal{L}(\phi, \partial_\mu\phi)$ under local gauge transformations. To fulfill this requirement, a vector field $A_\mu(x)$ can be introduced, and the ordinary partial derivative operator ∂_μ is replaced by the covariant one,

$$\partial_\mu \rightarrow D_\mu = \partial_\mu - igA_\mu(x), \quad (3.4)$$

where g is the coupling constant. The gauge interaction is thus introduced into the theory. In the SM, there are 3 gauge potentials, namely, gluon fields $G_\mu^a(x)\frac{\lambda^a}{2}$ for SU(3), gauge fields $W_\mu^b(x)\frac{\sigma^b}{2}$ for SU(2) and $B_\mu(x)$ for U(1), where λ^a are the Gell-Mann matrices ($a = 1, \dots, 8$) and σ^b are the Pauli matrices ($b = 1, 2, 3$). The 3 gauge coupling constants are g_3 , g_2 and g_Y , respectively, so that

$$D_\mu = \partial_\mu - ig_3 G_\mu^a \frac{\lambda^a}{2} - ig_2 W_\mu^b \frac{\sigma^b}{2} - ig_Y Y B_\mu. \quad (3.5)$$

After spontaneous symmetry breaking, the gauge group SU(2)×U(1) is broken, leaving the U(1)_{EM} symmetry.

Besides gauge interactions, the SM also has Yukawa interactions, i.e., *fermion-fermion-boson* type interactions. For example, before spontaneous symmetry

breaking, Higgs doublet H couples to lepton doublet l_L^i and lepton singlet e_R^j ,

$$\mathcal{L}_Y = -Y_{eij}\bar{l}_L^i H e_R^j + \text{h.c.}, \quad (3.6)$$

where Y_{eij} are Yukawa couplings, h.c. means Hermitian conjugates, and repeated indices (i, j) imply summation over flavors. After symmetry breaking, these Yukawa terms give rise to charged lepton masses. Finally, there are Higgs self-interactions,

$$\mathcal{L}_H = -\frac{\lambda}{2}\left(|H|^2 - \frac{v^2}{2}\right)^2, \quad (3.7)$$

with λ the Higgs quartic coupling constant, and v the vacuum expectation value of Higgs field.

3.3 Hierarchy Problem

The hierarchy problem is one serious issue plaguing the SM. This problem affects the mass correction of a scalar field severely. Consider a toy model of two scalar fields with a Lagrangian of the following form ¹,

$$\mathcal{L} = (\partial_\mu \phi_1^\dagger)(\partial^\mu \phi_1) - m_1^2 \phi_1^\dagger \phi_1 + (\partial_\mu \phi_2^\dagger)(\partial^\mu \phi_2) - m_2^2 \phi_2^\dagger \phi_2 - \lambda(\phi_1^\dagger \phi_1)(\phi_2^\dagger \phi_2), \quad (3.8)$$

assuming $m_2 \gg m_1$. The quantum correction to m_1^2 can be calculated using the Feynman diagram at 1-loop level (see Fig.(3.1)) and dimensional regularization. Under the $\overline{\text{MS}}$ renormalization scheme ², the quantum correction is given by

$$\Delta m_1^2(\phi_2) = -\frac{\lambda m_2^2}{16\pi^2} \left(2 + \ln \frac{4\pi\mu^2}{m_2^2}\right). \quad (3.9)$$

¹Thanks to Dr. Okada's discussion of hierarchy problem in class. This section is based on his lecture.

²The modified MS renormalization scheme. The Euler constant γ_E and the term $1/\epsilon$ used in the dimensional regularization are removed after applying this scheme.

If ϕ_1 is also coupled to a fermion ψ via a Yukawa coupling $-Y\bar{\psi}\psi\phi$, the fermion

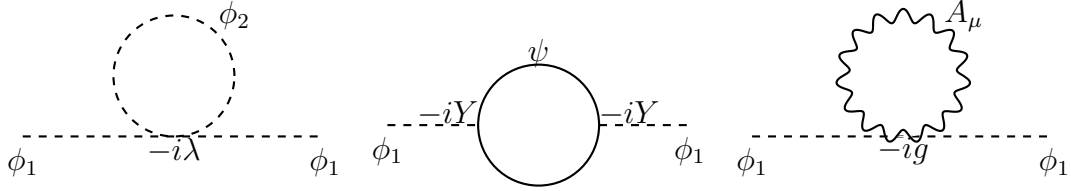


Fig. 3.1. Feynman diagrams for quantum corrections to scalar mass squared at 1-loop level. Left: Scalar loop contribution. Middle: Fermion loop contribution. Right: Gauge boson loop contribution.

loop will also contribute to the quantum correction to Δm_1^2 , which is,

$$\Delta m_1^2(\psi) = 3 \left(\frac{YM}{2\pi} \right)^2 \left(\frac{1}{2} + \ln \frac{4\pi\mu^2}{M^2} \right), \quad (3.10)$$

in which M is the mass of ψ . Finally, the coupling of ϕ_1 to a gauge bosons A_μ with mass $m_A \gg m_1$ via $g|\phi_1|^2 A_\mu A^\mu$ leads to similar quantum correction from the 3rd loop in Fig.(3.1), which is

$$\Delta m_1^2(A) = \frac{gm_A^2}{4\pi^2} \left(\frac{3}{2} + \ln \frac{4\pi\mu^2}{m_A^2} \right). \quad (3.11)$$

The three quantum corrections share the same feature, i.e., they all depend on the masses of the particles running in the loops quadratically. As long as any of the three masses (m_2, M, m_A) is much greater than m_1 , the scalar ϕ_1 will receive huge corrections to its mass. Therefore, this theory is said to be UV sensitive.

The Higgs field H is a vital ingredient of the SM, whose mass will suffer from large quantum corrections according to this analysis. If there exists some very large new physics scale, which might be of the order of the Planck scale $M_{Pl} \approx 10^{19}$ GeV, the quantum correction Δm_H^2 will be approximately $\sim M_{Pl}^2$. If the newly discovered scalar [19, 20] is the SM Higgs H , whose mass is about 125~126 GeV, there are 34 order of magnitude difference between physical m_H^2

and quantum correction Δm_H^2 , which is a fine tuning problem (or naturalness problem).

3.4 Large Extra Dimensions

The large extra dimension (LED) model [7, 8, 9] was proposed to solve the hierarchy problem by introducing a number n of large, compactified spatial dimensions (LEDs). Gravitons can propagate in the $D(=n+4)$ -dimensional space-time *bulk*. SM particles are confined to the 4-dimensional *brane*. Assuming compactification on a torus with equal radii R , the observed Planck mass M_{Pl} is related to the 4-dimensional *fundamental* Planck mass M_* by $M_{\text{Pl}}^2 = (2\pi R)^n M_*^{D-2}$. If R is sufficiently large, the fundamental Planck mass M_* may be as low as a few TeVs. This model is also called the ‘‘ADD’’ model. Table (3.2) lists the values of R for different n 's in order to lower M_* to 1 TeV.

n	1	2	3	4	5	6
R	4×10^9 km	0.34 mm	1.48 nm	3.08 pm	75.8 fm	6.4 fm

Table 3.2. Sizes of extra dimensions as n varies from 1 to 6.

To date, experimental results have not confirmed the existence of large extra dimensions (see, eg. Ref.'s [4, 21, 22, 23, 24, 5, 25]). These null results set upper bounds on the size of the large extra dimensions, or equivalently, lower bounds on the fundamental Planck scale. The ADD model with one LED requires the size of the LED to be of the order of 10^9 km (Table (3.2)) and is macroscopically ruled out because no deviations from Newtonian gravity have been observed at the solar system scale [26, 27]. Observations of neutron stars by the Fermi Large Area Telescope [21] rule out ADD models with two LEDs. Constraints on spacetimes with three large extra dimensions from astrophysical and cosmological experiments are generally very stringent, although they typically suffer from large systematic

errors. The observation of Supernova SN1987A sets a lower limit on M_D of 2.4 TeV for $n = 3$ [22], where the reduced Planck mass M_D is related to M_* by [28],

$$M_D = \left[\frac{(2\pi)^n}{8\pi} \right]^{\frac{1}{n+2}} M_*. \quad (3.12)$$

Neutron star-derived limits constrain M_D to be larger than 76 TeV for $n = 3$ [23]. Non-observation of perturbative processes predicted by LED models in collider experiments [29, 30, 31, 32, 33, 34, 35, 36, 37, 38, 39, 40] provide less stringent, albeit more accurate limits on M_D or the string scale Λ_T , which is related to M_D by [41]

$$\Lambda_T = 2\sqrt{\pi} \left[\Gamma\left(\frac{n}{2}\right) \right]^{1/(n+2)} M_D. \quad (3.13)$$

Current limits on M_D (in units of TeV) from these experiments are shown in Table (3.3), where references labeled by † indicate lower bounds on M_D derived from constraints on the string scale Λ_T and the remaining ones indicate lower bounds on M_D directly. The search for the extinction of QCD jet production by the Compact Muon Solenoid (CMS) Collaboration provides an additional lower limit of 3.3 TeV at 95% C.L. on the extinction mass scale (equivalent to the fundamental Planck scale) [24].

n	References										
	[29]	[30]	[31, 32]†	[33]†	[34]†	[35]	[36]	[37]†	[38]†	[39]	[40]
3	3.16	4.29	1.20	2.05	1.20	4.77	4.11	1.16	0.81	2.30	2.12
4	2.84	3.71	1.17	2.00	1.17	3.97	3.56	1.13	0.79	2.20	2.13
5	2.65	3.31	1.12	1.92	1.12	3.73	3.24	1.08	0.76	2.04	2.14
6	2.58	3.12	1.07	1.84	1.07	3.53	2.96	1.03	0.72	2.00	2.17

Table 3.3. The observed lower limits on M_D from collider experiments in TeV.

Lower bounds on the Planck scale can also be derived by non-observation of production and decay of TeV BHs in collider experiments and cosmic ray observations [42, 43, 44, 45, 46, 47, 48, 49]. The CMS and ATLAS (A Toroidal LHC ApparatuS) collaborations have conducted searches for BH signatures at the LHC [4, 5, 25], setting limits on the production cross section and the minimal BH mass M_{\min} , i.e., the minimum mass at which a BH can form. Depending on model assumptions and using different final states, the CMS collaboration excludes M_{\min} below 4.3 to 6.2 TeV, while the ATLAS collaboration excludes M_{\min} below 4.8 to 6.2 TeV [5] and 4.6 to 6.2 TeV [25], all at 95% C.L.. The recent 13 TeV analysis carried out by the ATLAS collaboration has excluded the production of a rotating BH with $n = 6$ [50].

4 BLACK HOLES

In this chapter, static and spherical symmetric BH solutions of vacuum Einstein equations in $D = n + 4$ ($n \geq 0$) dimensions are discussed. 4-dimensional solutions are first discussed, and the generalization to higher dimensional spacetime is briefly introduced. Then the physics of BH formation by colliding two massless particles is introduced briefly within the framework of GR. The second part is devoted to BH thermodynamics, assuming the spacetime is 4-dimensional, and the generalization to higher dimensional spacetime is straightforward. Finally, the production and decay of D -dimensional microscopic BHs at the high energy colliders are discussed.

4.1 D Dimensional Static, Spherical Symmetric Black Holes

A spacetime with a BH in it is a special solution to Einstein's equations (Eq.(2.32)). Because of the nonlinearity of Eq.(2.32), it is very difficult to analytically solve those equations. However, when a spacetime possesses symmetries, the metric $g_{\mu\nu}$ is a function of a few coordinates in a suitably chosen coordinate system, and then an analytic solution of Eq.(2.32) may exist. In fact, the spherically symmetric spacetime solution is the first 4D solution to Eq.(2.32) obtained by Karl Schwarzschild [51] in 1916, soon after the publication of Einstein's GR.

4.1.1 4D Schwarzschild Black Holes

The Schwarzschild spacetime is static, meaning, there exists a timelike Killing vector field χ^μ and a foliation of spacetime with spacelike slices Σ_t . χ^μ is normal

to Σ_t everywhere. The spacelike slices Σ_t are labeled by the parameter t which can be chosen as one coordinate of the spacetime manifold \mathcal{M} , and is called the Schwarzschild time. Since t is constant across Σ_t , its gradient $\nabla_\mu t$ is normal to Σ_t , so $\chi^\mu \propto g^{\mu\nu} \nabla_\nu t$. χ^μ can be chosen to be $g^{\mu\nu} \nabla_\nu t$ such that $\chi^\mu \nabla_\mu t = -1$, which means that the integral curve γ of χ^μ can be parametrized by t . The curve $\gamma(t)$ intersects each Σ_t only once. Suppose it intersects Σ_{t_0} at $p = \gamma(t_0)$ and as time flows, it intersects Σ_t at $q = \gamma(t)$. If there is a spatial coordinate system x^i defined on Σ_{t_0} , it is natural to also assign a coordinate system to Σ_t by letting $x^i(p) = x^i(q)$. Since any point in Σ_t is labeled by t, x^i , a coordinate system is set up for \mathcal{M} , and the metric $g_{\mu\nu}$ can be written as,

$$ds^2 = -V(x^i)dt^2 + h_{ij}dx^i dx^j, \quad (4.1)$$

where $V(x^i)$ is a function of the spatial coordinates x^i , and h_{ij} is the spatial metric on Σ_t .

In addition to being static, the Schwarzschild spacetime is also spherically symmetric, which means that any spacelike slice Σ_t has a symmetry group isomorphic to $SO(3)$. If p is a point in Σ_t , under a symmetry transformation, it will trace out a 2 dimensional surface B_r which is homeomorphic to a sphere S^2 . A sphere can be parametrized by θ and ϕ such that the metric on B_r is given by,

$$ds_B^2 = r^2(d\theta^2 + \sin^2 \theta d\phi^2), \quad (4.2)$$

where r determines the area of B_r : $A = 4\pi r^2$. For a different point $p' \notin B_r$, p' will similarly trace out a different 2 dimensional surface $B_{r'}$, which can also be parametrized by two angular coordinates. Because of the spherical symmetry, Σ_t is naturally foliated by 2 dimensional surfaces B_r , which are parametrized by two angular coordinates. In analogy to t labeling different Σ_t , r labels different B_r . r

is the radial coordinate and its divergence $\nabla_\mu r$ is also normal to B_r everywhere. The vector field $S^\mu = g^{\mu\nu}\nabla_\nu r$ is dual to $\nabla_\mu r$ and can be chosen to have integral curves perpendicular to B_r . If that is the case, the metric on Σ_t is

$$h_{ij}dx^i dx^j = W(r)dr^2 + ds_B^2, \quad (4.3)$$

with $W(r)$ a function of r . $V(x^i)$ in Eq.(4.1) should depend only on r , consequently.

Finally, plugging Eq.(4.3) in Eq.(4.1) gives the ansatz of the metric,

$$ds^2 = -V(r)dt^2 + W(r)dr^2 + r^2(d\theta^2 + \sin^2\theta d\phi^2). \quad (4.4)$$

The coordinates introduced are called the Schwarzschild coordinates. Substituting this metric into the vacuum Einstein's equations,

$$G_{\mu\nu} = R_{\mu\nu} - \frac{1}{2}g_{\mu\nu}R = 0, \quad (4.5)$$

gives the 4-dimensional Schwarzschild metric,

$$ds^2 = -\left(1 - \frac{2G_4 M_{\text{BH}}}{r}\right)dt^2 + \left(1 - \frac{2G_4 M_{\text{BH}}}{r}\right)^{-1}dr^2 + r^2(d\theta^2 + \sin^2\theta d\phi^2). \quad (4.6)$$

This metric describes the spacetime outside of a spherical object, e.g., a star or a BH, sitting at the center of the coordinate system. The parameter M is the mass of the object, and G_4 is the 4D gravitational constant.

4.1.1.1 Event Horizon

The Schwarzschild metric (Eq.(4.6)) possesses singularities at $r = 0$ and $2G_4 M_{\text{BH}}$, because at $r = 0$, g_{tt} becomes infinite, and at $r = 2G_4 M_{\text{BH}}$, g_{rr} becomes infinite, too. The singularity at $r = 0$ is the more severe one, because the

curvature invariant $R_{\mu\nu\rho\sigma}R^{\mu\nu\rho\sigma} = 48G_4^2M_{\text{BH}}^2/r^6$ blows up. This means $r = 0$ is a true spacetime singularity, called “scalar curvature singularity”, or an essential singularity. However, the singularity at $r = 2G_4M_{\text{BH}}$ is due to the choice of the particular coordinate system, which can be removed by a change of coordinate system.

For example, the tortoise coordinate r_* is defined as

$$dr_* = \left(1 - \frac{2G_4M_{\text{BH}}}{r}\right)^{-1} dr \quad \Rightarrow \quad r_* = r + 2G_4M_{\text{BH}} \ln\left(\frac{r}{2G_4M_{\text{BH}}} - 1\right). \quad (4.7)$$

A “time” coordinate is defined as $v = t + r_*$, then the metric transforms to

$$ds^2 = -\left(1 - \frac{2G_4M_{\text{BH}}}{r}\right)dv^2 + 2dvdr + r^2(d\theta^2 + \sin^2\theta d\phi^2). \quad (4.8)$$

So the components $g_{\mu\nu}$ behave normally at $r = 2G_4M_{\text{BH}}$. In this coordinate system, it is also easy to understand the meaning of the hypersurface $r = 2G_4M_{\text{BH}}$ being the event horizon. It is interesting to study the trajectory of a photon moving in the radial direction, which is parametrized by λ :

$$d\lambda^2 = -\left(1 - \frac{2G_4M_{\text{BH}}}{r}\right)dv^2 + 2dvdr = 0. \quad (4.9)$$

Solving this equation gives two results,

$$dv = 0 \quad \Rightarrow \quad v = C_1, \quad (4.10)$$

$$\frac{dv}{dr} = \frac{2r}{r - 2G_4M_{\text{BH}}} \quad \Rightarrow \quad v = 2r_* + C_2. \quad (4.11)$$

Here, C_1, C_2 are constants. The first result represents incoming light rays, while the second one is shown in Fig.(4.1), which shows that within the region $r < 2G_4M_{\text{BH}}$, all null geodesics will inevitably enter the singularity. In fact, the light cone inside the horizon always tilts towards to the singularity. Since light travels

the fastest, any particle entering the horizon will never escape from it. A slightly

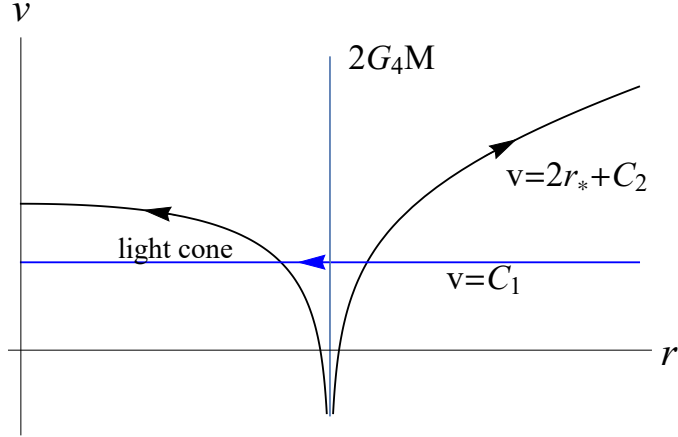


Fig. 4.1. Null geodesics in the Eddington-Finkelstein coordinates (v, r) .

different choice of “time” coordinate $u = t - r_*$ gives,

$$ds^2 = -\left(1 - \frac{2G_4M_{\text{BH}}}{r}\right)du^2 - 2dudr + r^2(d\theta^2 + \sin^2\theta d\phi^2), \quad (4.12)$$

whose radial null geodesics are described by

$$u = D_1, \quad (4.13)$$

$$u = -2r_* + D_2, \quad (4.14)$$

with D_1, D_2 constant. Fig.(4.2) shows the two null geodesics, of which $u = D_1$ represents an outgoing photon, and the light cones inside the horizon. This plot shows that any particle inside the horizon will eventually come out from it. In fact, this coordinate system suitably describes a white hole. In contrast, the previous coordinate system describes a BH.

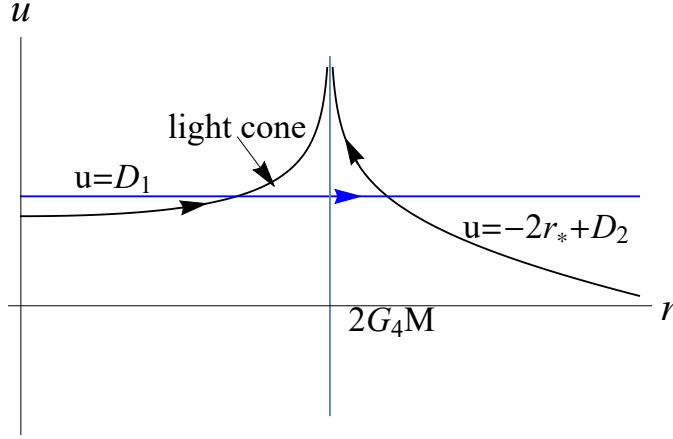


Fig. 4.2. Null geodesics in the Eddington-Finkelstein coordinates (u, r) .

4.1.1.2 Particle motion

Let $u^\mu = dx^\mu/d\tau$ be the 4 velocity of a particle moving in the background of Schwarzschild spacetime. The existence of a timelike Killing vector χ^μ defines the conserved energy per unit mass,

$$E = -u^\mu \chi_\mu = \left(1 - \frac{2G_4 M_{\text{BH}}}{r}\right) \frac{dt}{d\tau}. \quad (4.15)$$

This spacetime also possesses another Killing vector field, i.e. $\phi^\mu = (\partial_\phi)^\mu$, which generates a rotational symmetry around the z -axis. It defines the conserved angular momentum per unit mass,

$$L = u^\mu \phi_\mu = r^2 \frac{d\phi}{d\tau}, \quad (4.16)$$

where the motion has been restricted to the hypersurface $\theta = \pi/2$, which is adequate because of the spherical symmetry. The motion of the particle is determined by,

$$-\left(1 - \frac{2G_4 M_{\text{BH}}}{r}\right) \left(\frac{dt}{d\tau}\right)^2 + \left(1 - \frac{2G_4 M_{\text{BH}}}{r}\right)^{-1} \left(\frac{dr}{d\tau}\right)^2 + r^2 \left(\frac{d\phi}{d\tau}\right)^2 = -\iota. \quad (4.17)$$

ι is a constant, which is either 1 or 0, depending on whether the particle is massive or not. Substituting Eq.'s (4.15, 4.16) into the above, the effective one-dimensional motion is described by

$$\frac{1}{2}\left(\frac{dr}{d\tau}\right)^2 + \frac{1}{2}\left(1 - \frac{2G_4 M_{\text{BH}}}{r}\right)\left(\frac{L^2}{r^2} + \iota\right) = \frac{E^2}{2}, \quad (4.18)$$

which means that the particle is propagating in an effective potential (the second term in Eq.(4.18)) and its total mechanical energy is $E^2/2$.

4.1.1.3 Surface Gravity

The event horizon is a null hypersurface, and the tangent to the horizon turns out to be the Killing vector χ^μ . For this reason, this hypersurface is also called the Killing horizon. By Froebnius's theorem,

$$\chi_{[\mu}\nabla_\nu\chi_{\rho]} = 0, \quad (4.19)$$

where square brackets mean totally antisymmetrizing indices. Since χ^μ is a Killing vector, $\nabla_\mu\chi_\nu = -\nabla_\nu\chi_\mu$, and the above equation reduces to

$$\chi_\mu\nabla_\nu\chi_\rho + \chi_\rho\nabla_\mu\chi_\nu + \chi_\nu\nabla_\rho\chi_\mu = 0. \quad (4.20)$$

On a Killing horizon, $\chi_\mu\chi^\mu = 0$, so $\nabla_\mu(\chi_\nu\chi^\nu)$ is normal to the horizon, and there exists a function κ defined on the horizon such that

$$-2\kappa\chi_\mu = \nabla_\mu(\chi_\nu\chi^\nu) = 2\chi^\nu\nabla_\mu\chi_\nu = -2\chi^\nu\nabla_\nu\chi_\mu, \quad (4.21)$$

which means that χ^μ is tangent to a null geodesic which is not affinely parametrized,

$$\chi^\nu\nabla_\nu\chi^\mu = \kappa\chi^\mu. \quad (4.22)$$

To calculate κ , Eq.(4.20) is contracted with $\nabla^\mu \chi^\nu$,

$$2\kappa^2 \chi_\rho + \chi_\rho \nabla^\mu \chi^\nu \nabla_\mu \chi_\nu = 0 \quad \Rightarrow \quad \kappa = \sqrt{-(\nabla^\mu \chi^\nu)(\nabla_\mu \chi_\nu)/2}. \quad (4.23)$$

For the Schwarzschild BH, $\chi^\mu = \delta_t^\mu$ in the Schwarzschild coordinate system, and its covariant derivative is $\nabla_\nu \chi^\mu = \Gamma^\mu_{\nu\rho} \delta_t^\rho = \Gamma^\mu_{\nu t}$. Therefore, κ is

$$\kappa = \sqrt{-\frac{\Gamma^\mu_{\nu t} \Gamma^\nu_{\mu t}}{2}} = \frac{1}{4G_4 M_{\text{BH}}}. \quad (4.24)$$

The meaning of κ can be understood by the following calculation:

$$3\chi^{[\mu} \nabla^\nu \chi^{\rho]} \chi_{[\mu} \nabla_\nu \chi_{\rho]} = \chi^\mu \chi_\mu (\nabla^\nu \chi^\rho)(\nabla_\nu \chi_\rho) - 2(\chi^\mu \nabla_\mu \chi^\nu)(\chi^\rho \nabla_\rho \chi_\nu). \quad (4.25)$$

At the horizon, the left hand side vanishes by Eq. (4.19). Since $\nabla_\nu(\chi_\mu \chi^\mu)$ does not vanish on the horizon, l'Hopital's rule can be applied to get

$$\kappa^2 = \lim \frac{(\chi^\mu \nabla_\mu \chi^\nu)(\chi^\rho \nabla_\rho \chi_\nu)}{-\chi_\sigma \chi^\sigma}, \quad (4.26)$$

where \lim means approaching the horizon. Let $V^2 = -\chi_\sigma \chi^\sigma$, so V is the redshift factor. $a^\nu = (\chi^\mu \nabla_\mu \chi^\nu)/V^2$ is the 4-acceleration of χ^ν . Defining $a^2 = a^\nu a_\nu$, κ can be expressed as

$$\kappa = \lim(Va). \quad (4.27)$$

This equation implies that κ is the acceleration measured at infinity, so it is called the *surface gravity*.

4.1.2 Higher Dimensional Case

In this section, spacetime is assumed to be $D = n + 4$ dimensions with $n \neq 0$, and all dimensions are non-compact. The spacetime can also be foliated by

spacelike slices Σ_t labeled by time t , each of which has $\text{SO}(D - 2)$ symmetry. Besides the radial coordinate r , there are $D - 2$ angular coordinates: $\theta_1, \theta_2, \dots, \theta_{D-2}$, and the metric of the unit $D - 2$ dimensional sphere is [52]

$$d\Omega_{D-2}^2 = d\theta_{D-2}^2 + \sin^2 \theta_{D-2} d\Omega_{D-3}^2, \dots, d\Omega_1 = d\theta_1, \quad (4.28)$$

so that $0 < \theta_1 < 2\pi$, $0 < \theta_2, \dots, \theta_{D-2} < \pi$. Finally, the metric for the D dimensional static, spherically symmetric spacetime is,

$$ds^2 = -f(r)dt^2 + g(r)dr^2 + r^2 d\Omega_{D-2}^2, \quad (4.29)$$

where $f(r)$ and $g(r)$ are determined by Eq.(4.5), that is,

$$f(r) = 1/g(r) = 1 - \frac{16\pi G_D M_{\text{BH}}}{(D-2)S_{D-2}r^{D-3}}, \quad S_{D-2} = \frac{2\pi^{\frac{D-1}{2}}}{\Gamma(\frac{D-1}{2})}. \quad (4.30)$$

Here, M_{BH} is the BH mass, and G_D is the D dimensional gravitational constant, which is related to the fundamental Planck scale M_* via,

$$M_* = 1/G_D^{1/(n+2)}. \quad (4.31)$$

As can be verified, the metric component g_{rr} blows up at the horizon, which is defined by $r = R_S$, where

$$R_S = \frac{1}{\sqrt{\pi}M_*} \left[\frac{8\Gamma(\frac{n+3}{2})}{n+2} \right]^{\frac{1}{n+1}} \left(\frac{M_{\text{BH}}}{M_*} \right)^{\frac{1}{n+1}}, \quad (4.32)$$

This is the D dimensional Schwarzschild radius. $\chi^\mu = \delta_t^\mu$ also becomes tangent to the horizon at R_S , and the surface gravity is given by

$$\kappa = \frac{|f'(R_S)|}{2} = \frac{D-3}{2R_S}. \quad (4.33)$$

If $M_{\text{BH}} = 5M_*$, the sizes of R_{S} as a function of n is given in Table (4.1). Comparison with Table (3.2) shows that the Schwarzschild radius is much smaller

n	1	2	3	4	5	6	7
$R_{\text{S}} \left(\frac{1 \text{ TeV}}{M_*} \times 10^{-4} \text{ fm} \right)$	3.61	2.34	1.98	1.84	1.78	1.76	1.77

Table 4.1. D -dimensional Schwarzschild radius R_{S} vs n for $n > 0$.

than the size of extra dimensions, which justifies the use of the metric in Eq.(4.29).

4.2 Four Laws of Black Hole Mechanics

This section will be devoted to a general, brief discussion of the four laws of BH mechanics based on Ref's [17, 53, 54]. They are

- 0th Law: The surface gravity κ is constant over the event horizons of stationary BHs, assuming the dominate energy condition.
- 1st Law: $dM_{\text{BH}} = \frac{\kappa}{8\pi G} dA_H + \Omega_H dJ_H$, where A_H is the horizon area, J_H is the angular momentum of the BH and Ω_H is its angular velocity.
- 2nd Law: $\delta A_H \geq 0$ in any process, if the cosmic censorship and weak energy condition hold.
- 3rd Law: It is impossible to achieve $\kappa = 0$ in a physical process.

These four laws of BH mechanics resemble the four laws of thermodynamics in such a way that

$$\begin{aligned}
\kappa/2\pi &\leftrightarrow T \\
M_{\text{BH}} &\leftrightarrow E \\
A_H/4\pi G_D &\leftrightarrow S \\
\Omega_H &\leftrightarrow p \\
J_H &\leftrightarrow V.
\end{aligned}
\tag{4.34}$$

Here, T is the temperature, E is the energy, S is the entropy, p is the pressure and V is the volume. Therefore, they are also called the four laws of BH thermodynamics. In the following, they will be derived purely from the mechanical side. The discussion follows a more logical order, instead of the order listed above.

4.2.1 Raychaudhuri's Equation & the 2nd Law

The resemblance between BH mechanics and thermodynamics was first noticed by the discovery of the *BH area theorem* [55]. This theorem roughly states that the BH area never decreases. The rigorous proof of the theorem is highly technical and involves the use of causality. To understand this theorem roughly, it is necessary to introduce null geodesic congruence. In this section, the null geodesic congruence will be discussed briefly. For more details on it, please refer to Appendix B.

A null geodesic congruence is a set of null geodesics in a region of spacetime such that every point in this region lies on precisely one curve. Let K_0 be a 2-dimensional, compact and spacelike surface whose induced metric is $\gamma_{\mu\nu}$ and the coordinate system is $\{\theta, \phi\}$. Light rays emanating from K_0 will form a null geodesic congruence. Take a sphere S^2 in the 4-dimensional Minkowski spacetime for example. All light rays emanating from this sphere S^2 form the null geodesic

congruence, and $K_0 = S^2$. Call k^μ the tangent vector to a null geodesic in the congruence, then $g^{\mu\nu}\nabla_\nu k_\mu$ is an important quantity, which is called the expansion ρ . It satisfies Raychaudhuri's equation,

$$\frac{d\rho}{dv} = -\frac{\rho^2}{2} - \hat{\sigma}_{\mu\nu}\hat{\sigma}^{\mu\nu} + \hat{\omega}_{\mu\nu}\hat{\omega}^{\mu\nu} - R_{\mu\nu}k^\mu k^\nu, \quad (4.35)$$

where $\hat{\sigma}_{\mu\nu}$ and $\hat{\omega}_{\mu\nu}$ are the shear and rotation (refer to Appendix B). Suppose all null geodesics are normal to K_0 . It can be shown that $\hat{\omega}_{\mu\nu} = 0$, and $\hat{\sigma}_{\mu\nu}\hat{\sigma}^{\mu\nu} \geq 0$.

Another important conclusion associates the change in the area A of K_0 with ρ . Suppose all light rays in the congruence are parametrized by "time" v , and on K_0 , $v = 0$. After a while, at "time" v , all photons in the congruence will form a different compact surface K_v . It can be shown that the area A of K_v varies, depending on ρ in the following way,

$$\frac{dA}{dv} = \oint_{K_v} \frac{\partial\sqrt{\gamma}}{\partial v} d\theta d\phi = \oint_{K_v} \rho\sqrt{\gamma} d\theta d\phi, \quad (4.36)$$

where γ is the determinant of $\gamma_{\mu\nu}$. Therefore, if $\rho > 0$, K_v will expand, but if $\rho < 0$, K_v will shrink, instead.

Hawking [55] argued in 1971 that the area of the BH horizon never decreases in any physical process in GR. This is the famous *Hawking's area theorem*: Assuming the cosmic censorship conjecture and $R_{\mu\nu}k^\mu k^\nu \geq 0$, the area of the future event horizon is nondecreasing. This is because suppose K is one section of the future event horizon H , then the expansion ρ of null k^μ emanating from and normal to K is non-negative, as long as certain causality conditions are satisfied. Therefore, Eq.(4.36) implies that the area A_H of H never decreases. This is the second law of BH mechanics.

4.2.2 The 0th Law

The Zeroth law is a statement of how the surface gravity κ varies across the Killing horizon. In this section, χ^μ will represent a general Killing vector field. To calculate it, the operator $\chi_{[\mu}\nabla_{\nu]}$ is applied to Eq.(4.22) to get

$$\chi_\rho\chi_{[\mu}\nabla_{\nu]}\kappa + \kappa\chi_{[\mu}\nabla_{\nu]}\chi_\rho = \chi_{[\mu}\nabla_{\nu]}\chi^\sigma\nabla_\sigma\chi_\rho - \chi_{[\mu}R_{\nu]\alpha\sigma\rho}\chi^\alpha\chi^\sigma. \quad (4.37)$$

Using Eq.(4.20) and the Killing property $\nabla_\mu\chi_\nu = -\nabla_\nu\chi_\mu$, the second term on the left hand side of the above equation is

$$\kappa\chi_{[\mu}\nabla_{\nu]}\chi_\rho = -\frac{1}{2}\kappa\chi_\rho\nabla_\mu\chi_\nu, \quad (4.38)$$

and the first term in the last line is accordingly,

$$\chi_{[\mu}\nabla_{\nu]}\chi^\sigma\nabla_\sigma\chi_\rho = -\frac{1}{2}\kappa\chi_\rho\nabla_\mu\chi_\nu, \quad (4.39)$$

which implies that,

$$\chi_\rho\chi_{[\mu}\nabla_{\nu]}\kappa = -\chi_{[\mu}R_{\nu]\alpha\sigma\rho}\chi^\alpha\chi^\sigma. \quad (4.40)$$

Now, apply $\chi_{[\mu}\nabla_{\nu]}$ to $\chi_\alpha\nabla_\beta\chi_\rho$,

$$\chi_{[\mu}\nabla_{\nu]}(\chi_\alpha\nabla_\beta\chi_\rho) = -\frac{1}{2}(\nabla_\mu\chi_\nu)\chi_\alpha\nabla_\beta\chi_\rho - \chi_\alpha\chi_{[\mu}R_{\nu]\gamma\beta\rho}\chi^\gamma. \quad (4.41)$$

Antisymmetrizing over indices α, β and ρ leads to,

$$\chi_{[\mu}\nabla_{\nu]}(\chi_{[\alpha}\nabla_\beta\chi_{\rho]}) = -\frac{1}{2}(\nabla_\mu\chi_\nu)\chi_{[\alpha}\nabla_\beta\chi_{\rho]} - \chi_{[\mu}R_{\nu]\gamma[\beta\rho}\chi_{\alpha]}\chi^\gamma. \quad (4.42)$$

The left hand side and the first term on the right hand side vanish due to Eq.(4.19). Contracting with $g^{\rho\nu}$ and expand the last term,

$$\chi_{[\beta}R_{\alpha]\rho\gamma\mu}\chi^\rho\chi^\gamma = \chi_\mu\chi_{[\beta}R_{\alpha]\gamma}\chi^\gamma. \quad (4.43)$$

Combining this equation with Eq.(4.40) gives,

$$\chi_{[\mu}\nabla_{\nu]}\kappa = -\chi_{[\mu}R_{\nu]\rho}\chi^\rho. \quad (4.44)$$

Suppose $\chi^\mu = dx^\mu/d\lambda$, and $k^\mu = dx^\mu/dv$ is another vector field. If $\lambda = -e^{-\kappa v}/\kappa$, then k^μ satisfies the geodesic equation,

$$k^\nu\nabla_\nu k^\mu = 0, \quad (4.45)$$

so it is interesting to calculate the corresponding $\hat{B}_{\mu\nu}$ (Eq.(B.15)). On the horizon,

$$k_{[\rho}\nabla_{\mu]}k_\nu = -e^{-2\kappa v}\chi_\nu\left(\kappa\chi_{[\rho}\nabla_{\mu]}v + \frac{1}{2}\nabla_\rho\chi_\mu\right). \quad (4.46)$$

Then for any two spatial deviation vectors η^ρ and ξ^ν , the following relation holds,

$$\eta^\rho\xi^\nu k_{[\rho}\nabla_{\mu]}k_\nu = \frac{1}{2}(\eta^\rho k_\rho\xi^\nu\nabla_\mu k_\nu - k_\mu\eta^\rho\xi^\nu\nabla_\rho k_\nu) = 0, \quad (4.47)$$

since $\eta^\rho k_\rho = \xi^\rho k_\rho = 0$. Therefore, $\eta^\rho\xi^\nu\nabla_\rho k_\nu = 0$, which leads to,

$$\hat{B}_{\mu\nu} = 0, \quad (4.48)$$

by Eq.(B.15). Thus, ρ , $\hat{\sigma}_{\mu\nu}$ and $\hat{\omega}_{\mu\nu}$ all vanish, and Raychaudhuri's equation (4.35) implies that,

$$R_{\mu\nu}k^\mu k^\nu = 0 = R_{\mu\nu}\chi^\mu\chi^\nu. \quad (4.49)$$

Assuming the dominate energy condition, which states that $-T^\mu{}_\nu\chi^\nu$ is a future-directed timelike or null vector field, Einstein's equation (2.32) can be used to get $T^\mu{}_\nu\chi_\mu\chi^\nu = 0$, which means that $-T^\mu{}_\nu\chi^\nu$ is parallel to χ^μ , in other words,

$$-R^\mu{}_\nu\chi^\nu = -\frac{1}{2}\left(T^\mu{}_\nu\chi^\nu - \frac{\chi^\mu}{D-2}T\right). \quad (4.50)$$

Plugging it into Eq.(4.44) gives,

$$\chi_{[\mu}\nabla_{\nu]}\kappa = 0, \quad (4.51)$$

which is equivalent to saying that κ is a constant over the Killing horizon. This is the zeroth law of BH mechanics.

4.2.3 The 1st Law

The first law of BH mechanics will apply to stationary, axisymmetric BHs. A stationary spacetime possesses a timelike Killing vector field χ^μ , which can be normalized, $\chi^\mu\chi_\mu = -1$ at infinity. If \mathcal{M} is also axisymmetric, it also has an axial Killing vector field ϕ^μ . In general, χ^μ is not normal to the horizon of a BH, but $l^\mu = \chi^\mu + \Omega_H\phi^\mu$ is. Ω_H is a constant and is called the angular velocity of the horizon. The first law involves the variations in a BH's energy M and angular momentum J_H , as discussed below.

Consider a timelike hypersurface Σ with unit normal vector n^μ , and Σ is bounded by two compact surfaces: one is the horizon $\mathcal{H} = H \cap \Sigma$, and the other, K_∞ , is at infinity. So the integral

$$-\int_\Sigma R_{\nu\mu}\chi^\mu n^\nu \sqrt{h}d^3x = \int_\Sigma (\nabla^\mu\nabla_\mu\chi_\nu)n^\nu \sqrt{h}d^3x, \quad (4.52)$$

gives rises to

$$M_{\text{BH}} = \frac{\kappa A}{4\pi G_4} + 2\Omega_H J_H. \quad (4.53)$$

This is the first law in integral form.

To obtain the differential form of Eq.(4.53), the variation of both sides is taken,

$$\delta M_{\text{BH}} = \frac{\delta\kappa A + \kappa\delta A}{4\pi G_4} + 2\delta\Omega_H J_H + 2\Omega_H\delta J_H. \quad (4.54)$$

Suppose the variation is caused by some event which affects a BH, e.g., some particles fall through horizon. Then after a sufficiently long time, the system settles down to a new BH solution with metric $g'_{\mu\nu} = g_{\mu\nu} + \gamma_{\mu\nu}$. For simplicity, a suitable diffeomorphism leaves the position of H , and the two Killing vectors χ^μ, ϕ^μ unchanged. Calculating the variation $\delta\kappa$ and integrating the variation over the horizon result in,

$$A_H\delta\kappa = -4\pi G_4\delta M_{\text{BH}} - 8\pi G_4\delta\Omega_H J_H. \quad (4.55)$$

This equation together with Eq.(4.54) gives the differential form of the first law of BH mechanics,

$$\delta M_{\text{BH}} = \frac{\kappa\delta A_H}{8\pi G_4} + \Omega_H\delta J_H. \quad (4.56)$$

The resemblance between Eq.(4.56) and the 1st law of thermodynamics is clear once one makes the identification Eq.(4.34).

4.2.4 The 3rd Law

The third law of BH mechanics states that it is impossible to reduce κ to zero in any physical process. As an example, the Schwarzschild BH's surface gravity κ is given by Eq.(4.24) (or Eq.(4.33)) and contains powers of M in the denominator. In order to make $\kappa = 0$, M would have to be infinity, which is impossible.

4.3 Black Holes in Particle Collisions

4.3.1 Black Hole Production

According to the *Hoop Conjecture* [56], a BH forms when a mass M is confined to a region of typical size equal to the Schwarzschild radius for that mass, $R_S(M)$. Therefore, if two particles collide with center of mass energy \sqrt{s} and impact parameter smaller than $R_S(\sqrt{s})$, a BH may form. If $R_S \ll R$, as expected in the ADD scenario, the newly formed BH lives in a D -dimensional spacetime with negligible curvature at the BH scale. In this case, the Schwarzschild radius of the BH is given by Eq.(4.32) where $M_{\text{BH}} = (1 - y)\sqrt{s}$ and y is the fraction of energy which escapes into the bulk as gravitons, depending on the impact parameter. The Hoop Conjecture implies a BH production cross section $\sigma(s, n, y) = \pi F R_S^2$, where the form factor $F \leq 1$ is related to y and accounts for the energy of the colliding particles which is not trapped in the event horizon, the so called “graviton energy loss at formation.”

The Hoop Conjecture can be tested by the *trapped surface* approach, based on classical GR [57, 58, 59, 60, 61]. A trapped surface (TS) is a $(D - 2)$ -dimensional compact, spacelike submanifold with the property that the expansion ρ of both families (i.e., “incoming” and “outgoing”) of future directed null geodesics orthogonal to it is everywhere negative. If a spacetime satisfies certain causality conditions, and $R_{\mu\nu}k^\mu k^\nu \geq 0$ for all null k^μ , any trapped surface is enclosed by a horizon. In fact, any sphere with radius smaller than R_S is a trapped surface for the D -dimensional Schwarzschild BH. By finding the position of the so-called marginally trapped surface to which the outgoing null geodesic congruences are orthogonal and from which emanating have vanishing expansion, the horizon radius can be estimated to be the radius of the marginally trapped surface. Since the horizon radius increases with the BH mass, the trapped surface approach gives a lower bound on BH mass, and is checked against alternative approaches. For

example, Ref.[62] studied gravitational energy emission in the linearized limit, and suggested that the trapped surface method overestimates the graviton energy loss. The instantaneous method predicts that the graviton energy loss is only about 10% of the center of mass energy \sqrt{s} for head-on collisions. Perturbative calculations which model the parton-parton collision as a plunge of a relativistic test particle into a BH with mass \sqrt{s} agree on that result [63]. Therefore, the mass of a BH produced in a high energy collider is expected to range between 60% to 100% of \sqrt{s} [64].

Since BH production in hadron colliders occurs at the parton level, the total cross section for a hadronic collision is obtained by integrating over the Parton Distribution Functions (PDFs) of the hadrons [27]

$$\sigma(s, n, y, M_{\min}) = \sum_{ij} \int_0^1 2zdz \int_{x_m}^1 dx \int_x^1 \frac{dx'}{x'} f_i(x', Q) f_j(x/x', Q) \sigma(\sqrt{xs}, n, y), \quad (4.57)$$

where the $f_i(x, Q)$ are the PDFs with four-momentum transfer Q , and z is the impact parameter normalized to its maximum value. The cutoff at small x is $x_m = M_{\min}^2 / \{s[(1 - y(z))^2]\}$, where M_{\min} is the minimum-allowed mass of the BH. The total cross section in the absence of graviton energy loss at formation is recovered by setting $F = 1$ (Black Disk (BD) cross section) [64].

4.3.2 Black Hole Decay

If the initial BH mass is much larger than the Planck mass, a semiclassical treatment suggests that the newly-formed BH decays through four distinct phases: *balding*, *spin-down*, *Hawking* and *Planck* [65].

Balding phase BH radiates multipole moments and quantum numbers [66, 67], eventually settling down to a D -dimensional Kerr geometry.

Spin-down phase Angular momentum evaporates via Hawking radiation, so a D -dimensional Schwarzschild BH forms at the end of this phase.

Hawking phase BH decays into elementary particles via Hawking radiation. As discussed in Section (4.3.1), the trapped surface method likely overestimates the graviton energy loss in the BH production, so it is assumed that most of the energy of the BH is radiated in the Hawking phase, with SM particles dominating the decay products. For the details of D -dimensional Hawking radiation, please refer to Chapter 5.

Planck phase When the mass of the evaporating BH approaches the Planck scale, $Q_{\min} \sim M_*$, the BH enters the quantum phase, where the decay ceases to be semiclassical and becomes dominated by quantum gravitational effects.

5 HAWKING RADIATION

5.1 Unruh Effect

An easier way to understand the Hawking effect and to derive the spectrum of the radiation of BHs is through the study of the *Unruh effect* [18, 68], in which an accelerated observer in Minkowski spacetime views the vacuum seen by a free-fall observer as thermal. Although this effect takes place in a flat spacetime, it reflects the fact that different observers do not necessarily share the same vacuum state.

For simplicity, a uniformly accelerated observer is considered in a 2 dimensional Minkowski spacetime. Because of translational and rotational symmetry, this simplification is adequate to grasp the essential ideas of the Unruh effect. Let the metric be

$$ds^2 = -dt^2 + dx^2, \quad (5.1)$$

and let the observer's worldline be parametrized by τ , so that the observer's position is given by

$$t = \frac{\sinh \alpha\tau}{\alpha}, \quad x = \frac{\cosh \alpha\tau}{\alpha}. \quad (5.2)$$

The acceleration is

$$a^\mu = u^\nu \partial_\nu u^\mu = (\alpha \sinh \alpha\tau, \alpha \cosh \alpha\tau), \quad (5.3)$$

Its magnitude is

$$a = \sqrt{a^\mu a_\mu} = \alpha, \quad (5.4)$$

and α is assumed to be constant. The trajectory (Eq.(5.2)) is one branch of a hyperbola, and if α varies, the observer will trace out a different hyperbola. In

this way, a new coordinate system (ξ, η) can be introduced, defined by,

$$t = \frac{e^{\kappa\xi} \sinh \kappa\eta}{\kappa}, \quad x = \frac{e^{\kappa\xi} \cosh \kappa\eta}{\kappa}, \quad (5.5)$$

where $-\infty < \xi, \eta < +\infty$. This coordinate system covers one quarter of the 2 dimensional Minkowski spacetime, region I in Fig.(5.1). The trajectory of the observer is one of these η lines, whose $\kappa = \alpha$. Similarly, region III can also be charted. The coordinates there are also called (ξ, η) but their directions are opposite, i.e., in region II,

$$t = -\frac{e^{\kappa\xi} \sinh \kappa\eta}{\kappa}, \quad x = -\frac{e^{\kappa\xi} \cosh \kappa\eta}{\kappa}. \quad (5.6)$$

In this way, the metric tensor in these two regions can be expressed as,

$$ds^2 = e^{2\alpha\xi}(-d\eta^2 + d\xi^2). \quad (5.7)$$

Suppose there is a scalar field $\phi(x)$ satisfying the Klein-Gordon equation, $\square\phi = 0$. There are two classes of observers: the free-fall observers, whose velocities are $(\partial_t)^\mu$, and the uniformly accelerated ones, whose velocities are $(\partial_\eta)^\mu$. They will observe different particle content of the field $\phi(x)$. The free-fall observer will view the solutions to the Klein-Gordon equation as linear combinations of the plane wave,

$$\phi_k = \frac{\exp[-i(\omega t - kx)]}{\sqrt{4\pi\omega}}, \quad (5.8)$$

and its complex conjugate ϕ_k^* , with $|k| = \omega$. Therefore, ϕ can be expanded as

$$\phi = \int dk(a_k\phi_k + a_k^\dagger\phi_k^*), \quad (5.9)$$

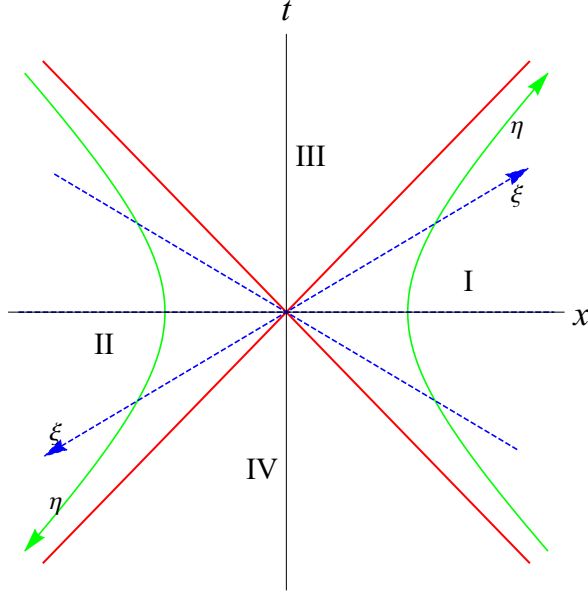


Fig. 5.1. The Rindler coordinate system (ξ, η) covers region I of the Minkowski spacetime. Region II is another copy of region I, whose coordinates are still called (ξ, η) but pointing in the opposite directions.

where a_k and a_k^\dagger are the ladder operators for free-fall observers. So $a_k|\Omega_M\rangle = 0$, and $|\Omega_M\rangle$ is the vacuum seen by a free-fall observer. The number operator is $a_k^\dagger a_k$.

But the accelerated observer in region I will use different plane waves, which are

$$\psi_k^I = \frac{\exp[-i(\omega\eta - k\xi)]}{\sqrt{4\pi\omega}}, \quad (5.10)$$

and their complex conjugates ψ_k^{I*} , while the accelerated observer in region II uses,

$$\psi_k^{II} = \frac{\exp[i(\omega\eta + k\xi)]}{\sqrt{4\pi\omega}}, \quad (5.11)$$

and ψ_k^{II*} . So the wave function decomposition is,

$$\phi = \int dk (b_k^I \psi_k^I + b_k^{I\dagger} \psi_k^{I*} + b_k^{II} \psi_k^{II} + b_k^{II\dagger} \psi_k^{II*}). \quad (5.12)$$

Here, $b_k^I, b_k^{I\dagger}$ and $b_k^{II}, b_k^{II\dagger}$ are the ladder operators associated with the accelerated observers in region I and II, respectively. In addition, these observers observe a vacuum state $|\Omega_R\rangle$, and $b_k^I|\Omega_R\rangle = b_k^{II}|\Omega_R\rangle = 0$. The number operators are $n_R^I(k) = b_k^{I\dagger}b_k^I$ and $n_R^{II}(k) = b_k^{II\dagger}b_k^{II}$ for regions I and II, respectively.

The relations between ϕ_k and ψ_k^I, ψ_k^{II} must be determined in order to study the relations between the vacuum states $|\Omega_M\rangle$ and $|\Omega_R\rangle$. A trick reveals that there exist another set of basic wave modes,

$$\varphi_k^I = \frac{e^{\pi\omega/2\kappa} a^{i\omega/\kappa}}{\sqrt{8\pi\kappa \sinh(\pi\omega/\kappa)}} (-t+x)^{i\omega/\kappa}, \quad (5.13)$$

$$\varphi_k^{II} = \frac{e^{\pi\omega/2\kappa} a^{i\omega/\kappa}}{\sqrt{8\pi\kappa \sinh(\pi\omega/\kappa)}} (-t-x)^{i\omega/\kappa}, \quad (5.14)$$

such that

$$\phi = \int dk (c_k^I \varphi_k^I + c_k^{I\dagger} \varphi_k^{I*} + c_k^{II} \varphi_k^{II} + c_k^{II\dagger} \varphi_k^{II*}). \quad (5.15)$$

Here c_k^I and $c_k^{I\dagger}$ are the ladder operators for φ_k^I , and similarly, c_k^{II} and $c_k^{II\dagger}$ for φ_k^{II} .

The Bogoliubov transformations relate ladder operators of different observers, and are given by

$$b_k^I = \frac{e^{\pi\omega/2\kappa} c_k^I + e^{-\pi\omega/2\kappa} c_{-k}^{II\dagger}}{\sqrt{2 \sinh(\pi\omega/\kappa)}}, \quad (5.16)$$

$$b_k^{II} = \frac{e^{\pi\omega/2\kappa} c_k^{II} + e^{-\pi\omega/2\kappa} c_{-k}^{I\dagger}}{\sqrt{2 \sinh(\pi\omega/\kappa)}}. \quad (5.17)$$

It turns out that $c_k^I|\Omega_M\rangle = c_k^{II}|\Omega_M\rangle = 0$. Therefore, c_k^I and c_k^{II} annihilate the same vacuum state as a_k does. Since the number operator for the accelerated observer

in region I is $n_R^I(k) = b_k^{I\dagger} b_k^I$, so the expected number of particles of frequency ω is

$$\begin{aligned}
\langle \Omega_M | n_R^I(k) | \Omega_M \rangle &= \langle \Omega_M | b_k^{I\dagger} b_k^I | \Omega_M \rangle \\
&= e^{-\pi\omega/\kappa} \frac{\langle \Omega_M | c_k^I c_k^{I\dagger} | \Omega_M \rangle}{2 \sinh(\pi\omega/\kappa)} \\
&= \frac{1}{\exp \frac{\omega}{\kappa/2\pi} - 1}.
\end{aligned} \tag{5.18}$$

Therefore, the accelerated observer views the vacuum of the free-fall observer as thermal. The temperature is given by

$$T_U = \frac{\kappa}{2\pi}. \tag{5.19}$$

5.2 Hawking Radiation

In 1975, Hawking [69] studied the solutions to the massless Klein-Gordon equation in the background of Schwarzschild spacetime and showed that the outgoing positive frequency mode at future infinity is a mixture of positive and negative frequency incoming modes at past infinity. This mixture leads to the famous Hawking radiation, which has the Planck distribution,

$$\langle n_\omega^s \rangle = \frac{1}{\exp\left(\frac{\omega}{T_H}\right) + (-1)^{2s}}. \tag{5.20}$$

where s is the spin of the emitted particle. The Hawking temperature takes the same form as the Unruh temperature,

$$T_H = \frac{\kappa}{2\pi}. \tag{5.21}$$

By Eq.(4.33), the Hawking temperature for a D -dimensional, spherically symmetric, static BH is

$$T_H = \frac{n+1}{4\pi R_S}, \quad (5.22)$$

where $n = D - 4$. Table (5.1) shows T_H for D -dimensional BH whose mass $M_{\text{BH}} = 5M_*$.

n	1	2	3	4	5	6	7
$T_H \left(\frac{M_*}{1 \text{ TeV}} \text{ GeV} \right)$	77	179	282	379	470	553	629

Table 5.1. The Hawking temperature of a D -dimensional BH as a function of n . T_H is in units of M_* . Data are taken from Ref.[3].

The number of particles emitted per unit time, i.e., the flux spectrum, can thus be calculated using the following expression [3],

$$\frac{dN^{(s)}(\omega)}{dt} = \sum_j \frac{\sigma_{j,n}^{(s)}(\omega)}{\exp(\omega/T_H) + (-1)^{2s}} \frac{d^{n+3}k}{(2\pi)^{n+3}}, \quad (5.23)$$

and the power spectrum is

$$\frac{dE^{(s)}(\omega)}{dt} = \sum_j \frac{\omega \sigma_{j,n}^{(s)}(\omega)}{\exp(\omega/T_H) + (-1)^{2s}} \frac{d^{n+3}k}{(2\pi)^{n+3}}. \quad (5.24)$$

The extra term $\sigma_{j,n}^{(s)}(\omega)$ in the above two equations is called the graybody factor, which arises due to the effects of the effective potential (refer to Eq.(4.18)). Any particle emitted from the BH and reaching infinity has to penetrate the effective potential, so the spectra are modified. $\sigma_{j,n}^{(s)}(\omega)$ corresponds to the transmission cross section for a particle propagating in the effective potential, so it is related to the absorption coefficient $\mathcal{A}_j^{(s)}$ in the following way,

$$\sigma_{j,n}^{(s)}(\omega) = \frac{2^n A_H}{\pi(\omega R_S)^{n+2}} \Gamma\left(\frac{n+3}{2}\right)^2 N_j |\mathcal{A}_j^{(s)}|^2, \quad (5.25)$$

with N_j representing the multiplicity of states for the same partial wave j ,

$$N_j = \frac{(2j + n + 1)(j + n)!}{j!(n + 1)!}. \quad (5.26)$$

A_H is the horizon area of a D -dimensional Schwarzschild BH,

$$A_H = 2\pi R_S^{n+2} \pi^{(n+1)/2} \Gamma\left(\frac{n+3}{2}\right)^{-1}. \quad (5.27)$$

The graybody factor can be determined by studying the propagation of different fields - scalar, vector, spinor and tensor fields - in the background of a D -dimensional Schwarzschild spacetime, i.e., their Schrödinger equations. Since in the ADD model, SM particles propagate on the brane, but gravitons propagate in the bulk, Schrödinger equations are different for the brane modes and the bulk modes. In the following two sections, these two cases are discussed briefly.

5.2.1 Hawking Radiation on the Brane

SM particles live on the brane, so they feel only the induced metric on the brane, that is, setting θ_s ($s = D - 2, D - 3, \dots, 3$) to zero and defining $\theta_2 = \theta$, $\theta_1 = \varphi$ for simplicity in Eq.(4.29),

$$ds^2 = -f(r)dt^2 + f(r)^{-1}dr^2 + r^2(d\theta^2 + \sin^2\theta d\varphi^2), \quad (5.28)$$

with $f(r) = 1 - (R_S/r)^{n+1}$. The tortoise coordinate y is also useful,

$$y = \frac{f(r)}{R_S^{n+1}(n+1)}. \quad (5.29)$$

Following the treatment of Ref.[69], a generic matter field $\Psi_s(t, r, \theta, \phi)$ can be decomposed into modes with definite energy ω , angular momentum quantum number

j and magnetic quantum number m , i.e.,

$$\Psi_s(t, r, \theta, \phi) = e^{-i\omega t} e^{im\varphi} R_s(r) S_{s,j}^m(\theta), \quad (5.30)$$

where $S_{s,j}^m(\theta)$ are the spin-weighted spheroidal harmonics. Plugging this expression into the equation of motion for $\Psi_s(t, r, \theta, \phi)$ in the background metric given by Eq.(5.28), the so-called *master equation* can be obtained for the radial part $R_s(r) = [r^2 f(r)]^{-s} P_s(r) = \Delta^{-s} P_s(r)$,

$$\Delta^s \frac{d}{dr} \left(\Delta^{1-s} \frac{dP_s}{dr} \right) + \left[\frac{\omega^2 r^2}{f(r)} + i2\omega sr - i \frac{s\omega r^2 f'(r)}{f(r)} - j(j+1) + s(s+1) \right] P_s(r) = 0. \quad (5.31)$$

This equation can be analytically solved using an approximation method in which solutions at the near horizon region ($r \rightarrow R_S$) and at the far-field region ($r \gg R_S$) can be obtained. These two solutions can then be matched in the intermediate region. In the near horizon region, the general solution takes the following form,

$$P_s^{NH}(r) = A_- f^\alpha (1-f)^\beta F_s(a, b, c; f) + A_+ f^{-\alpha} (1-f)^\beta F_s(a-c+1, b-c+1, 2-c; f), \quad (5.32)$$

where A_\pm are constants, $F_s(a, b, c; f)$ is a hypergeometric function with hypergeometric indices (a, b, c) defined as,

$$a = \alpha + \beta + \frac{s+n(1-s)}{n+1}, \quad b = \alpha + \beta, \quad c = 1 - s + 2\alpha. \quad (5.33)$$

α and β are given by

$$\alpha_+ = s + i \frac{\omega R_S}{n+1}, \quad \alpha_- = -i \frac{\omega R_S}{n+1}, \quad (5.34)$$

$$\beta_\pm = \frac{1}{2(n+1)} \left[1 - 2s \pm \sqrt{(1+2j)^2 - 4\omega^2 R_S^2 - i8s\omega R_S} \right]. \quad (5.35)$$

A boundary condition must be imposed at the horizon in order to select the “+” version or the “-” version. Near the horizon, only incoming modes are allowed, because nothing can escape from the BH. Therefore, this leads to keeping the “-” version. In the far-field region, the solution is approximately,

$$P_s^{FF}(r) = e^{-i\omega r} r^{j+s} [B_+ M(j-s+1, 2j+2, i2\omega r) + B_- U(j-s+1, 2j+2, i2\omega r)], \quad (5.36)$$

where B_{\pm} are also constants, and M and U are the Kummer functions. Then expanding $P_s^{NH}(r)$ in the limit $r \rightarrow +\infty$, and $P_s^{FF}(r)$ in the limit $\omega r \ll 1$, the expansions which relate B_{\pm} to A_- are matched in the following way,

$$B_+ = \frac{A_-}{R_S^{j+s}} \frac{\Gamma(1-s+2\alpha_-)\Gamma(-2\beta_- + \frac{1-2s}{n+1})}{\Gamma(\alpha_- - \beta_- + 1 - s)\Gamma(\alpha_- - \beta_- + \frac{1-2s}{n+1})}, \quad (5.37)$$

$$B_- = \frac{A_- R_S^{j-s+1} (i2\omega)^{2j+1} \Gamma(1-s+2\alpha_-)\Gamma(2\beta_- - \frac{1-2s}{n+1})\Gamma(j-s+1)}{\Gamma(\alpha_- + \beta_-)\Gamma(\alpha_- + \beta_- + \frac{s+n(1-s)}{n+1})\Gamma(2j+1)}. \quad (5.38)$$

Finally, the calculation of the graybody factor requires rewriting the far-field solution (Eq.(5.36)) in the limit $r \rightarrow +\infty$,

$$P_s^{(\infty)}(r) = A_{\text{in}}^{(\infty)} \frac{e^{-i\omega r}}{(2\omega r)^{1-2s}} + A_{\text{out}}^{(\infty)} \frac{e^{i\omega r}}{2\omega r}, \quad (5.39)$$

with

$$A_{\text{in}}^{(\infty)} = \frac{e^{-i\pi(j-s+1)/2}}{(2\omega)^{j+s}} \left[B_- + \frac{B_+ e^{i\pi(j-s+1)} \Gamma(2j+2)}{\Gamma(j+s+1)} \right], \quad (5.40)$$

$$A_{\text{out}}^{(\infty)} = \frac{B_+ e^{i\pi(j+s+1)} \Gamma(2j+2)}{\Gamma(j-s+1)(2\omega)^{j+s}}. \quad (5.41)$$

So the absorption coefficient $\mathcal{A}_j^{(s)}$ for a scalar field ($s = 0$) is

$$|\mathcal{A}_j^{(0)}|^2 = 1 - \left| \frac{A_{\text{out}}^{(\infty)}}{A_{\text{in}}^{(\infty)}} \right|^2, \quad (5.42)$$

while for higher spin fields (vector and spinor fields), $\mathcal{A}_j^{(s)}$ can be calculated using the following relation,

$$|\mathcal{A}_j^{(s)}|^2 = (2\omega R_S)^{2(1-2s)} \left| \frac{A_-}{A_{\text{in}}^{(\infty)}} \right|^2. \quad (5.43)$$

Therefore,

$$|\mathcal{A}_j^{(s)}|^2 = \frac{(2\omega R_S)^{2j+2-2s}}{|\Gamma(1-s+2\alpha_-)[C(\omega R_S)^{2j+1} + D]|^2}, \quad (5.44)$$

where C and D are constants,

$$C = \frac{2^{2j+1} e^{i\pi(s-1/2)} \Gamma(2\beta_- - \frac{1-2s}{n+1}) \Gamma(j-s+1)}{\Gamma(\alpha_- + \beta_-) \Gamma(\alpha_- + \beta_- + \frac{s+n(1-s)}{n+1}) \Gamma(2j+1)}, \quad (5.45)$$

$$D = \frac{\Gamma(2j+2) \Gamma(-2\beta_- + \frac{1-2s}{n+1})}{\Gamma(\alpha_- - \beta_- + 1 - s) \Gamma(\alpha_- - \beta_- + \frac{1-2s}{n+1}) \Gamma(j+s+1)}. \quad (5.46)$$

Substituting Eq.(5.44) into Eq.(5.25) gives,

$$\sigma_{j,n}^{(s)}(\omega) = \frac{(2\omega R_S)^{2j-2s} (2j+1) A_H}{|\Gamma(1-s+2\alpha_-)[C(\omega R_S)^{2j+1} + D]|^2}. \quad (5.47)$$

With this analytic expression, it is easy to plot $\sigma_{j,n}^{(s)}(\omega)$ as a function of energy ω for $s = 0, 1/2, 1$; these plots are shown in Fig.(5.2). This figure shows that the graybody factor for a scalar field decreases with ω , and is smaller for large extra dimension models $n > 0$ than for $n = 0$. For a fermion field, the graybody factor decreases and then increases in the higher energy regime for $n > 0$, but for $n = 0$, the graybody factor is initially smaller, but a monotonic increasing function, so eventually it surpasses the one for $n > 0$. The graybody factor of a gauge boson

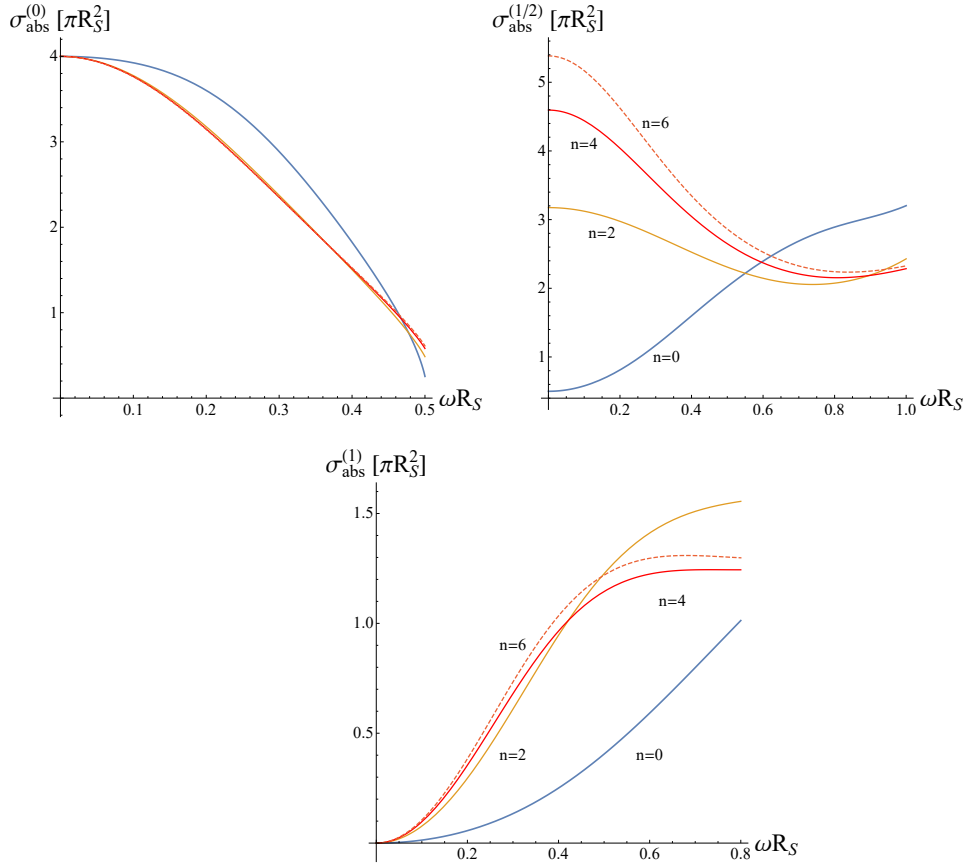


Fig. 5.2. Graybody factor $\sigma_{abs}^{(s)}(\omega)$ vs energy ω at different n . $\sigma_{abs}^{(s)}(\omega)$ is actually summed over j upto the third partial waves. Color code: $n = 0$ - Blue; $n = 2$ - Brown; $n = 4$ - Red Solid; $n = 6$ - Red Dashed.

behaves very differently. It increases at low energies, and then slowly decreases at higher energies for $n = 4, 6$. For $n = 2$, the graybody factor is an increasing function of ω in the energy range considered. Finally, the graybody factor for a gauge boson in the usual 4 dimensional spacetime ($n = 0$) is an increasing function within the considered energy range.

Power spectra can also be plotted according to Eq.(5.24), as shown in Fig.(5.3). The plot shows that for all types of fields, the power emission rates are increasing functions of ω for $n > 0$, while for $n = 0$, the power emission rates increase at lower energies but decreases at the higher energy regime. Fig.(5.3) also shows

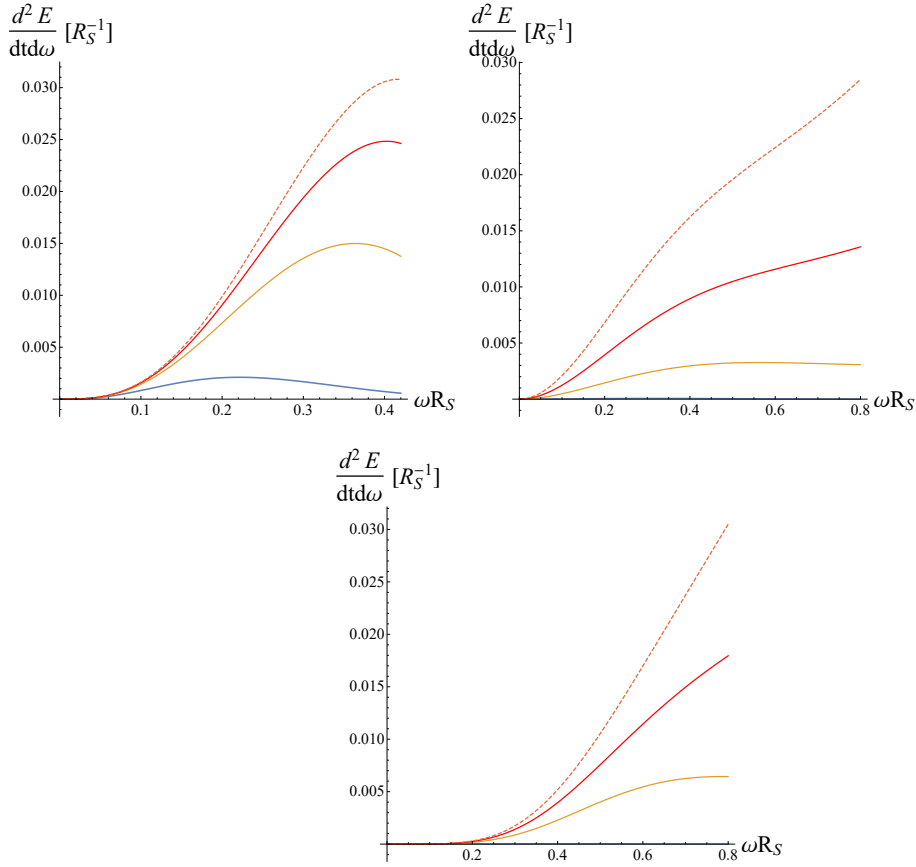


Fig. 5.3. The power spectra for spin-0 (top left), 1/2 (top right), 1 (bottom) fields. The color code is the same as Fig.(5.2)

that as n increases, the BH evaporates faster. So a higher dimensional BH will have shorter lifetime in the ADD model.

The conclusions discussed above are based on analytic solutions of Eq.(5.31), which are valid only at low energies. To find higher energy behaviors, numerical methods have been applied to calculate graybody factor in Ref.[70]. The numerically calculated graybody factors are shown in Fig.(5.4). As seen from these graphs, the low energy behavior of graybody factors agree with the analytic results (Fig.(5.3)) very well. Graybody factors oscillate in the energy range shown for all n 's with slightly decreasing amplitudes. At higher energies, $n = 0$ dominates over $n > 0$ for all types of fields, but the graybody factor for a scalar field

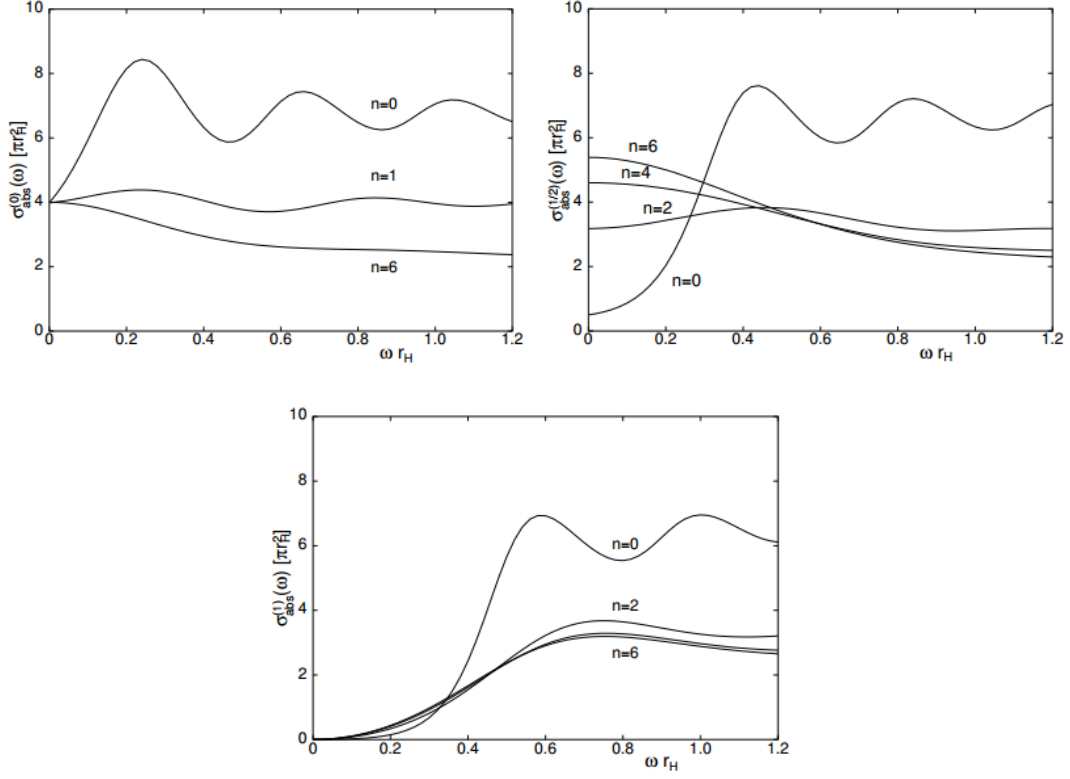


Fig. 5.4. Numerical results for graybody factors for scalars (top left), fermions (top right) and gauge bosons (bottom). These are taken from Ref.[3].

at $n = 0$ is also greater than $n > 0$. The emission rates were also determined in Ref.[70], which are shown in Fig.(5.5). The agreement with the analytic results in the low energy regime can be identified again, and the emission rates are enhanced greatly as n increases. Integration over the whole energy region gives the total emissivities as listed in Table (5.2). It is also possible to predict what type of par-

n	0	1	2	3	4	5	6	7
Scalars	1.0	8.94	36.0	99.8	222	429	749	1220
Fermions	1.0	14.2	59.5	162	352	664	1140	1830
Gauge Bosons	1.0	27.1	144	441	1020	2000	3530	5740

Table 5.2. Total energy emissivities for different matter fields as functions of n . They are normalized to the ones for $n = 0$ individually for each type of fields. Data are taken from Ref.[3].

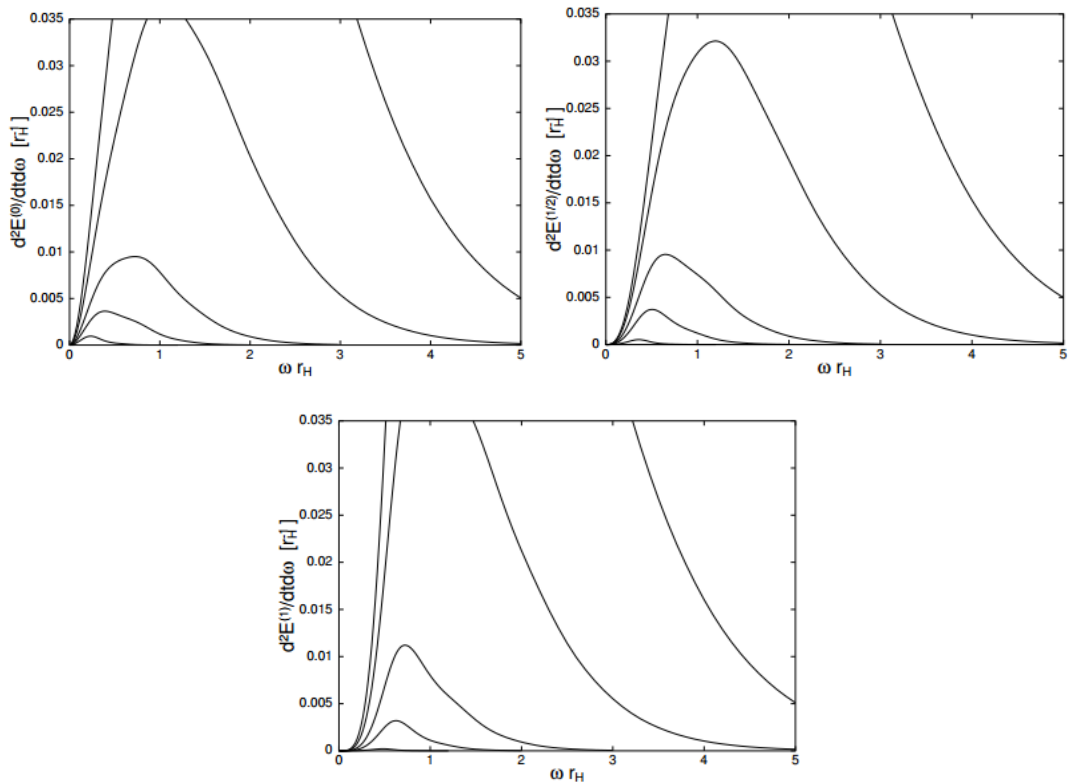


Fig. 5.5. Numerical results for power emission rates for scalars (top left), fermions (top right) and gauge bosons (bottom). These are taken from Ref.[3].

icles the BH prefers to emit. In Ref.[70], estimations for the relative emissivities were also made, which are tabulated in Table (5.3). Therefore, for $n = 0$, scalars

n	0	1	2	3	4	5	6	7
Scalars	1.00	1.00	1.00	1.00	1.00	1.00	1.00	1.00
Fermions	0.55	0.87	0.91	0.89	0.87	0.85	0.84	0.82
Gauge Bosons	0.23	0.69	0.91	1.00	1.04	1.06	1.06	1.07

Table 5.3. Relative energy emissivities for different n 's, normalized to the emissivity of the scalar field. Data are taken from Ref.[3]

carry away most of the BH energy, then fermions and then, gauge bosons. This situation changes when n increases. More and more energy is emitted in the form

of fermions and gauge bosons. When $n \geq 4$, gauge bosons contribute the most energy lost. Fermions always carry away less energy than scalars.

5.2.2 Hawking Radiation in the Bulk

Although the bulk modes cannot be detected, they contribute to the large missing energy, which is a distinct feature of BH events. So it is still important to study bulk modes to determine the amount of energy emitted into the bulk, and thus the energy left for emission on the brane. For this purpose, the complete metric Eq.(4.29) should be used. Since only gravitons, and possibly scalars, are allowed to propagate in the bulk, attention will be focussed on these fields. Since scalars are simpler, the first step will be to study the graybody factor for a scalar field.

5.2.2.1 Scalars

A generic scalar field is a linear composition of the expression below [70, 3],

$$\phi(t, r, \theta_i) = e^{i\omega R_{\omega l}(r)} \tilde{Y}_l(\Omega). \quad (5.48)$$

Here, the $\tilde{Y}_l(\Omega)$ are the higher dimensional generalization of the usual spherical harmonic functions, and Ω collectively represents all angular coordinates θ_i . Substituting this function into Klein-Gordon equation gives rise to the radial equation,

$$\frac{f(r)}{r^{n+2}} \frac{d}{dr} \left[f(r) r^{n+2} \frac{dR}{dr} \right] + \left[\omega^2 - \frac{f(r)}{r^2} l(l+n+1) \right] R = 0. \quad (5.49)$$

This equation can be analytically solved using a for similar to that used to obtain the brane modes, which are approximate and are only valid in low energy regime, so the analytic solutions of Eq.(5.49) will not be discussed (refer to [70, 3]). Numerical calculation gives the spectra graybody factors and energy emission rates

as functions of n , which are shown in Fig.(5.6). The left graph in Fig.(5.6) also

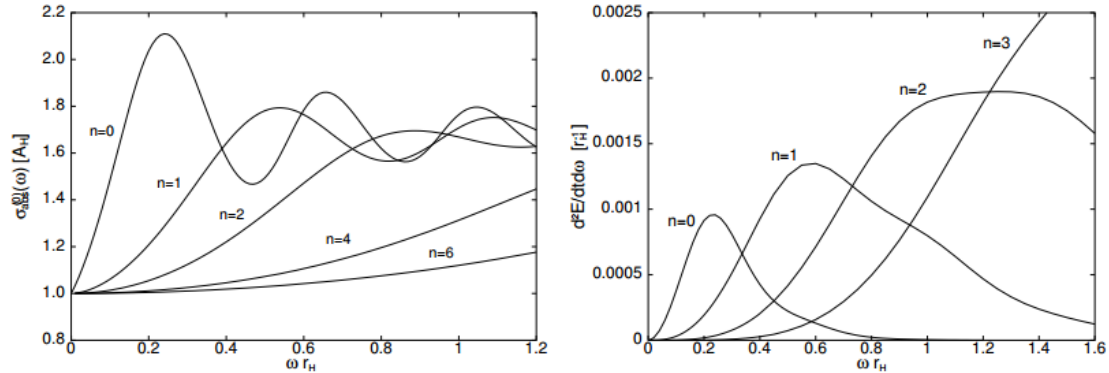


Fig. 5.6. Graybody factors (left) and energy emission rates (right) for bulk scalar mode as functions of energy ω for different n 's. Figures are taken from Ref.[3]

shows the oscillations of graybody factors as ω increases, although the relatively small energy range does not allow the oscillations for $n = 4, 6$ to be manifest. The right graph again shows the enhancement of emission as n increases. Integrating the energy emission rates over the whole energy regime gives the emissivities for the bulk and brane modes. Table (5.4) displays the ratio of bulk to brane emissivities for the scalar field. It shows that brane modes dominate over bulk modes

n	0	1	2	3	4	5	6	7
Bulk/Brane	1.0	0.40	0.24	0.22	0.24	0.33	0.52	0.93

Table 5.4. Bulk-to-brane energy emissivities of scalars for different values of n . Data are taken from Ref.[3].

for $2 \leq n \leq 4$, so most of scalar energy will be emitted into brane.

5.2.2.2 Gravitons

Gravitons are excitations of metric perturbations. For D -dimensional Schwarzschild BHs, a metric perturbation can be decomposed into three parts: a symmetric traceless tensor T , a vector V and a scalar S . Each type of metric perturbation

can be decomposed into modes like Eq.(5.48), and the radial parts $R_\Lambda(r)$ of the three types of perturbation satisfy the same equation,

$$f(r) \frac{d}{dr} \left[f(r) \frac{dR_\Lambda}{dr} \right] + (\omega^2 - \mathcal{V}_\Lambda) R_\Lambda = 0. \quad (5.50)$$

Here, the index Λ collectively stands for $\{B, \omega, l, n\}$ where $B = S, V$, or T , and $\mathcal{V}_\Lambda(r)$ is the effective potential. For tensor-like and vector-like perturbations, it is,

$$\mathcal{V}_{T/V, \omega, l, n} = \frac{f(r)}{r^2} \left[l(l+n+1) + \frac{n(n+2)}{4} - \frac{k}{4}(n+2)^2 \left(\frac{R_S}{r} \right)^{n+1} \right], \quad (5.51)$$

where $k = -1$ for tensor-like perturbations and $k = 3$ for vector-like perturbations. For the scalar-like perturbations, the potential is

$$\mathcal{V}_{S, \omega, l, n} = \frac{f(r)}{r^2} \frac{qx^3 + px^2 + wx + z}{4[2u + (n+2)(n+3)x]^2}, \quad (5.52)$$

where

$$\begin{aligned} x &= \left(\frac{R_S}{r} \right)^{n+1}, \quad u = l(l+n+1) - n - 2, \\ q &= (n+2)^4(n+3)^2, \quad z = 16u^3 + 4u^2(n+2)(n+4), \\ p &= (n+2)(n+3)[4u(2n^2 + 5n + 6) + n(n+2)(n+3)(n-2)], \\ w &= -12u(n+2)[u(n-2) + n(n+2)(n+3)]. \end{aligned} \quad (5.53)$$

Eq.(5.50) has been solved analytically in the low energy regime [71] and in the intermediate energy regime [72], which will not be discussed, since numerical calculations were also done in Ref.'s[73, 74, 75]. The numerical calculations found that the graviton radiation spectra are strongly enhanced in the higher energy regime. In Ref.s[73, 74], total energy emissivity for gravitons as a function of n is given, which is displayed in Table (5.5). Comparing Table (5.5) with Table (5.2) shows that the emissivity of gravitons is greatly enhanced at high n 's. Although

n	0	1	2	3	4	5	6	7
Gravitons	1	103	1036	3374	2×10^4	5.2×10^4	2.5×10^5	8×10^5

Table 5.5. Total energy emissivity for gravitons as a function of n . This table should be compared with Table (5.2). Data are taken from [74].

the graviton’s emissivity is much larger than that of brane modes, the huge number of brane mode degrees of freedom (d.o.f.) still makes the brane channel dominate over the bulk channel, as shown in Table (5.6). This table also shows that the

n	0	1	2	3	4	5	6	7
Scalars	6.8	4.0	3.7	3.6	3.6	3.6	3.3	2.9
Fermions	83.8	78.7	75.0	72.9	69.9	68.1	61.6	53.4
Gauge Bosons	9.3	16.7	20.0	21.8	22.3	22.6	20.7	18.6
Gravitons	0.1	0.6	1.3	1.7	4.2	5.7	14.4	25.1

Table 5.6. Percentage of power going into each field species for the SM with one Higgs field above the spontaneous symmetry breaking scale. Data are taken from Ref.[74].

contribution of gravitons cannot be neglected for large n , because, for example, when $n = 7$ nearly one quarter of the BH energy is emitted in the form of gravitons, which becomes the missing energy in high energy colliders.

6 BLACK HOLE EVENT SIMULATION

6.1 CATFISH: A Black Hole Event Generator

In this work, CATFISH (Collider grAviTational Field Simulator for black Holes) is used, which is a Fortran 77 Monte Carlo generator designed specifically for simulating BH events at CERN's LHC [64]. The simulated BH is a higher dimensional Schwarzschild BH, and it decays into SM particles and gravitons mainly via Hawking radiation. Possible phenomenological treatments of Planck phase are also implemented. The generator interfaces to the PYTHIA Monte Carlo fragmentation code [76] using the Les Houches interface [77]. In our analysis, we run CATFISH (v2.10) with the CTEQ6PDF PDF set and PYTHIA (v6.425) Tune Z1.

The simulation of a BH event in CATFISH follows these steps. First, CATFISH computes the total and differential cross sections for the BH formation. The initial BH mass is sampled from the differential cross section. The BH is then decayed through the Hawking mechanism until the BH mass reaches the quantum limit, where a final non-thermal hard event is generated or a BH remnant is created. The unstable quanta emitted by the BH are instantaneously hadronized or decayed by PYTHIA, which also simulates initial- and final-state radiation particles. To determine the physics of BH formation and decay, CATFISH uses several external parameters and switches:

- *ADD parameters*

1. Fundamental Planck mass: $MSTAR = M_*$.

2. Number of extra dimensions: $\text{NEXTRADIM} = n = 3, 4, 5, 6$.

- *Black hole formation parameters*

1. Graviton energy loss at formation: $\text{GRAVITONLOSS} = 0$ (BD model), 1 (YR or YN TS models, see below).

2. Gravitational loss model: $\text{GRAVITONMODEL} = 0$ (YN TS model [60]), 1 (YR improved TS model [61]).

3. Minimum initial BH mass in Planck units: $\text{XMIN} = M_{\text{min}}/M_* \geq 1$.

- *Black hole evaporation parameters*

1. Minimum quantum BH mass in Planck units: $\text{QMIN} = Q_{\text{min}}/M_* \leq \text{XMIN}$.

2. Number of quanta emitted in the Planck phase: $\text{NP} = n_p$. If $\text{NP} = 0$, the BH forms a stable remnant with mass Q_{min} .

6.1.1 Black Hole Production in CATFISH

CATFISH incorporates three models for BH formation and cross section: BD, Yoshino-Nambu TS model [60] and Yoshino-Rychkov (YR) improved TS model [61]. The total cross section is given by Eq.(4.57). The PDF used for this work is CTEQ6. As discussed in Section 4.3.1, BD cross section is used by setting $F = 1$, so that the graviton energy loss is ignored. In CATFISH, this model is chosen by setting $\text{GRAVITONLOSS} = 0$.

If BD model is switched on, $y = 0$ and $F = 1$, so the expression for the total cross section becomes simpler and it is given by,

$$\sigma(s, n, \text{XMIN}) = \sum_{ij} \int_0^1 2zdz \int_{x_m}^1 dx \int_x^1 \frac{dx'}{x'} f_i(x', Q) f_j(x/x', Q) \sigma(\sqrt{xs}, n, 0). \quad (6.1)$$

Here, x_m is simply $XMIN^2 M_*^2/s$, since $y = 0$, and the total cross section is expressed in terms of $XMIN$. The differential cross section $d\sigma/dM_{BH}$ and the total cross section σ v.s. M_{BH} can be obtained by running CATFISH at $n = 4$, and $XMIN = QMIN = 1$, where M_{BH} is the BH mass. Graviton energy loss is also switched off. The results are shown in Fig.(6.1).

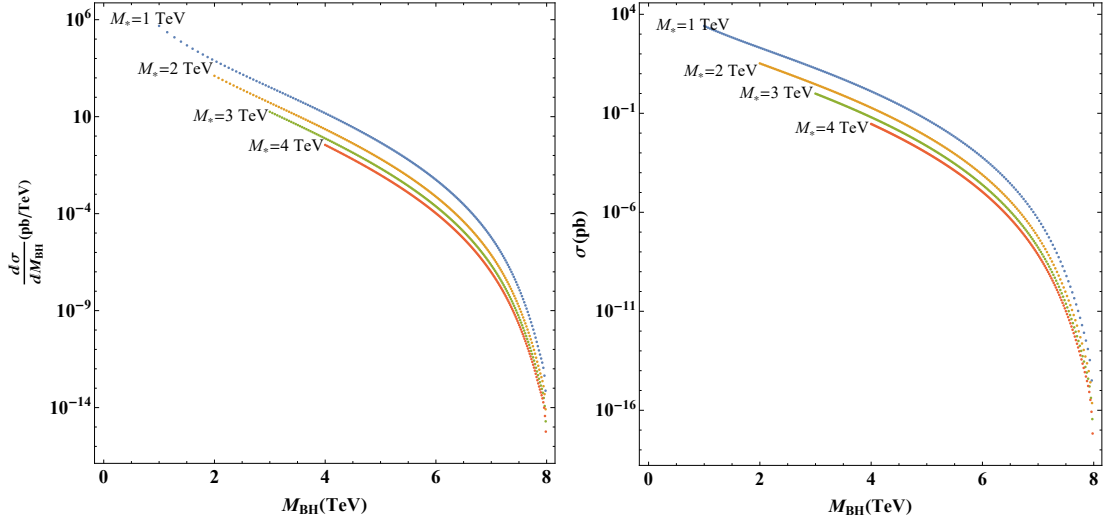


Fig. 6.1. Left: The differential cross section $d\sigma/dM_{BH}$ v.s. M_{BH} . Right: The total cross section σ v.s. M_{BH} . M_* varies from 1 TeV to 4 TeV.

6.1.2 Black Hole Decay in CATFISH

According to Section 4.3.2, a BH decays through four phases. There is a lack of results for the balding and spin-down phases, so energy loss in these two stages are assumed to be either negligible or included in the energy loss during production. This is a reasonable assumption because TS model might overestimate the energy loss. So CATFISH simulates neither of phases in the current version, although their effects could significantly affect the event signatures [64].

6.1.2.1 Hawking phase

In CATFISH, black decay process starts with Hawking phase. So a BH is modeled as a D -dimensional Schwarzschild one and Hawking radiation carries away its energy. It is assumed that BH quickly settles down to a lighter Schwarzschild one after emitting a particle. The total decay multiplicity is [78]

$$N = S_0 \frac{n+1}{4\pi} \frac{\sum_i c_i \mathcal{R}_i \Gamma_{\mathcal{R}_i}}{\sum_j c_j \mathcal{P}_j \Gamma_{\mathcal{P}_j}}, \quad (6.2)$$

where S_0 is the initial entropy of the BH, obtained by integrating the 1st law Eq.(4.56) with $\Omega_H = 0$,

$$S_0 = \frac{n+1}{n+2} \frac{M_{\text{BH}}}{T_H}. \quad (6.3)$$

c_i is the degrees of freedom (DoFs) of species i as listed in Table (6.1). \mathcal{R}_i and \mathcal{P}_j

Species	c_i	%	$N_i/N(\%)$			
			$n=3$	$n=4$	$n=5$	$n=6$
Quarks q	72	60.5	70.0	69.2	68.5	68.1
Charged leptons l	12	10.1	11.7	11.5	11.4	11.3
Neutrinos ν	6	5.04	5.8	5.8	5.7	5.7
Photon γ	2	1.68	0.65	0.72	0.7	0.80
EW bosons W/Z	9	7.56	2.91	3.23	3.47	3.61
Gluons g	16	13.45	5.18	5.75	6.18	6.41
Higgs h	1	0.84	3.64	3.69	3.75	3.78
Graviton G	1	0.84	0.05	0.11	0.15	0.30

Table 6.1. DoFs c_i and percentages (%) for the SM particles on the brane and graviton in the bulk. Also shown are the fractions N_i/N of multiplicities for different n obtained from Eq.(6.5) (last 4 columns). Data are taken from Ref.[64].

are the emissivity normalizations, which are

$$\mathcal{R}_s = \begin{cases} 1.4 \times 10^{-3}, & s = 0, \\ 4.8 \times 10^{-4}, & s = 1/2, \\ 1.5 \times 10^{-4}, & s = 1, \\ 2.2 \times 10^{-5}, & s = 2; \end{cases}, \quad \mathcal{P}_s = \begin{cases} 2.9 \times 10^{-4}, & s = 0, \\ 1.6 \times 10^{-4}, & s = 1/2, \\ 6.7 \times 10^{-5}, & s = 1, \\ 1.5 \times 10^{-5}, & s = 2. \end{cases} \quad (6.4)$$

Finally, $\Gamma_{\mathcal{R}_i}$ and $\Gamma_{\mathcal{P}_j}$ are the relative emissivities. They are displayed in Tables (6.2) and (6.3), respectively.

n	3	4	5	6
Higgs	1	1	1	1
Fermions	0.78	0.76	0.74	0.73
Gauge bosons	0.83	0.91	0.96	0.99
Gravitons	0.91	1.9	2.5	5.1

Table 6.2. Fraction of emission rates per DoF and species j , $\Gamma_{\mathcal{R}_i}$, normalized to the Higgs field. The graviton values include all the helicity states. Data are taken from Ref.'s[73, 74].

n	3	4	5	6
Higgs	1	1	1	1
Fermions	0.89	0.87	0.85	0.84
Gauge bosons	1.0	1.04	1.06	1.06
Gravitons	2.7	4.8	8.8	17.7

Table 6.3. Fraction of radiated power per DoF and species i , $\Gamma_{\mathcal{P}_j}$, normalized to the Higgs field. The graviton values include all the helicity states. Data are taken from Ref.'s[73, 74].

The decay multiplicities per species N_i are,

$$N_i = N \frac{c_i \mathcal{R}_i \Gamma_{\mathcal{R}_i}}{\sum_j c_j \mathcal{R}_j \Gamma_{\mathcal{R}_j}}, \quad (6.5)$$

which are shown in Table (6.1).

The Hawking radiation ends when the BH mass decreases to Q_{\min} , which might be close to M_* . 4-momentum is conserved at each step in the evaporation process by taking into account the recoil of the BH on the brane due to the emission of particles.

6.1.2.2 Planck phase

The lack of well-established quantum theory of gravity forces CATFISH to implement two phenomenological models: final explosion into NP ($\neq 0$) particles each with equal energy, and the formation of a stable remnant (NP = 0). A remnant is a charge neutral particle and is invisible to the detector, thus it contributes to the missing energy. The electric charge can be chosen to be conserved, and the QCD color is always conserved.

6.1.3 Some Simulation Results

In this section, several sample models will be presented. These events will be analyzed at the parton level, so quarks and gluons will not hadronize. CATFISH was run by fixing $n = 4$, GRAVITONLOSS = 0, XMIN = QMIN = 1, $\alpha = 0$, but varying $M_* = 1, 2, 3, 4$ TeV and NP = 0, 2, 4, 6. The multiplicity fractions for each type of particle species are determined; these fractions are shown in Table (6.4). It shows that quarks and gluons dominate the final products, taking up 90% \sim 99%. There are more charged leptons than gravitons for NP = 0, but graviton is the next dominating species for NP $\neq 0$ and increases with NP. The remaining species take up small fractions of final products. In Table (6.5), the fractions of energy carried away from the BH by different particles are displayed. As shown in this table, fermions carry away the most amount of energy, ranging from $\sim 70\%$ to $\sim 89\%$ of BH energy. As NP increases, more and more energy is emitted into the gauge boson channel, from $\sim 11\%$ to $\sim 24\%$, and fermion channel's contribution to energy loss decreases. Gravitons start to make noticeable contribution at NP

M_* (TeV)	NP	Percentage (%)							
		q	Charged l	ν	γ	W/Z	g	h	G
1	0	41.49	0.41	0.18	0.09	0.01	57.68	0	0
	2	43.79	0.69	0.49	0.19	0.44	52.98	0.05	1.13
	4	43.81	1.31	0.86	0.31	0.92	49.86	0.12	2.39
	6	43.83	1.79	1.13	0.40	1.31	47.49	0.17	3.31
2	0	42.49	0.24	0.10	0.11	0	56.98	0	0
	2	45.09	0.63	0.43	0.20	0.43	51.99	0.06	0.97
	4	44.76	1.26	0.87	0.33	0.98	48.72	0.13	2.54
	6	44.96	1.81	1.15	0.44	1.39	45.94	0.18	3.55
3	0	44.04	0.13	0.05	0.12	0	56.62	0	0
	2	47.21	0.58	0.40	0.20	0	50.35	0	1
	4	46.61	1.28	0.88	0.36	1.03	46.81	0.14	2.47
	6	46.29	1.86	1.17	0.45	1.48	44.24	0.19	3.72
4	0	46.26	0.04	0.02	0.13	0	52.54	0	0
	2	49.43	0.56	0.38	0.22	0.46	48.27	0.06	0.45
	4	48.72	1.32	0.91	0.37	1.11	44.69	0.15	2.30
	6	48.33	1.94	1.24	0.49	1.58	41.86	0.20	3.74

Table 6.4. Multiplicity fractions for different particle species.

$= 2$, which increases to $\sim 6.9\%$. Finally, the BH radiates very little via the Higgs channel. It turns out that the multiplicity and energy fractions have very weak dependence on n , as well as **GRAVITONLOSS**.

Table (6.6) shows other properties: the initial Hawking temperature T_H , lifetime τ , multiplicity N , initial entropy S_0 , and the total cross sections σ at $\text{XMIN} = \text{QMIN} = 1, \text{GRAVITONLOSS} = \alpha = 0$. NP does not affect the results ¹. As predicted by Eq.s (4.32) and (5.22), the Hawking temperature T_H increases with M_* and n , as confirmed by the simulation. As the temperature becomes higher at higher M_* and n , the lifetime τ is expected to be smaller. Moreover, the initial entropy S_0 (or the multiplicity N) decreases with M_* and n according to

¹NP only affects the Planck phase, so it does not affect these quantities. Note that CATFISH calculates τ by assuming the BH evaporates via Hawking radiation completely, and N is given by Eq.(6.2).

M_* (TeV)	NP	Percentage (%)			
		Higgs	Fermions	Gauge bosons	Gravitons
1	0	0	77.92	21.89	0
	2	0.09	74.18	23.42	1.91
	4	0.14	73.91	23.42	2.09
	6	0.15	73.73	23.65	2.02
2	0	0	81.43	18.40	0
	2	0.17	74.17	22.15	2.90
	4	0.25	72.48	22.44	4.12
	6	0.26	72.32	22.50	4.15
3	0	0	85.02	14.87	0
	2	0.25	75.31	20.98	2.33
	4	0.34	72.20	21.28	5.14
	6	0.36	71.05	21.61	5.91
4	0	0	88.57	11.39	0
	2	0.29	75.33	19.85	2.25
	4	0.43	72.05	20.43	5.44
	6	0.46	70.54	20.70	6.85

Table 6.5. Energy fractions for different particle species.

Eq.(6.3) (or Eq.(6.2)), which also contributes to the decrease in τ . This table also shows that the total cross section σ decreases quite a lot as M_* increases, while it becomes a little bit bigger for higher n .

6.1.4 Other Black Hole Event Generators

There are other BH event generators: TRUENOIR [79], CHARYBDIS2 [80, 81] and BlackMax [82, 83]. The TRUENOIR generator is a plug-in module for the PYTHIA Monte Carlo package. It simulates the production and decay of BHs based on a heuristic algorithm and the conservation of baryon and lepton numbers, as well as the color charges. It assumes that the evolution of the BH includes only the Hawking evaporation phase. A fast-decay approximation is used to simulate the decay of a BH.

M_* (TeV)	n	T_H (TeV)	$\tau(\times 10^{-23}\text{s})$	N	$S_0(k_B)$	σ (pb)
1	4	0.213	20.1	120	350	2571
	6	0.366	3.96	69	214	2778
2	4	0.490	3.81	52	152	33.1
	6	0.808	0.813	31	96.8	36.4
3	4	0.797	1.44	32	93.6	0.984
	6	1.28	0.322	20	60.9	1.09
4	4	1.13	0.722	23	66.2	0.029
	6	1.78	0.167	14	43.9	0.032

Table 6.6. Basic properties of BHs simulated by CATFISH: Hawking temperature T_H , lifetime τ , multiplicity N , entropy S_0 and cross section σ .

CHARYBDIS [80] interfaces, via the Les Houches accord, to general purpose Monte Carlo programs such as HERWIG and PYTHIA. Compared with TRUEOIR, CHARBDIS takes the graybody factors into account. It also includes the change in the Hawking temperature as the decay progresses and is designed for simulations with either $p - p$ or $\bar{p} - p$. The new release, CHARYBDIS2 [81], incorporates the effects of the rotation on the Hawking radiation and different models for the Planck phase.

BlackMax is also interfaced with HERWIG and PYTHIA via the Les Houches accord. It includes all of the BH graybody factors and implements the effects of BH rotation, splitting between the fermions, nonzero brane tension, and BH recoil due to Hawking radiation.

6.2 Lower Limits on M_* and M_{\min}

In Ref.[4], the CMS Collaboration searched for microscopic BHs, using a data sample of pp collisions at $\sqrt{s} = 8$ TeV. The corresponding integrated luminosity was 12.0 fb^{-1} . The search was based on a search for a deviation from the SM background predictions in the S_T (defined below) spectra observed in data. There was no excess of data over the background prediction, so the CMS Collaboration

set limits on BH production rates, that is, the model-independent limits on the cross section times the acceptance (A). These limits can be used to constrain specific models of BH physics resulting in energetic, multiparticle final states, and in this dissertation, the lower limits on M_* and M_{\min} will be presented, derived from the cross section limits published in Ref.[4].

In the following section, the analysis done by the CMS Collaboration is briefly described, along with the model-independent cross section limits. The next section 6.2.1 is based on Ref.[4].

6.2.1 Model-Independent Cross Section Limits

6.2.1.1 S_T variable and multiplicity N

The collision of protons produces various particles at the LHC. Among them, jets, photons, electrons and muons are the so-called objects included in the analysis. To identify and isolate these objects, the CMS Collaboration used several object definitions and isolation requirements. In the following, the variable $\text{Iso}(\iota)$ refers to the isolation requirement for a particular object, and it is either the sum of transverse momenta p_T 's of all charged and neutral particles in a cone of $\Delta R = \sqrt{(\Delta\phi)^2 + (\Delta\eta)^2} = \iota$ around the object, or the ratio of that sum to the object's p_T , depending on the context. Here, η is the pseudorapidity of a particle,

$$\eta = \frac{1}{2} \ln \frac{p + p_z}{p - p_z} = -\ln \left(\tan \frac{\theta}{2} \right), \quad (6.6)$$

and θ is the polar angle and ϕ is the azimuthal angle defined by Fig.(6.2), showing the coordinate system used by the CMS detector.

1. Jets are reconstructed by clustering the particles with the anti- k_T algorithm [84]. A distance parameter is set to 0.5. Further requirements are $p_T > 50$ GeV and $|\eta| < 2.6$.

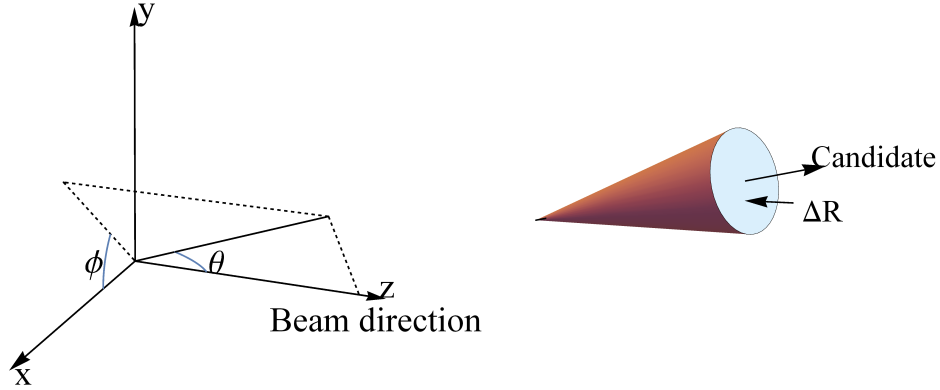


Fig. 6.2. Left: The coordinate system of the CMS detector. The beam direction is parallel or anti-parallel to the z direction. y is pointing upward and x is pointing into the center of the LHC ring. Right: The diagram showing the cone used to define the variable $\text{Iso}(\iota)$.

2. Muons are required to have $|\eta| < 2.1$ and $p_T > 50$ GeV. The impact parameter should be less than 0.2 cm. In addition, $\text{Iso}(0.3) < 20\%$.
3. Electrons must have $p_T > 50$ GeV and lie within the barrel ($|\eta| < 1.44$) and endcap ($1.56 < |\eta| < 2.4$). The separation ΔR between the electron candidate and any muon candidate that has over 10 hits in the inner tracker is required that $\Delta R > 0.1$. Again, $\text{Iso}(0.3) < 20\%$.
4. Photons must also have $p_T > 50$ GeV and lie within the regions $|\eta| < 1.44$ and $1.56 < |\eta| < 2.4$. The ratio of HCAL and ECAL energy deposits should be less than 5%. The ratio $\text{Iso}(0.4)$ should not be greater than 2.0, 4.2, and 2.2 GeV for the tracker, ECAL, and HCAL, respectively.

The missing transverse energy \cancel{E}_T is also important in the search for BHs, since a BH event tends to have large \cancel{E}_T . It is the absolute value of the vector sum of the transverse momenta of all the objects reconstructed in an event. Finally, the minimum separation between any two objects (jet, lepton, or photon) in the event is required to be $\Delta R > 0.3$.

As soon as objects are reconstructed and \cancel{E}_T is calculated, the S_T variable is given by the scalar sum of transverse energies of all objects in the event in excess of 50 GeV, and \cancel{E}_T is added to it if $\cancel{E}_T > 50$ GeV,

$$S_T = \sum_{\text{Objects}} p_T + \cancel{E}_T. \quad (6.7)$$

Then, the multiplicity N of the objects can be determined, i.e., N is the number of objects used for the calculation of S_T .

6.2.1.2 Data samples

The SM background is completely dominated by QCD multijet production. In their analysis, the CMS Collaboration estimated the QCD multijet production directly from data using the empirical observation that the shape of the S_T spectrum is roughly independent of N . So the shapes of the S_T spectrum for any N can be estimated by fitting to the dijet data $N = 2$. The dijet mass spectrum does not show any signal-like features in the range of $1.8 < S_T < 2.8$ TeV, so it was used to obtain the background shape. The background shape was then parametrized with a suitable function. To get higher multiplicity S_T spectra, the control region ($1.9 < S_T < 2.3$ TeV) was selected, and the scaling of background to higher multiplicities was performed by normalizing the background shape to data in each inclusive multiplicity bin in the control region. The small backgrounds from $\gamma + \text{jets}$, $W/Z + \text{jets}$ (or $V + \text{jets}$) and $t\bar{t}$ production were obtained using the MadGraph v5 [85] matrix element event generator interfaced with the PYTHIA [76] parton showering simulation, followed by the full detector simulation with GEANT4 [86]. The PDF used was CTEQ6L [87].

The signals, i.e., microscopic BH events, were simulated using the parton-level BlackMax v2.01 and CHARYBDIS Monte Carlo event generators. The simulated models included rotating and non-rotating BHs, BHs with or without mass and

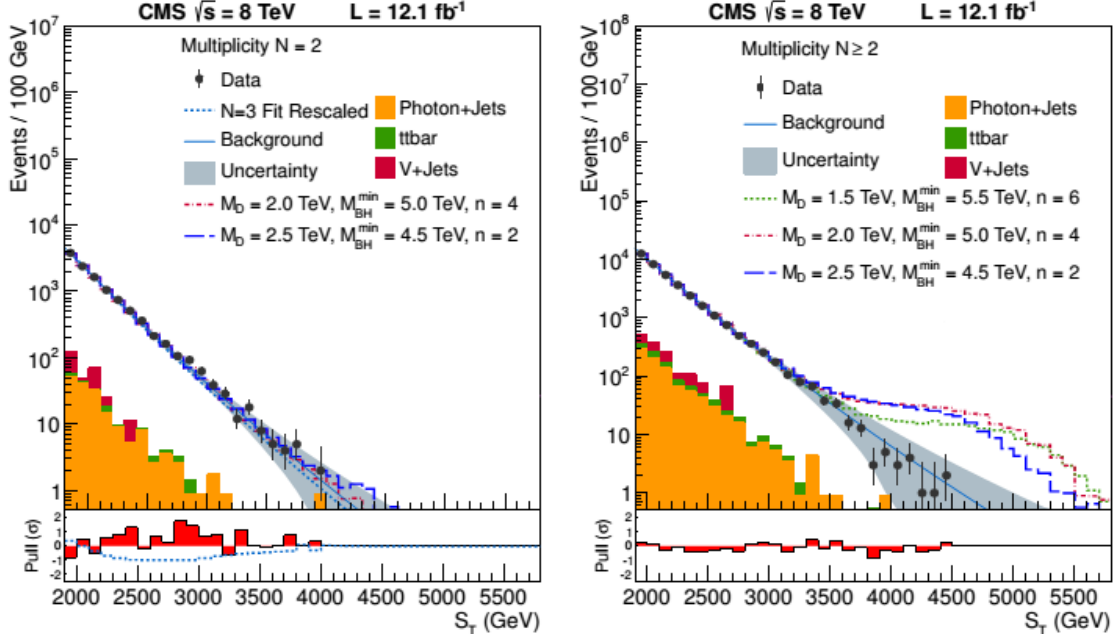


Fig. 6.3. Figure 1 in Ref.[4]. The S_T spectra for events with (left) $N = 2$ and (right) $N \geq 2$. Observed data are depicted as points with statistical error bars; the solid line with a shaded band is the multijet background prediction from $N = 2$ fit and its systematic uncertainty. Colored histograms represent small backgrounds. Also shown are the expected BH signals for 3 parameter sets of the BlackMax nonrotating BH model. Here, $M_{\text{BH}}^{\text{min}}$ is M_{min} in Section 6.1. The bottom panels in each plot show the pull distribution (defined as $(\text{data}-\text{background})/\sigma(\text{data}-\text{background})$) based on combined statistical and systematic uncertainty. For more detail, please refer to Ref.[4].

angular momentum loss at the formation, and those with or without a stable or “boiling” (i.e., evaporating at a fixed Hawking temperature) remnant. These parton-level events were then fed into the PYTHIA v6.426 parton showering simulation and a fast parametric simulation Delphes (see Section 7.3.1). Fig.(6.3) shows the S_T spectra for events with (left) $N = 2$ and (right) $N \geq 2$, together with data, predicted background and the back hole simulation results using BlackMax for 3 different parameter sets for a nonrotating BH model.

6.2.1.3 Results

As shown in Fig.(6.3), there is no excess of data over the background prediction, so the model-independent cross section times A upper limits were determined for high- S_T inclusive final states for $N \geq 3, \dots, 10$, as a function of minimum S_T . These limits are shown in Fig.s(6.4) and (6.5). Fig.(6.6) shows lower BH mass limits for various models by analyzing simulation results from BlackMax and CHARYBDIS2. Regions below each curve are excluded by the analysis.

6.2.2 Results from CATFISH

The results reported here have been published in Ref. [88]. So this section is mainly based on Ref. [88].

6.2.2.1 The S_T spectra

Several samples of BH events were simulated by CATFISH. The sample models considered here ignore graviton energy loss ($\text{GRAVTTONLOSS} = 0$) and GUP effects ($\alpha = 0$; $\alpha \neq 0$ will be the topic of Chapter 7). As an example, the fundamental Planck scale is chosen to be $M_* = 1$ TeV, and it is assumed that there are 4 LED's. The BHs formed have masses of at least 3, 4 or 5 times that of M_* and they decay into $\text{NP} = 2, 4$ or 6 final quanta or settle down to a remnant ($\text{NP} = 0$) in the Planck phase. The S_T spectra at different multiplicities (N 's) are obtained as shown in Fig.'s (6.7) and (6.8). Also shown are observed data (dots), and the green curves represent the S_T spectra for the SM processes fitting the predicted background spectra obtained by the CMS Collaboration to the function $P_0(1+x)^{P_1}/x^{P_2+P_3 \log(x)}$ with $x = S_T/\sqrt{s}$ [4].

To obtain the S_T spectra, several kinematic cuts were applied. They are listed in Table (6.7). In this table, kinematic cuts are directly applied to quarks and

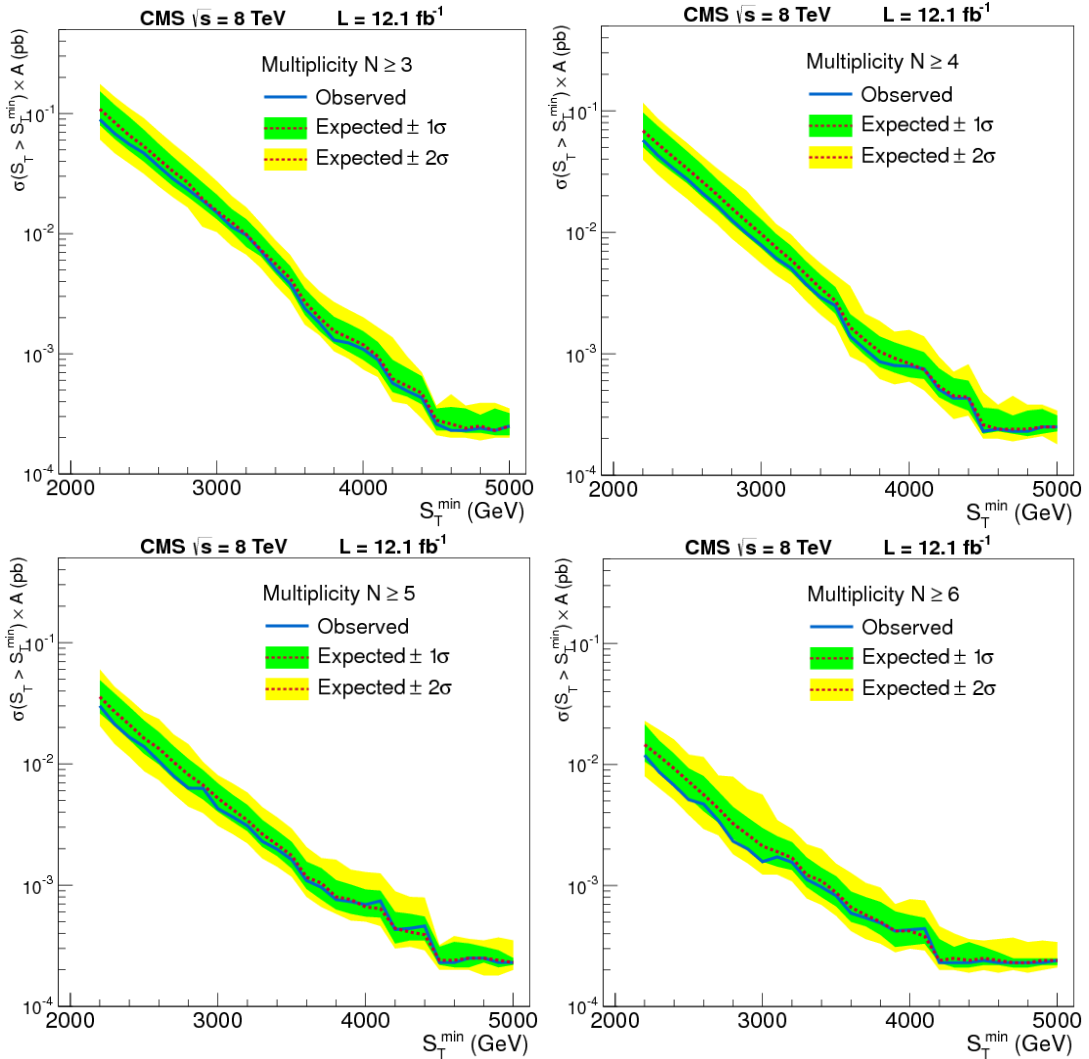


Fig. 6.4. Model-independent 95% CL cross section times acceptance (A) upper limits for counting experiments with $S_T > S_T^{\min}$ as a function of S_T^{\min} for events with multiplicity: (top left) $N \geq 3$, (top right) $N \geq 4$, (bottom left) $N \geq 5$, and (bottom right) $N \geq 6$. The blue solid (red dotted) lines correspond to an observed (expected) limit. The green (dark) and yellow (light) bands represent one and two standard deviations from the expected limits. Graphs are taken from Figure 6 in Ref.[4].

gluons because only parton level events were analyzed, that is, hadronization was turned off.

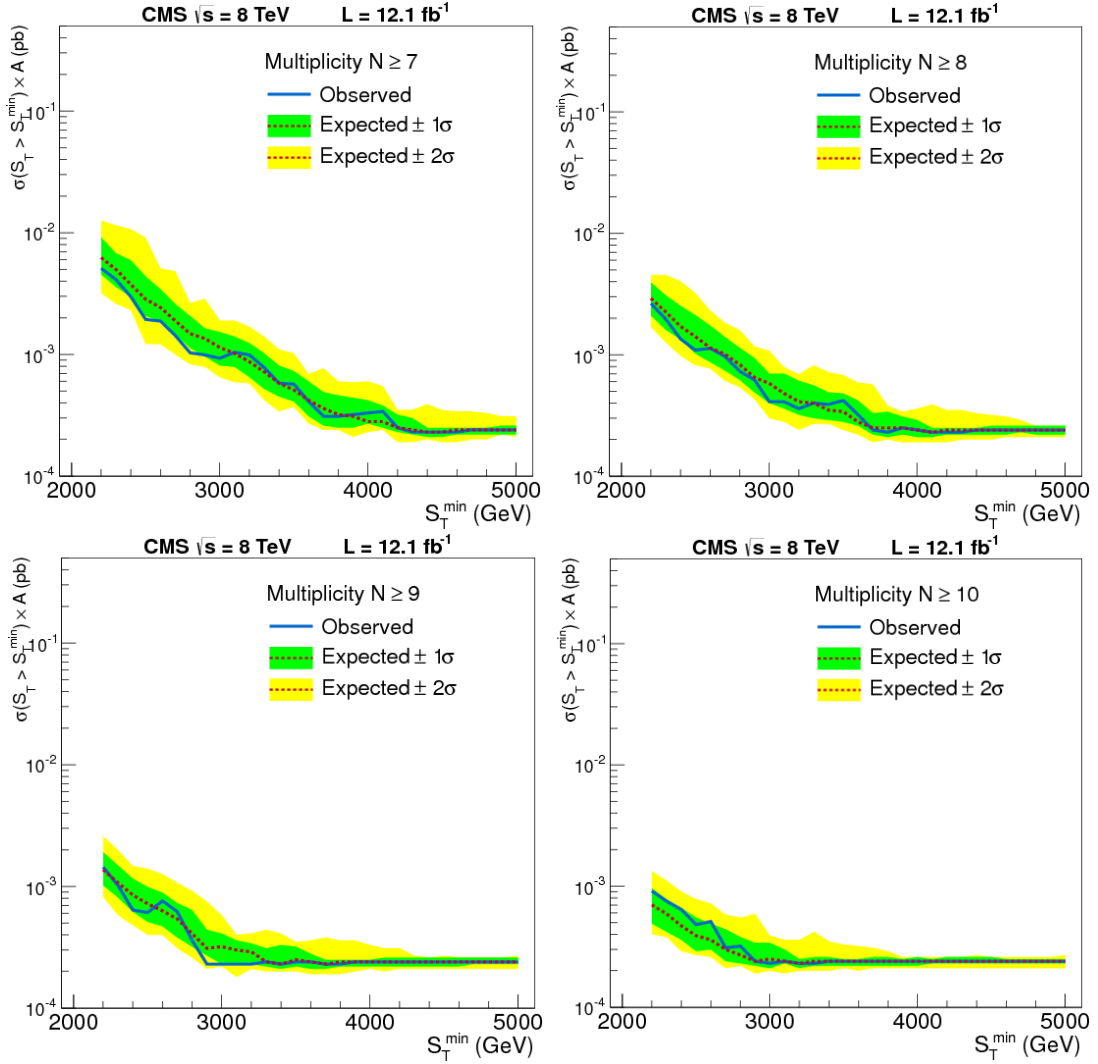


Fig. 6.5. Model-independent 95% CL cross section times acceptance (A) upper limits for counting experiments with $S_T > S_T^{\min}$ as a function of S_T^{\min} for events with multiplicity: (top left) $N \geq 7$, (top right) $N \geq 8$, (bottom left) $N \geq 9$, and (bottom right) $N \geq 10$. The blue solid (red dotted) lines correspond to an observed (expected) limit. The green (dark) and yellow (light) bands represent one and two standard deviations from the expected limits. Graphs are taken from Figure 7 in Ref.[4].

6.2.2.2 Lower limits on M_* and M_{\min}

Lower bounds on M_* and M_{\min} are obtained by using the model-independent cross section limits in Fig.'s (6.4) and (6.5). The first step is to evaluate the partial

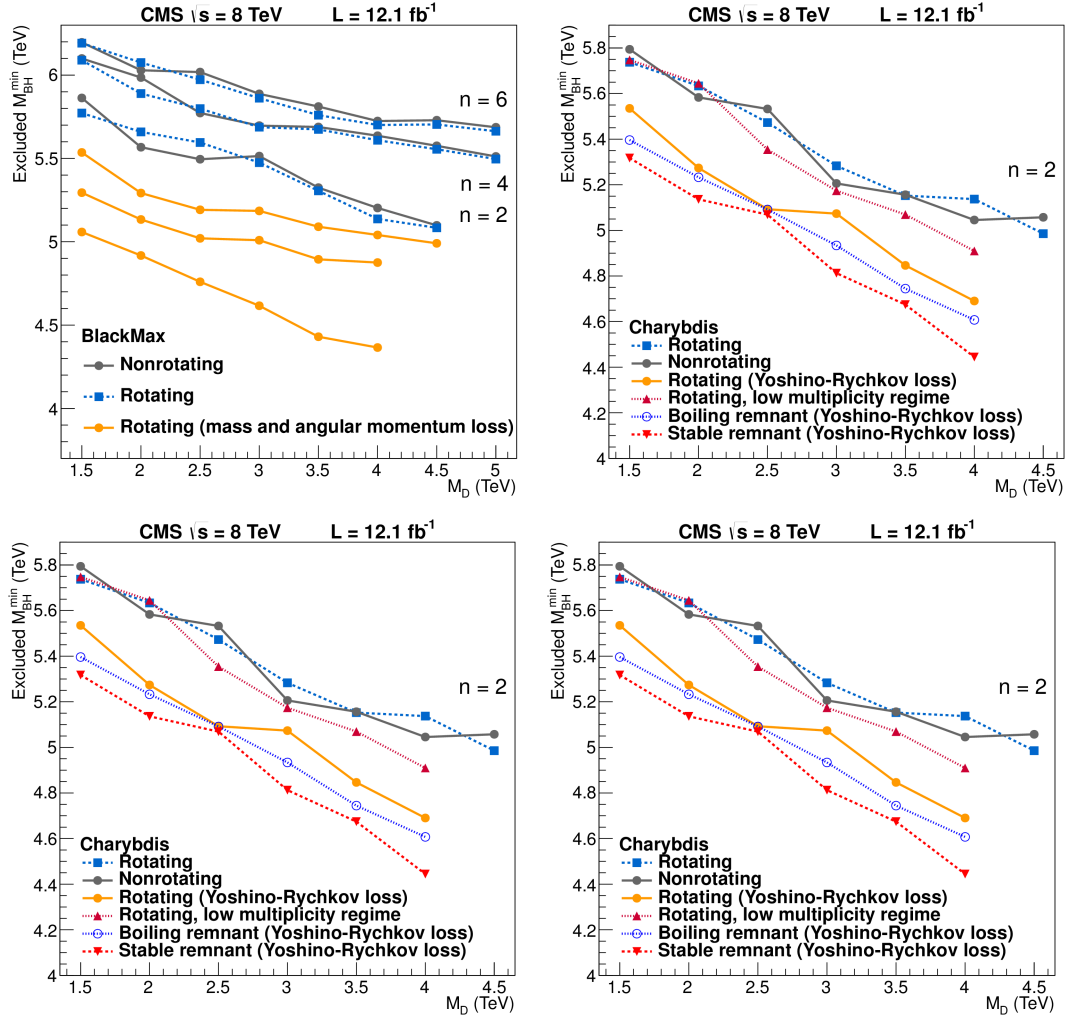


Fig. 6.6. The 95% CL lower limits on the BH mass derived from the upper 95% CL limits on cross section times branching fraction as a function of M_D for various models. The areas below each curve are excluded. Graph are taken from Figure 4 in Ref.[4].

cross section $\sigma(S_T > S_T^{\text{min}})$. It should be smaller than the experimental limits. $\sigma(S_T > S_T^{\text{min}})$ is calculated for events whose $S_T > S_T^{\text{min}}$ and whose multiplicities are greater than some chosen value given by,

$$\sigma(S_T > S_T^{\text{min}}) = k \cdot \sigma_{pp \rightarrow \text{BH}}, \quad (6.8)$$

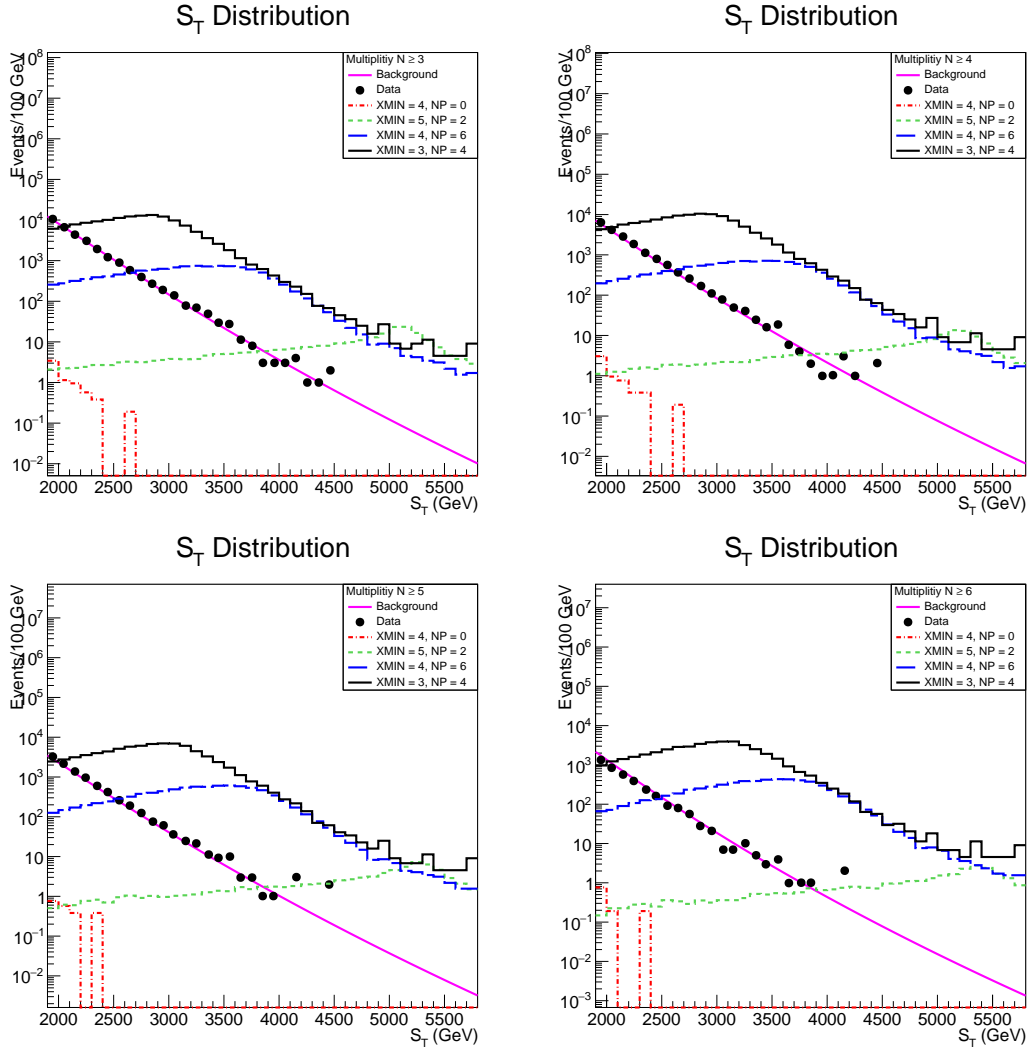


Fig. 6.7. The S_T for events with different multiplicities. Dots represent observed spectra and the green solid lines represent the predicted background distributions, which are taken from Figure 2 in Ref.[4]. The BH signals are also shown.

where k is

$$k = \frac{\text{Num. of events with } S_T > S_T^{\min}}{\text{Total Num. of events}}. \quad (6.9)$$

The behavior of the total cross section $\sigma_{pp \rightarrow \text{BH}}$ (refer to Eq.(4.57)) as a function of M_* and M_{\min} (i.e., XMIN) follows from Eqs.(4.57). There are 3 factors: 1) The BD cross section σ_{BD} is inversely proportional to a power of M_* ; 2) Since

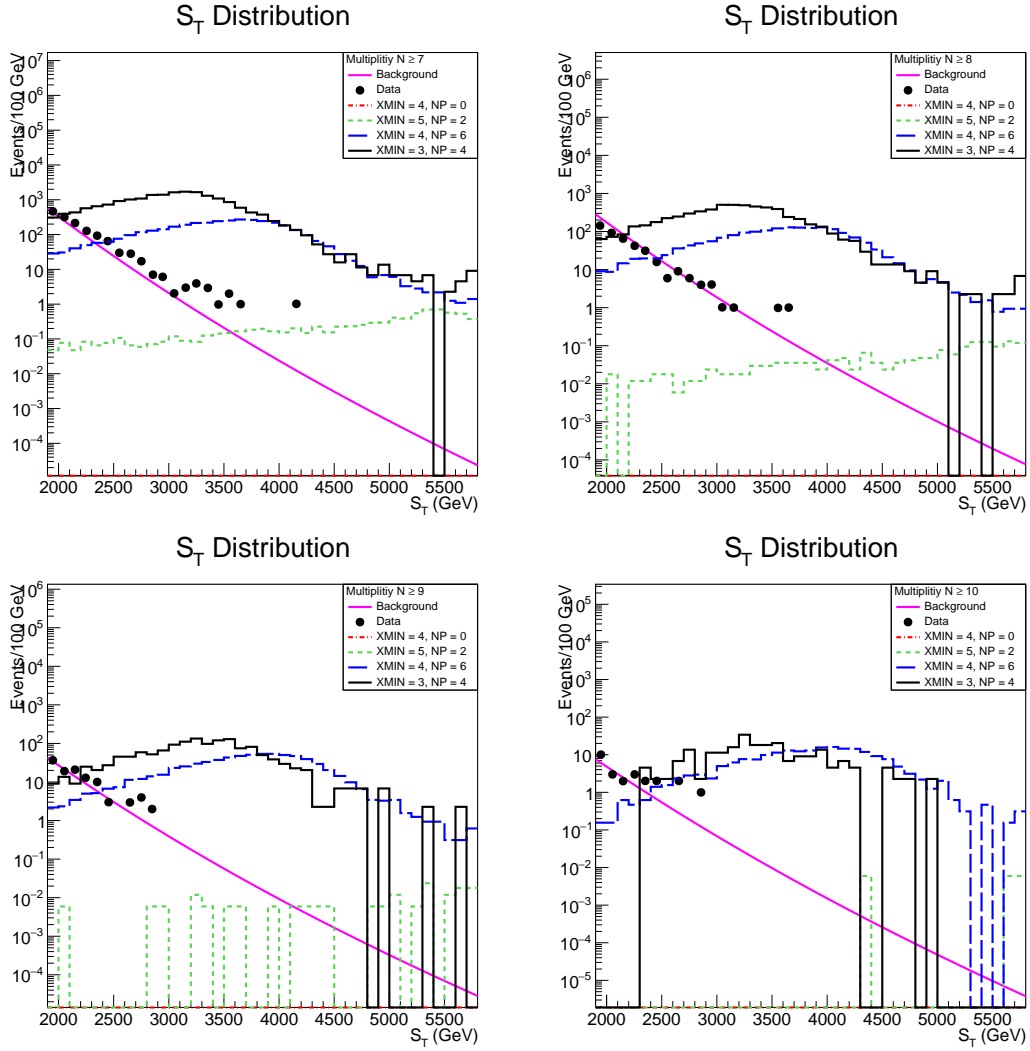


Fig. 6.8. The S_T for events with different multiplicities. Dots represent observed spectra and the green solid lines represent the predicted background distributions, which are taken from Figure 2 in Ref.[4]. The BH signals are also shown.

XMIN appears in the lower limit of integration in the total cross section $\sigma_{pp \rightarrow \text{BH}}$, the greater XMIN, the smaller $\sigma_{pp \rightarrow \text{BH}}$ is at a fixed M_* ; 3) In addition, the PDFs fall off rapidly at high x . Taking into account all these factors, $\sigma_{pp \rightarrow \text{BH}}$ is expected to decrease as M_* (XMIN) increases at fixed XMIN (M_*). The ratio k in Eq.(6.9) can be estimated by integrating the spectra of visible final state particles over the range $S_T > S_T^{\text{min}}$ and then averaging over all final state particles. k is an increasing

Objects	p_T	$ \eta $	Iso(l)
quarks & gluons	> 50 GeV	< 2.6	N/A
muons		< 2.1	Iso(0.3) $< 20\%$
electrons		(1.56, 2.4) &	
photons		(0, 1.44)	

Table 6.7. Kinematic cuts employed to obtain the S_T spectra.

function of the Hawking temperature T_H , which is thus a monotonically increasing function of M_* . Therefore, as M_* increases, the graph of k vs. S_T^{\min} flattens. Following the CMS Collaboration ², the signal acceptance, A , is chosen to be 100%. In summary, $\sigma(S_T > S_T^{\min}) \times A$ is expected to decrease as either M_* or X_{\min} increases. Therefore, lower limits on M_* and X_{\min} can be determined.

The partial cross section $\sigma(S_T > S_T^{\min})$ as a function of M_* is obtained by running CATFISH with fixed NEXTRADIM, GRAVITONLOSS, $X_{\min} = Q_{\min}$, NP. The results are shown by the upper two graphs in Figure (6.9) for NEXTRADIM = 3, $X_{\min} = Q_{\min} = 5$, NP = 0, 4. The lower two graphs in Figure (6.9) display $\sigma(S_T > S_T^{\min})$ as a function of X_{\min} for $M_* = 1.5$ TeV, NEXTRADIM = 5, and NP = 0, 4. As expected, Figure (6.9) shows that the cross section decreases as M_* and X_{\min} increase.

Figure (6.9) can be used to determine bounds on M_* and X_{\min} by comparing the simulated $\sigma(S_T > S_T^{\min})$ with the experimental limits (the solid curves in the graphs). For example, the upper right plot shows that the lower limit on M_* lies in the range 1.0 TeV–1.2 TeV, and the bottom right plot shows that the lower limit on X_{\min} lies in the range 3.7–3.9. Multiplying this range by $M_* = 1.5$ TeV, we obtain the lower limits on $M_{\min} = 5.55$ TeV–5.85 TeV.

CATFISH ran over a large range of parameter space and required the simulated $\sigma(S_T > S_T^{\min})$ to be less than the experimental limits for all multiplicities $N \geq 3, 4, \dots, 10$. Figure (6.10) shows the exclusion region for M_* . As expected, the

²G. Landsberg, private conversation.

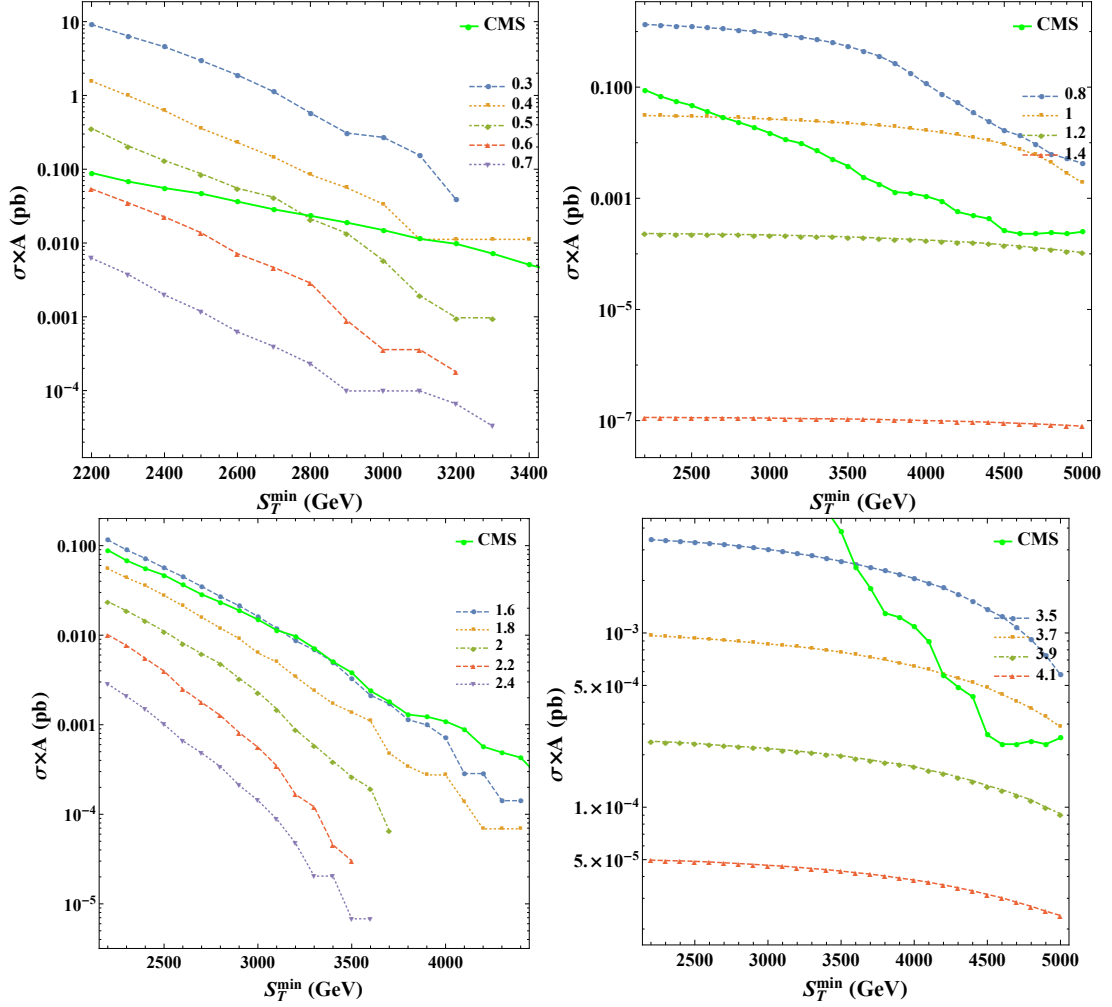


Fig. 6.9. $\sigma(S_T > S_T^{\min}) \times A$ as a function of M_* (Upper two graphs, numbers being M_* 's chosen in units of TeV) or XMIN (Lower two graphs, numbers being XMIN's) at NP = 0 (Left two graphs) and NP = 4 (Right two graphs). The model-independent 95% CL experimental upper limits for counting experiments from CMS Collaboration are also shown. The multiplicity is $N \geq 3$.

lower limit $M_{*, \text{exp}}$ is a decreasing function of XMIN. The value of $M_{*, \text{exp}}$ does not strongly depend on NP, as long as $\text{NP} \neq 0$. If $\text{NP} = 0$, the bound on $M_{*, \text{exp}}$ becomes much smaller. This is due to the high transverse momentum carried by the BH remnant, which contributes to the missing energy. The lower limits on M_* set upper bounds on M_{\min} (XMIN). As experimental data exclude values of $M_* \lesssim 1$

TeV[64], our results for $\text{NP} = 0$ set an upper limit $\mathbf{XMIN} \lesssim 2.5$. $\text{NP} \neq 0$ results give the milder constraint, $\mathbf{XMIN} \lesssim 6$. More experimental limits are shown in Table 3.3, leading to more stringent constraints. For instance, CMS searches for events with an energetic jet and an imbalance in transverse momentum at $\sqrt{s} = 8$ TeV [30] set the lower limit $M_* \sim 2.71$ TeV for $n = 3$. The upper left panel in Figure (6.10) shows that the events with microscopic BHs decaying to remnants ($\text{NP} = 0$) are excluded, and the experimentally allowed range of \mathbf{XMIN} is restricted to $1 \sim 2$ for $\text{NP} \neq 0$. The lower limits of M_* for $n = 4, 5, 6$ do not exclude events with remnants as BH final products, but never the less, they set strong constraints on the ranges where the semi-classical treatment is valid.

Figure (6.11) shows the exclusion region for \mathbf{XMIN} . As expected, the lower limit of \mathbf{XMIN} is a decreasing function of M_* . Figure (6.11) also shows that these limits do not depend on NP strongly when $\text{NP} \neq 0$, but become much smaller at $\text{NP} = 0$. This figure can be combined with Figure (6.10) to constrain M_* further. For example, if there are 3 extra dimensions, and a BH decays into 2 quanta in the quantum phase, the dashed curve ($\text{NP} = 2$) in the upper left plot shows that $\mathbf{XMIN} \gtrsim 4$ at $M_* \sim 1.5$ TeV. At the same time, the dashed curve in the upper left plot ($n = 3$) of Figure (6.10) indicates that if $\mathbf{XMIN} = 4$, $M_* \gtrsim 1.5$ TeV. This shows that the lower limits of M_* are consistent with those of \mathbf{XMIN} . In Figure (6.11), the ranges of M_* were chosen in order to compare the CATFISH results with those of BlackMax and CHARYBDIS2 from Ref.'s [4, 5].

Figure (6.12) compares the lower limits of M_{\min} predicted by CATFISH with those from BlackMax and CHARYBDIS2 done by the CMS Collaboration [4]. It shows that as long as $\text{NP} = 0$, CATFISH's limits are much smaller than those of BlackMax and CHARYBDIS2. The difference in predictions between CATFISH and CHARYBDIS2 when a stable remnant model is produced is due to the different treatments of the Planck phase by the two generators [4, 80, 81]. Moreover, CATFISH's stable remnant is invisible to the detector and contributes to missing

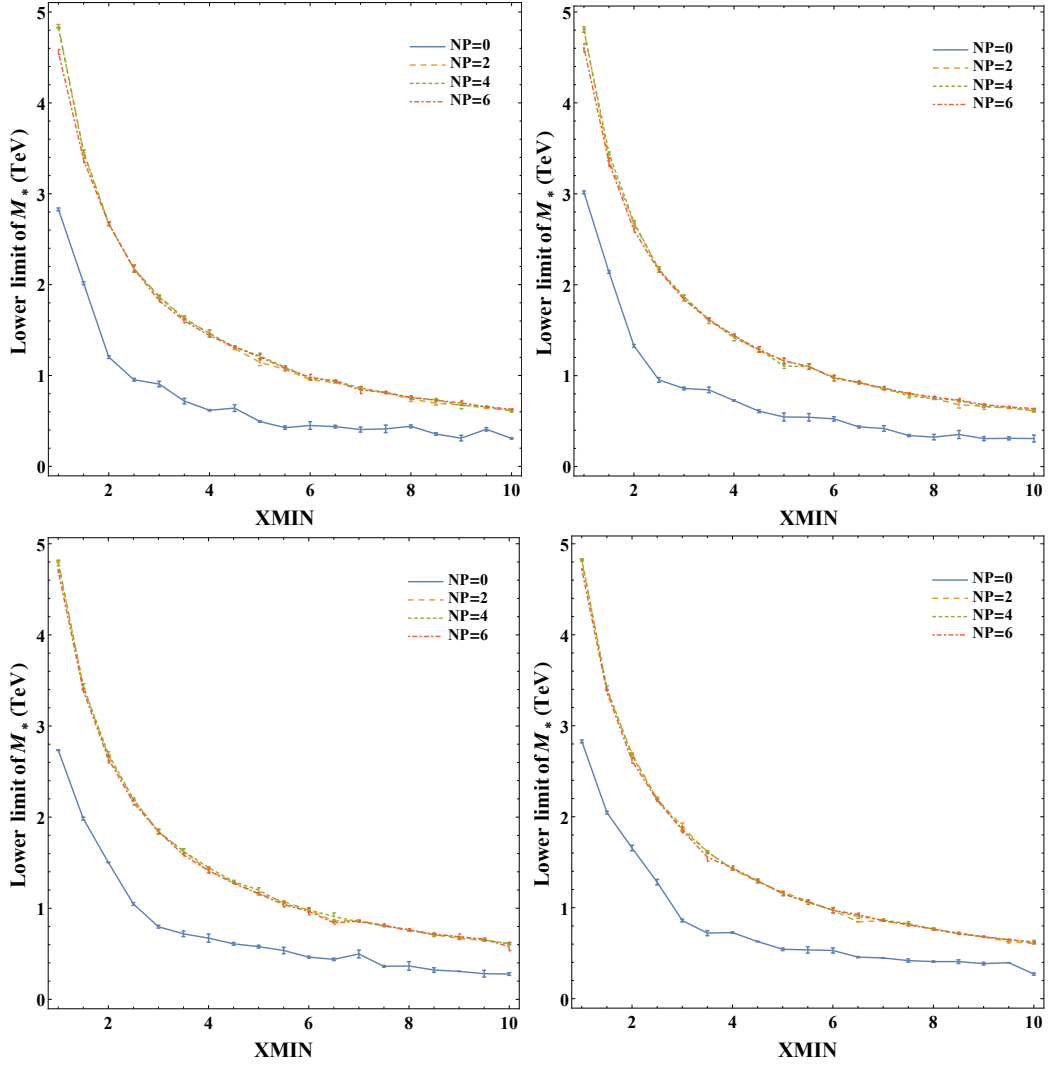


Fig. 6.10. Simulated lower limit on M_* vs. $XMIN$ as a function of NP and $N_{EXTRADIM} = 3$ (top left), 4 (top right), 5 (bottom left), and 6 (bottom right).

energy, while CHARYBDIS2's remnant behaves as a heavy fundamental particle with conventional interactions in the detector. If $NP \neq 0$, the situation is more complicated. CATFISH agrees with BlackMax (nonrotating BH model) very well when $n = 4$, but gives higher limits than BlackMax if $n = 6$. CATFISH gives limits similar to those of CHARYBDIS2 (nonrotating BH model) for $n = 4, 6$. Figure (6.13) shows the comparison between CATFISH predictions with those from the

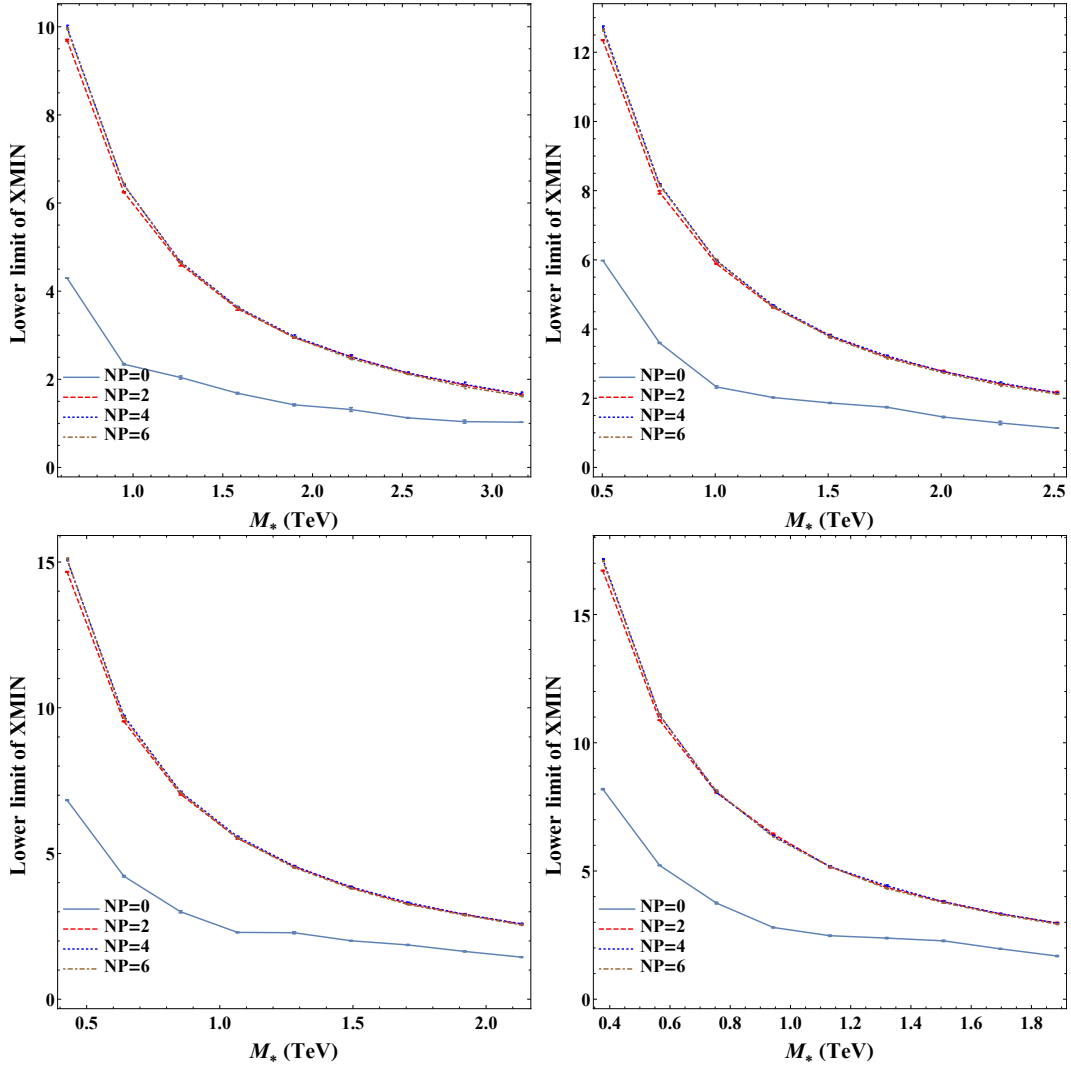


Fig. 6.11. Simulated lower limit on XMIN vs. M_* as a function of NP and NEXTRADIM = 3 (top left), 4 (top right), 5 (bottom left), and 6 (bottom right).

ATLAS Collaboration [5]. CATFISH agrees with BlackMax and CHARYBDIS2 when $NP \neq 0$, but predicts much smaller limits when $NP = 0$. The similarities among the three generators as shown in the two figures for M_{\min} vs M_* for $NP \neq 0$ are due to the fact that the three generators incorporate the same basic physics of microscopic BH formation and decay. However, the three generators differ from one another in the implementation of the Planck phase and in the inclusion or

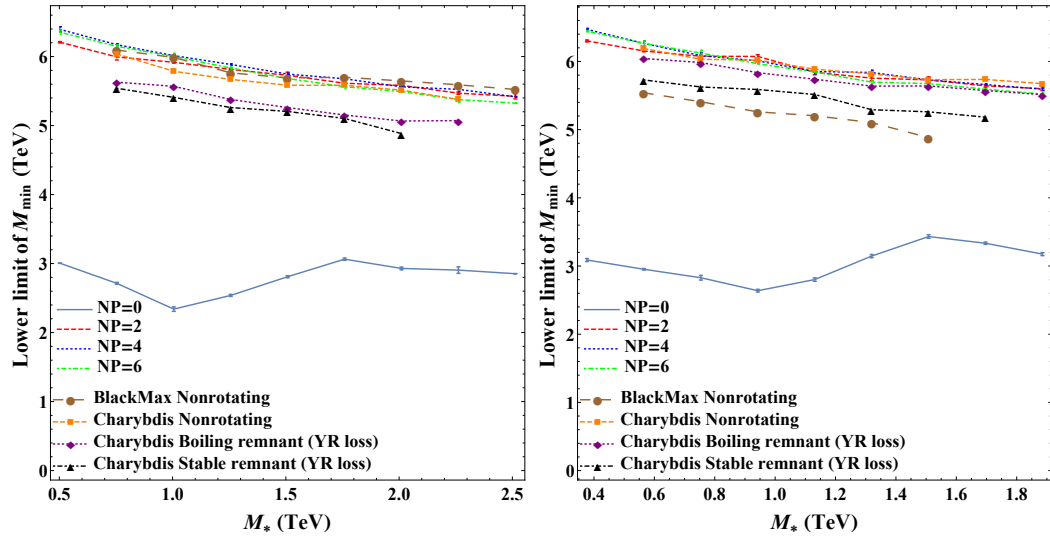


Fig. 6.12. Comparison of the predictions on lower limits of M_{\min} from CATFISH with those from BlackMax and CHARYBDIS2 at NEXTRADIM = 4 (left) and 6 (right). The results of BlackMax and CHARBDIS are extracted from Fig. 4 in Ref.[4].

exclusion of the effect of gravitational energy loss at the formation of the BHs. For example, the predictions of the behavior of M_{\min} vs. M_* for NP = 0 (BH remnant) by CATFISH differ from those of BlackMax and CHARYBDIS2.

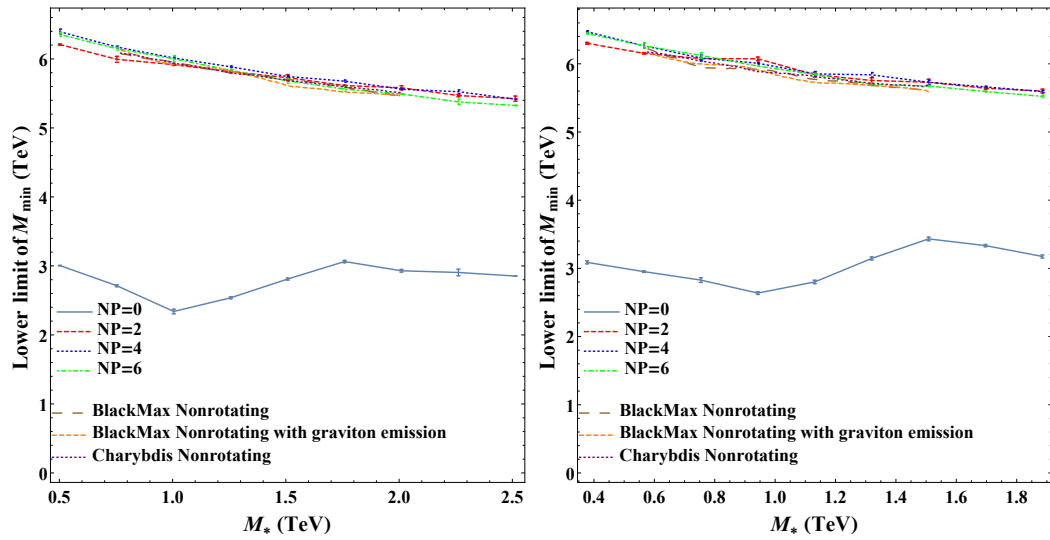


Fig. 6.13. Comparison of the predictions on lower limits of M_{\min} from CATFISH with those from BlackMax and CHARYBDIS2 at $NEXTRADIM = 4$ (left) and 6 (right). The results of BlackMax and CHARBDIS are extracted from Fig.'s 8 and 10 in Ref.[5].

7 GENERALIZED UNCERTAINTY PRINCIPLE AND BLACK HOLES

The Planck scale is the energy scale where the effects of quantum gravity start to take place. The black hole produced from particle collisions might have large enough initial mass so that the semi-classical treatment can be applied to study its evolution, as was done in the previous chapter, but its mass will eventually decrease to the Planck mass due to Hawking radiation. Therefore, quantum gravity must influence the decay of a black hole. Although there is no a well established quantum theory of gravity, the generalized uncertainty principle (GUP) is one of the common results of many candidates for quantum gravity, such as string theory, noncommutative geometry, and canonical quantum gravity [64]. So it is interesting to study how the GUP will affect the fate of a BH and its signatures at the LHC.

7.1 Generalized Uncertainty Principle

The GUP is closely related to the postulate of minimal length scale l_m , which might be about the same order as the Planck length l_{Pl} . The usual Heisenberg uncertainty principle $\Delta x \Delta p \gtrsim \hbar$ makes it difficult to probe smaller and smaller distances, because more and more energy is needed. Nevertheless, the distance can be arbitrarily small as long as the energy is arbitrarily large, so there is no smallest nonzero distance in quantum mechanics. If gravity is taken into account, the situation changes, that is, a BH will form if the energy is large enough and if

it is accumulated in a small enough region, according to Thorne's hoop conjecture [56]. Since the Planck length l_{Pl} is a natural length scale for phenomena involving gravity, the Heisenberg uncertainty principle might be modified as,

$$\Delta x_i \gtrsim \frac{\hbar}{\Delta p_i} + \alpha^2 l_{\text{Pl}}^2 \frac{\Delta p_i}{\hbar}, \quad (7.1)$$

where $l_{\text{Pl}} = (\hbar G_D / c^3)^{1/(D-2)}$ is the Planck length with $D = n + 4$, α is a dimensionless constant of order one, and the index i labels spatial directions, running from 1 to $n + 3$. This is called the generalized uncertainty principle (GUP). The minimal length scale is given by

$$l_m = 2\alpha l_{\text{Pl}}. \quad (7.2)$$

This length scale not only defines the minimal distance that can be probed, but also restricts the sizes of BHs. The diameter of a BH should be at least l_m , so its mass is greater than M_{ml} , which is given by

$$M_{\text{ml}} = a(\alpha) \cdot M_*, \quad a(\alpha) = \frac{n+2}{8\Gamma(\frac{n+3}{2})} (\alpha\sqrt{\pi})^{n+1}. \quad (7.3)$$

A BH cannot exist when its mass is below M_{ml} .

7.1.1 Implications for Black Hole Physics

There are two major implications of the GUP for BH physics which are implemented in CATFISH. In the following two sections, these implications will be briefly discussed [89, 90].

7.1.1.1 The first implication: M_{ml}

The first implication of the GUP for BH physics is the existence of the minimal mass M_{ml} . Fig.(7.1) shows how M_{ml} varies as a function of α for different numbers

n of LEDs. So M_{ml} is smaller than M_* when $\alpha \lesssim 0.75 \sim 0.8$, and it increases very

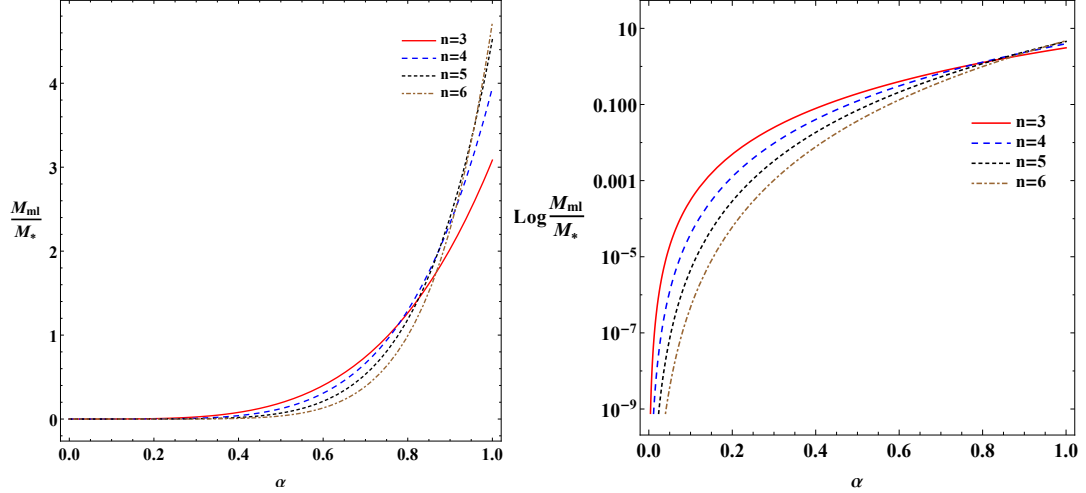


Fig. 7.1. The minimal mass M_{ml} in units of M_* v.s. α for different n . The left graph is in linear scale and the right graph is in log scale.

slowly in this region. Eventually, it surpasses M_* and increases much faster for large α .

The BH mass M_{BH} should certainly be greater than or equal to M_{ml} . At the same time, $M_{\text{BH}} \geq M_*$, so a new variable M_u is defined as $M_u = \text{Max}\{M_*, M_{\text{ml}}\}$, and

$$M_{\text{BH}} \geq M_u. \quad (7.4)$$

This implies that M_u is the energy scale above which a BH might form. In this sense, M_u plays a similar role as M_* when there are no GUP effects.

7.1.1.2 The second implication: Modified Hawking radiation

The second implication of the GUP on BH physics is the modification of Hawking radiation. The generalized uncertainty relation Eq. (7.1) can be solved for

Δp_i ,

$$\frac{2}{\Delta x_i} \left[1 + \sqrt{1 - \frac{4\alpha^2 l_{\text{Pl}}^2}{\Delta x_i^2}} \right]^{-1} \lesssim \Delta p_i \lesssim \frac{2}{\Delta x_i} \left[1 - \sqrt{1 - \frac{4\alpha^2 l_{\text{Pl}}^2}{\Delta x_i^2}} \right]^{-1}. \quad (7.5)$$

At the limit of $l_{\text{Pl}}^2/\Delta x_i \rightarrow 0$, the GUP should reduce to the usual uncertainty relation, so the left inequality will be used in the following discussion. The uncertainty in the energy of the emitted particles is

$$\Delta E \simeq \Delta p_i \sim \frac{2}{\Delta x_i} \left[1 + \sqrt{1 - \frac{4\alpha^2 l_{\text{Pl}}^2}{\Delta x_i^2}} \right]^{-1} \Big|_{\Delta x_i=2R_S} = \frac{1}{R_S} \left[1 + \sqrt{1 - \frac{\alpha^2 l_{\text{Pl}}^2}{R_S^2}} \right]^{-1}. \quad (7.6)$$

The GUP modified Hawking temperature is thus

$$T'_H = \frac{n+1}{2\pi} \Delta E = \frac{n+1}{2\pi R_S} \left[1 + \sqrt{1 - \frac{\alpha^2 l_{\text{Pl}}^2}{R_S^2}} \right]^{-1}. \quad (7.7)$$

When $\alpha \rightarrow 0$, a Taylor expansion gives,

$$T'_H \simeq \frac{n+1}{4\pi R_S} \left(1 + \frac{\alpha^2 l_{\text{Pl}}^2}{4R_S^2} \right) = T_H \left(1 + \frac{\alpha^2 l_{\text{Pl}}^2}{4R_S^2} \right), \quad (7.8)$$

which shows that the GUP modified temperature is higher. Fig.(7.2) shows the ratio T'_H/T_H for different BH masses M_{BH} and n 's. As expected, the modified Hawking temperature is higher than the usual one and is an increasing function of α . The higher temperature implies that the BH radiates at a faster rate.

Replacing T_H by T'_H in Eq.(4.56) and integrating it with $\Omega_H = 0$ leads to the GUP modified entropy,

$$S'_0 = 2\pi\alpha \left(\frac{\alpha}{M_* R_S} \right)^{n+1} \frac{M_{\text{BH}}}{M_*} I \left(1, n, \frac{M_* R_S}{\alpha} \right), \quad (7.9)$$

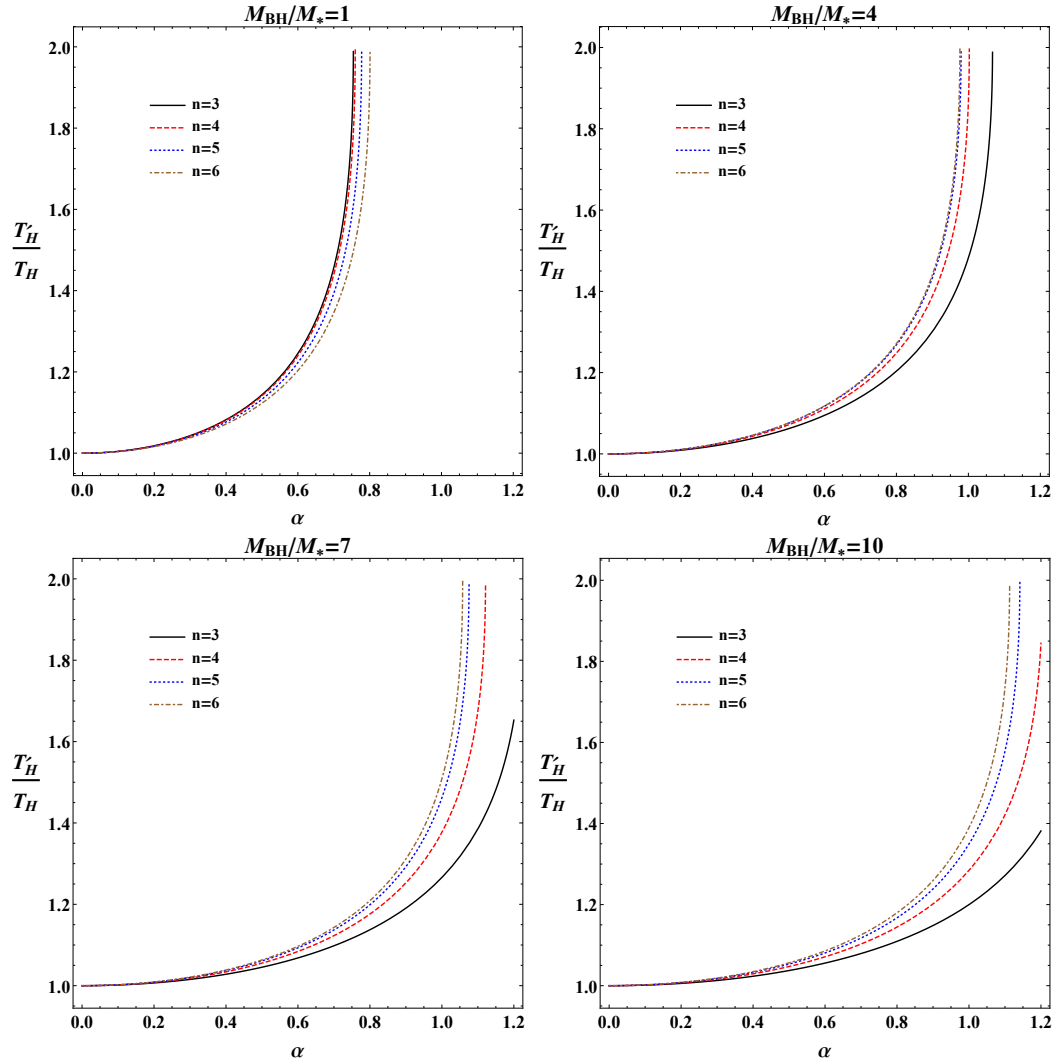


Fig. 7.2. The ratio T'_H/T_H varies as a function of M_{BH}/M_* and n .

where $I(p, q, x) = \int_1^x z^q (z + \sqrt{z^2 - 1})^p dz$. The first order correction to S'_0 is thus

$$\Delta S_0 = -\frac{\pi \alpha^2 M_{\text{BH}}}{n M_*^2 R_S}, \quad (7.10)$$

which implies that the entropy of the BH becomes smaller. Fig.(7.3) shows the ratio S'_0/S_0 v.s. n at different M_{BH}/M_* 's. It shows that the GUP modified initial entropy S'_0 becomes smaller and smaller with α for any number of LEDs. S'_0 almost

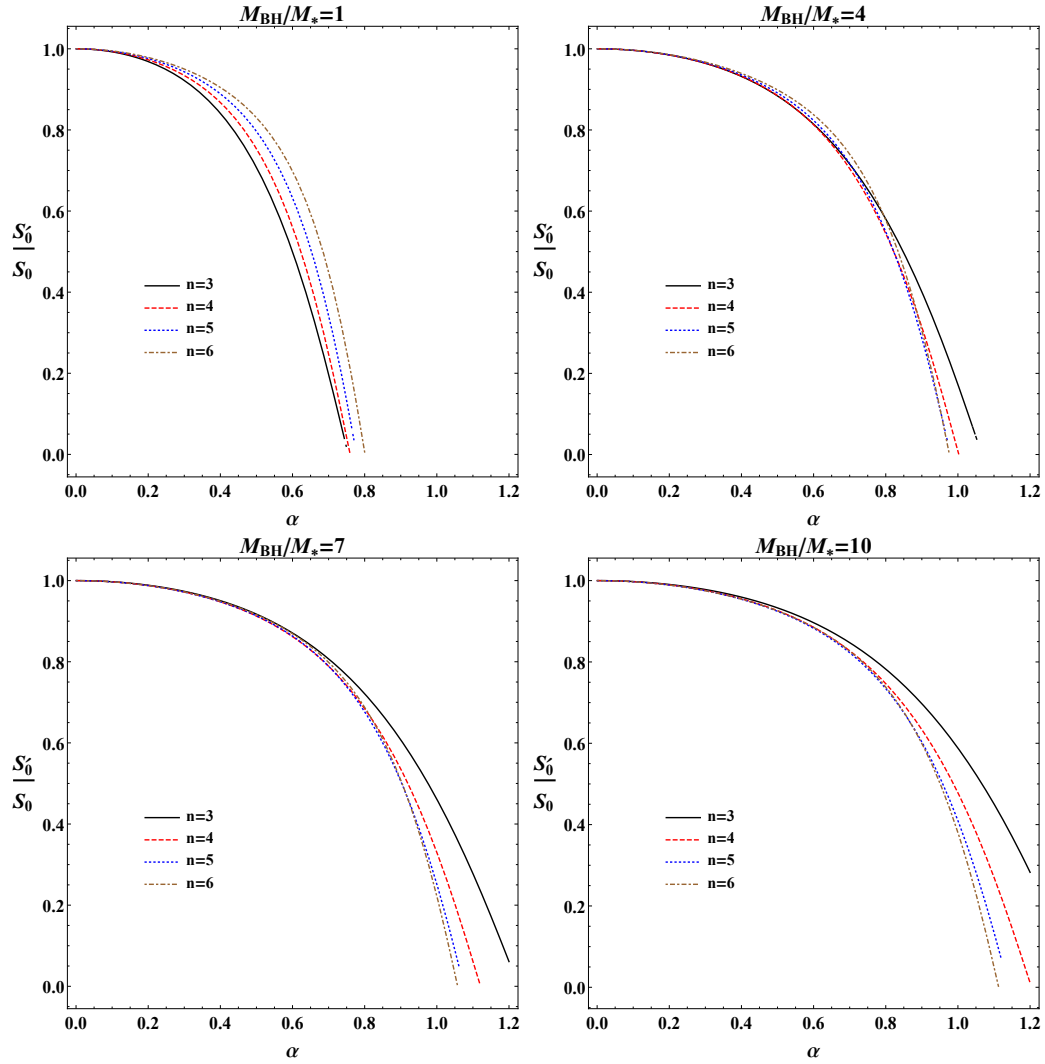


Fig. 7.3. The Ratio S'_0/S_0 as a function of n at different M_{BH}/M_* .

vanishes at $\alpha \approx 0.8 - 1.0$ for lighter BHs (upper graphs in Fig. (7.3)), and for heavier ones, S'_0 approaches zero at $\alpha \gtrsim 1.05$ (lower graphs in Fig.(7.3)), no matter what n is. Therefore, the total decay multiplicity will decrease significantly. Since there are fewer particles emitted from the BH, the average energy of the produced quanta will be higher.

The GUP also leads to the termination of the Hawking radiation when the BH mass is M_u .

7.2 GUP and CATFISH

CATFISH already incorporates GUP effects. The existence of the minimal length scale requires that the BH mass be greater than M_{ml} , and M_* too. The BH formation parameter \mathbf{XMIN} has a slightly different meaning from the one introduced in Section 6.1, where α was assumed to be zero, and $\mathbf{XMIN} = M_{\text{min}}/M_*$. If the GUP effect is turned on, \mathbf{XMIN} is given by the following relation,

$$\mathbf{XMIN} = \frac{M_{\text{min}}}{M_u}. \quad (7.11)$$

According to Eq.(7.3), $M_u = M_{\text{ml}}$ when the following condition is satisfied,

$$\alpha > \alpha_c = \frac{1}{\sqrt{\pi}} \left[\frac{8\Gamma(\frac{n+3}{2})}{n+2} \right]^{\frac{1}{n+1}}. \quad (7.12)$$

When $\alpha \leq \alpha_c$, \mathbf{XMIN} is still given by M_{min}/M_* . Table (7.1) lists the values of α_c as a function of n . The simulation of the Hawking phase will be modified according

n	3	4	5	6
α_c	0.755	0.760	0.778	0.801

Table 7.1. α_c vs n .

to the discussion in the previous section.

In this section and the next one, some results obtained from the simulation of BH events with GUP effects included will be presented. The upper bound on α below which a BH can be produced will be discussed in the next subsection. Then the lower limits on M_* and M_{min} can also be obtained using the experimental limits on BH production cross sections in Ref.[4]. These limits will be presented in the next section.

7.2.1 Simulating GUP Effects

Figs. (7.1), (7.2) and (7.3) show that the deviations of M_{ml}, T'_H and S'_0 from M_*, T_H and S_0 are very small initially, but increase faster and faster when α becomes large. Simulations with GUP effects at certain α 's confirms this prediction as shown below.

Eq.(4.57) is used to calculate the production cross section. Because of the GUP, $M_{\text{min}} = \text{XMIN} \times M_u$, so the cross section depends on α and now is called $\sigma(s, n, \text{XMIN}, \alpha)$. In fact, if $\alpha \leq \alpha_c$, $M_u = M_*$, so the cross section will not be modified, i.e.,

$$\sigma(s, n, \text{XMIN}, \alpha \leq \alpha_c) = \sigma(s, n, \text{XMIN}). \quad (7.13)$$

The expression for $\sigma(s, n, \text{XMIN})$ is given by Eq.(6.1). If $\alpha > \alpha_c$, $\sigma(s, n, \text{XMIN}, \alpha)$ is given by the following relation,

$$\sigma(s, n, \text{XMIN}, \alpha > \alpha_c) = \sigma\left(s, n, \text{XMIN} \frac{M_{\text{ml}}}{M_*}\right). \quad (7.14)$$

The production cross section as a function of M_{BH} can be obtained by running CATFISH at $n = 4$ and $\text{XMIN} = \text{QMIN} = 1$, for example. Graviton energy loss is again switched off. Fig. (7.4) shows the differential cross section $\frac{d\sigma}{dM_{\text{BH}}}$ and the total cross section σ as functions of M_{BH} at various M_* 's and α 's. In this figure, curves for $\alpha = 0.2$ and $\alpha = 0.8$ share some segments, i.e., curves for $\alpha = 0.2$ contain those for $\alpha = 0.8$, which confirms the above relation (Eq.(7.14)). A comparison with Fig.(6.1) also confirms Eq.(7.13). Therefore, if $\alpha > \alpha_c$, the cross section becomes smaller.

Table (7.2) shows other properties: modified Hawking temperature T'_H , lifetime τ , multiplicity N , modified initial entropy S'_0 , and the total cross sections σ at $\text{XMIN} = \text{QMIN} = 1$, $\text{GRAVITONLOSS} = 0$. NP does not affect the results. As shown in this table, the modified Hawking temperature T'_H is an increasing function of α ,

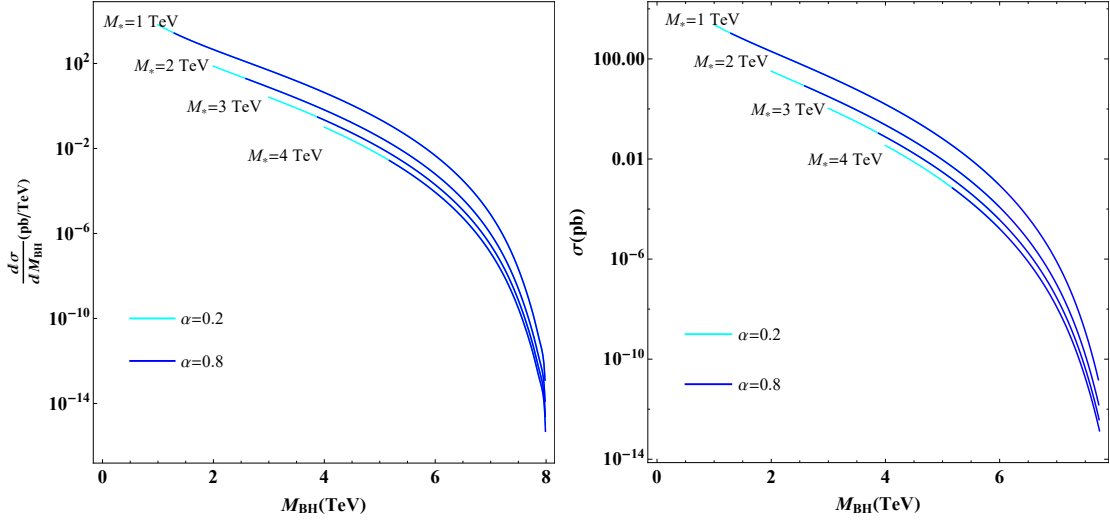


Fig. 7.4. The differential cross section $\frac{d\sigma}{dM_{\text{BH}}}$ and the total cross section σ as functions of M_{BH} . Curves for $\alpha = 0.8$ (Blue ones) overlap with those for $\alpha = 0.2$ (Cyan ones) partially.

while the lifetime τ , multiplicity N and the modified initial entropy S'_0 decrease with α . Finally, the total cross section σ stays the same initially ($\alpha \leq \alpha_c$), but drops drastically after $\alpha > \alpha_c$.

7.2.2 Upper Bounds on α

With CATFISH, it is easy to determine the maximum α which allows the formation of BHs at the center of mass energy $\sqrt{s} = 8$ TeV at the LHC. The following simple analysis shows that the maximum α_m will depend on M_* and XMIN. For a particular XMIN, M_{min} must be smaller than \sqrt{s}/XMIN . Requiring $\sqrt{s}/\text{XMIN} = M_{\text{ml}}$ gives the maximum α_m , so

$$\alpha_m = \frac{1}{\sqrt{\pi}} \left[\frac{8\Gamma(\frac{n+3}{2})}{n+2} \frac{\sqrt{s}}{M_* \times \text{XMIN}} \right]^{\frac{1}{n+1}}. \quad (7.15)$$

The maximum α_m , which will determine whether a BH can be produced at certain M_* and XMIN, can also be determined by running CATFISH. In Fig.(7.5),

M_* (TeV)	n	α	T'_H (TeV)	$\tau(\times 10^{-23}\text{s})$	N	$S'_0(k_B)$	σ (pb)	
1	4	0.2	0.214	19.8	119.03	348.14	2321.14	
		0.7	0.221	16.3	112.56	329.21	2321.14	
		0.8	0.224	15.1	110.04	321.84	1056.25	
		0.9	0.227	13.9	106.9	312.67	93.88	
		1	0.231	12.5	103	301.24	1.77	
	6	0.2	0.368	3.87	68.8	212.61	2506.7	
		0.7	0.388	2.92	63.77	197.06	2506.7	
		0.8	0.395	2.62	61.74	190.79	2506.7	
		0.9	0.405	2.29	59.1	182.63	109.57	
		1	0.417	1.93	55.57	171.74	0.15	
2	4	0.2	0.492	3.73	51.74	151.32	32.3	
		0.7	0.515	2.86	47.85	139.94	32.3	
		0.8	0.524	2.59	46.24	135.24	8.32	
		0.9	0.534	2.28	44.17	129.18	0.03	
	6	0.2	0.812	0.791	31.12	96.16	35.43	
		0.7	0.868	0.555	28.23	87.25	35.43	
		0.8	0.891	0.481	26.99	83.4	35.43	
		0.9	0.92	0.401	25.28	78.13	0.05	
	3	4	0.2	0.8	1.4	31.77	92.93	1.06
			0.7	0.846	1.02	28.86	84.41	1.06
0.8			0.863	0.901	27.6	80.72	0.11	
0.9			0.885	0.771	25.94	75.88	3.022×10^{-8}	
6		0.2	1.292	0.312	19.56	60.45	1.18	
		0.7	1.394	0.208	17.46	53.97	1.18	
		0.8	1.436	0.176	16.51	51.03	1.18	
		0.9	1.492	0.14	15.16	46.86	0.035	
4		4	0.2	1.131	0.702	22.48	65.75	0.03
			0.7	1.204	0.488	20.09	58.77	0.03
	0.8		1.233	0.421	19.03	55.65	6.91×10^{-4}	
	6	0.2	1.796	0.161	14.07	43.48	0.04	
		0.7	1.952	0.103	12.39	38.29	0.04	
		0.8	2.019	0.085	11.6	35.84	0.04	

Table 7.2. Basic properties of BHs simulated by CATFISH: modified Hawking temperature T'_H , lifetime τ , multiplicity N , modified entropy S'_0 and cross section σ .

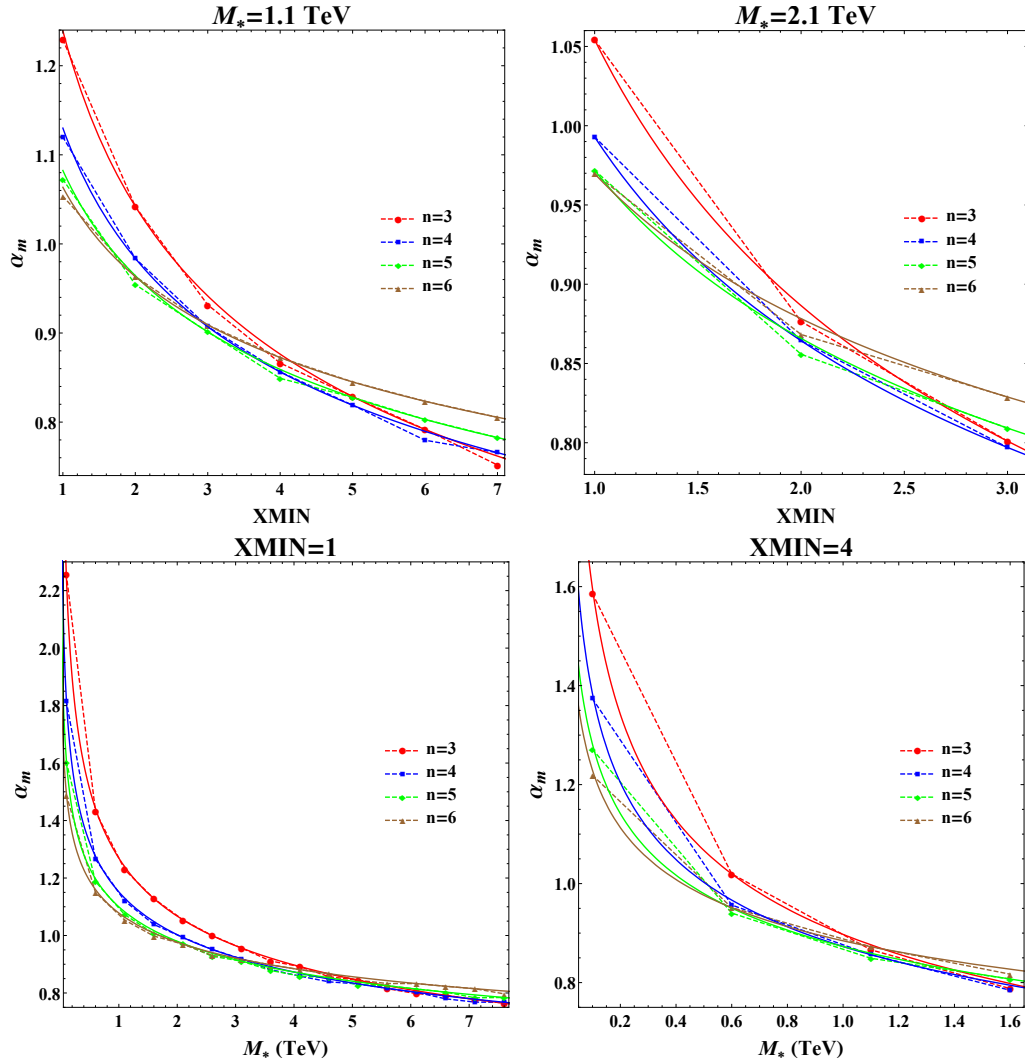


Fig. 7.5. Maximum α_m that still allows BHs to form at $\sqrt{s} = 8$ TeV at the LHC. Marked points represent results from simulation, and are linked by dashed lines. The solid curves are predicted α_m 's according to Eq.(7.15).

the top two graphs show that α_m varies as a function of X_{MIN} at different n 's. For the top left graph, $M_* = 1.1$ TeV, and for the top right graph, $M_* = 2.1$ TeV. The bottom two graphs show α_m v.s. M_* at different n 's. For the bottom left graph, $X_{MIN}=1$, while for the bottom right one, $X_{MIN}=4$. Each graph show the simulated α_m (dots) and predicted α_m by Eq.(7.15) (smooth curves) for different n 's.

7.3 Lower Bounds on M_* and M_{\min} from the GUP

In this section, the lower bounds on M_* and M_{\min} (or **XMIN**) from the GUP will be presented. These limits were obtained using the same method discussed in Chapter 6. As shown there, those bounds depend only weakly on n and NP ($\neq 0$), so in this section, lower bounds on M_* and **XMIN** are presented only for $n = 4, 6$ and $\text{NP} = 0, 4$. α is chosen to be 0.2 and 0.7, in which case $M_{\min} < M_*$. Higher values of α are also used in order to see the effect of a highly suppressed cross section on the lower bounds. These values of α are $\alpha = 0.9, 1.0$ for $n = 4$, and $\alpha = 1.0, 1.2$ for $n = 6$. CATFISH is asked to output parton level events, which are fed into PYTHIA (v8.2.12) to hadronize. The PDF CTEQ6L1 is used for this analysis.

7.3.1 Delphes: A Fast Detector Simulator

The charged particles emitted from the BH travel in a magnetic field of strength 3.8 T, so when they reach the detector, their velocities will change because of the Lorentz force applied by the magnetic field. In addition, the detector is not 100% efficient, so some particles might be misidentified or their energies may not be measured accurately. Finally, the design of the detector includes “blind spots”, which should be taken care specifically. All of these requires to perform detector simulations.

In this analysis, Delphes [91] is used to simulate the detector response. It is a C++ framework and a simplified approach based on the parametrization of the detector response, including the tracking system, embedding into a magnetic field, calorimeters and a muon system. The framework is interfaced to standard file formats, e.g., Les Houches Event File or HepMC, and outputs observables such as isolated leptons, missing transverse energy and collections of jets which can be used for dedicated analyses. The simulation of the detector response takes into

account the effect of the magnetic field, the granularity of the calorimeters and sub-detector resolutions. The present version of Delphes roughly emulates the particle-flow (PF) reconstruction philosophy used in CMS [92]. FastJet algorithm [93] provides fast native implementations of different jet-finding algorithms, especially, including the anti- k_T algorithm used in this analysis.

7.3.2 The S_T Spectra

Delphes is employed for this analysis, and its kinematic cuts are given in Table (7.3) below. These requirements parallel mostly those listed in Section 6.2.1.1 as

Objects	p_T	$ \eta $	Iso(ι)
Jets	> 50 GeV	< 2.6	N/A
Muons		< 2.1	Iso(0.3) $< 20\%$
Electrons		(1.56, 2.4) &	
Photons		(0, 1.44)	†

Table 7.3. Kinematic cuts employed to obtain the S_T spectra. †: The scalar sums of transverse energy (momenta in the case of the tracker) calculated in a cone of $\Delta R = 0.4$ around the candidate photon direction should not be greater than 2.0, 4.2, and 2.2 GeV for the tracker, ECAL, and HCAL, respectively.

used by the CMS Collaboration in Ref.[4].

Choosing $M_* = 1$ TeV, and $n = 4$, the S_T spectra can be obtained for different NP's and α 's, as shown in Fig.'s (7.6, 7.7). Comparison can be made with Fig.'s (6.7, 6.8) which are the S_T spectra for $\alpha = 0$. As expected, at $\alpha = 0.7$, the GUP does not affect the S_T spectra a lot. However, when $\alpha = 0.9$ (represented by the yellow curve), the spectrum is highly suppressed, as compared to the blue one, because the cross section is much smaller.

7.3.3 Lower Bounds on M_* and M_{\min} for Various α 's

The lower bounds on M_* and M_{\min} with the GUP effects turned on will be presented in this section, and the discussion will parallel the one in Section (6.2.2.2).

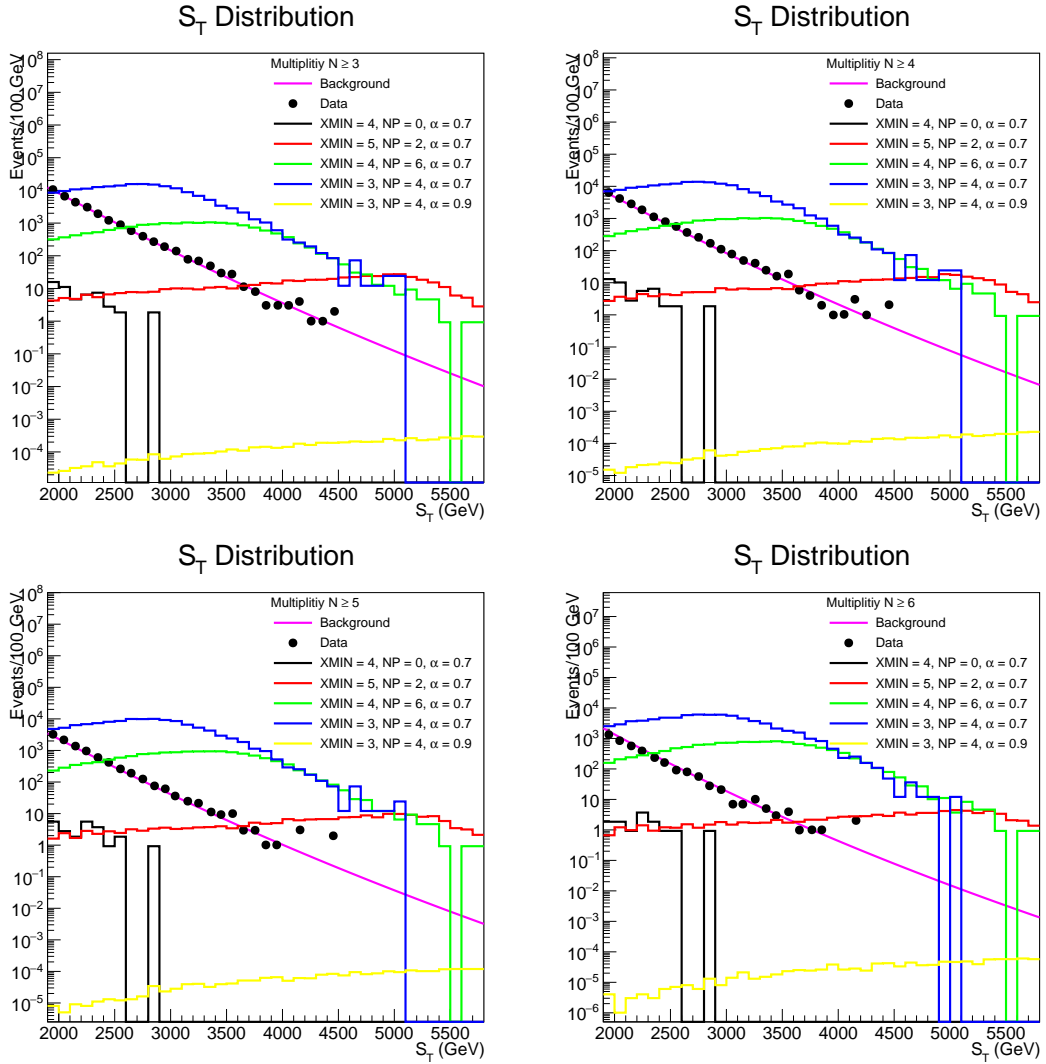


Fig. 7.6. The S_T for events with different multiplicities. Dots represent observed spectra and the green solid lines represent the predicted background distributions, which are taken from Figure 2 in Ref.[4]. The BH signals are also shown.

Having determined the S_T spectra, the distributions of partial cross section $\sigma(S_T > S_T^{\min})$ times acceptance (A) can be obtained, which are shown in Fig. (7.8). These curves were obtained by running CATFISH with $\text{NEXTRADIM} = 4$, $\text{GRAVITONLOSS} = 0$, $\text{NP} = 4$. The upper two graphs in Fig. (7.8) show $\sigma(S_T > S_T^{\min}) \times A$ as a function of M_* at $\text{XMIN} = \text{QMIN} = 3$ and $\alpha = 0.7$ (the left graph)

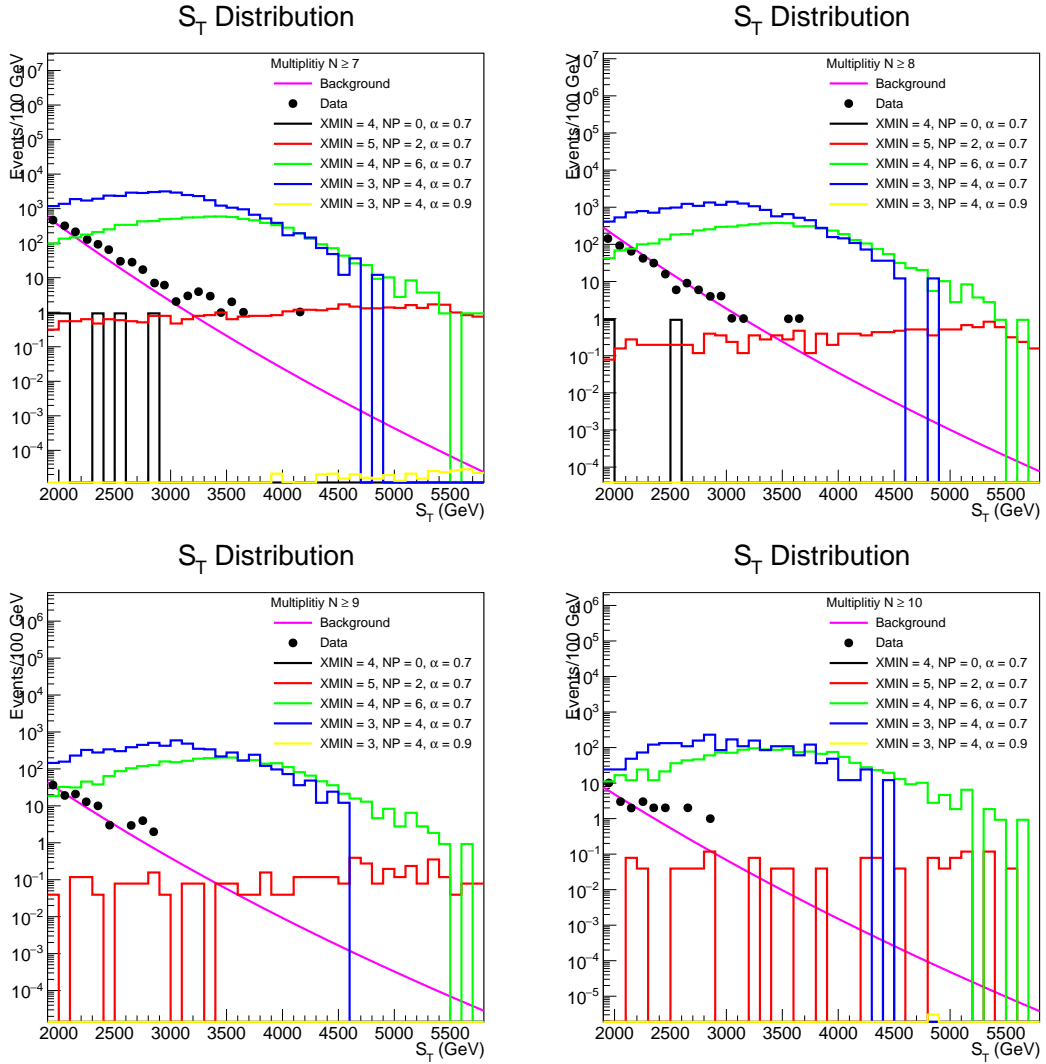


Fig. 7.7. The S_T for events with different multiplicities. Dots represent observed spectra and the green solid lines represent the predicted background distributions, which are taken from Figure 2 in Ref.[4]. The BH signals are also shown.

and 0.9 (the right graph). The lower two graphs show $\sigma(S_T > S_T^{\min}) \times A$ as a function of XMIN at $M_* = 1.51$ TeV and $\alpha = 0.7$ (the left graph) and 0.9 (the right graph). These results confirm that $\sigma(S_T > S_T^{\min}) \times A$ is a decreasing function of M_* and XMIN as discussed in Section (6.2.2.2).

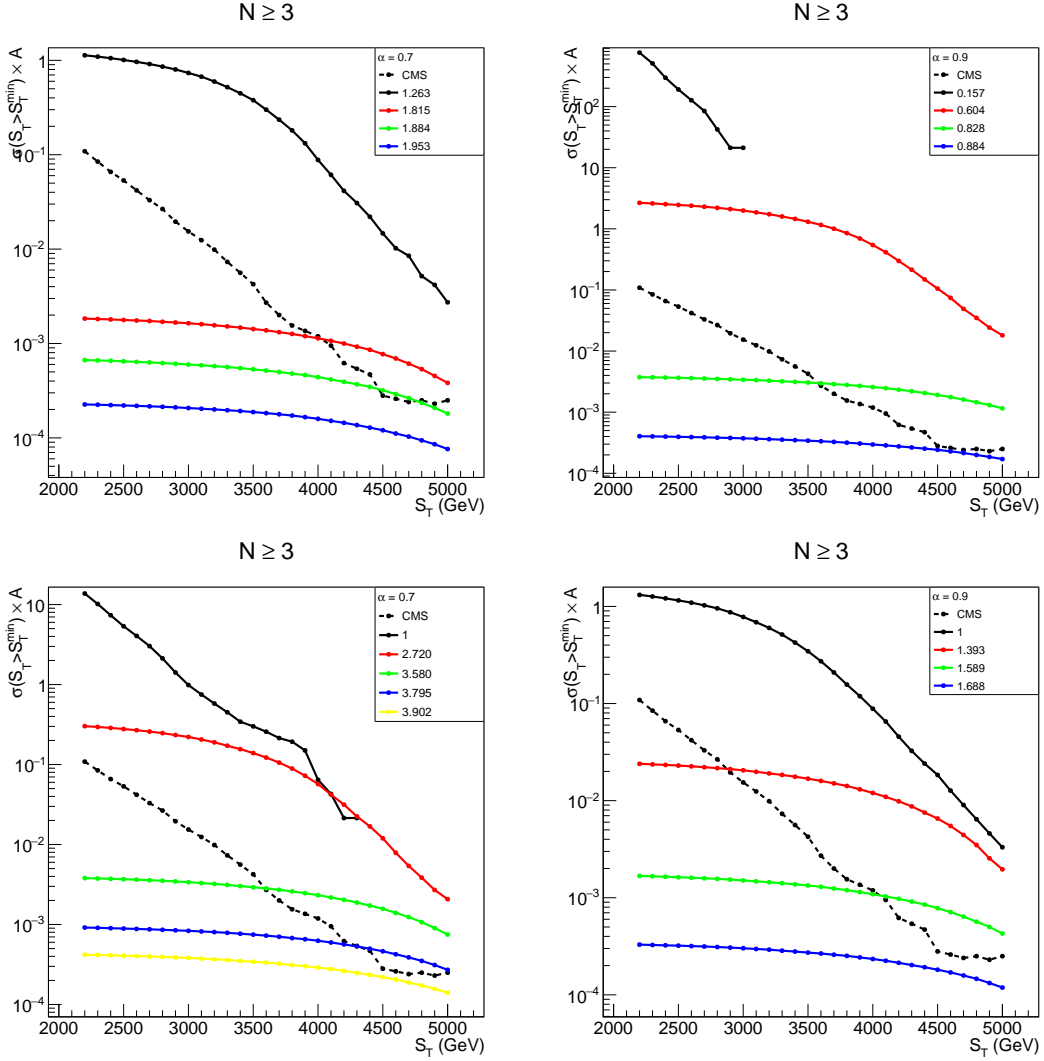


Fig. 7.8. $\sigma(S_T > S_T^{\min}) \times A$ as a function of M_* (Upper two graphs, numbers being M_* 's chosen in units of TeV) or X_{MIN} (Lower two graphs, numbers being X_{MIN} 's) at $\alpha = 0.7$ (Left two graphs) and $\alpha = 0.9$ (Right two graphs). The model-independent 95% CL experimental upper limits for counting experiments from CMS Collaboration are also shown. The multiplicity is $N \geq 3$.

The bisection method has been applied to determine the lower bounds on M_* and X_{MIN} . Fig. (7.9) shows the lower bounds on M_* as a function of X_{MIN} , NP and α for 4 (the left graph) and 6 (the right graph) extra dimensions. In these graphs, the dashed curves are for NP = 0 and the solid ones are for NP = 4. The curves

for $\alpha = 0$ represent the limits with GUP effects switched off, and as $\alpha \leq 0.7$, the limits stay almost the same as these at $\alpha = 0$, but when $\alpha \geq 0.9$, the limits become smaller. Similarly, Fig. (7.10) shows the lower bounds on XMIN as a function of

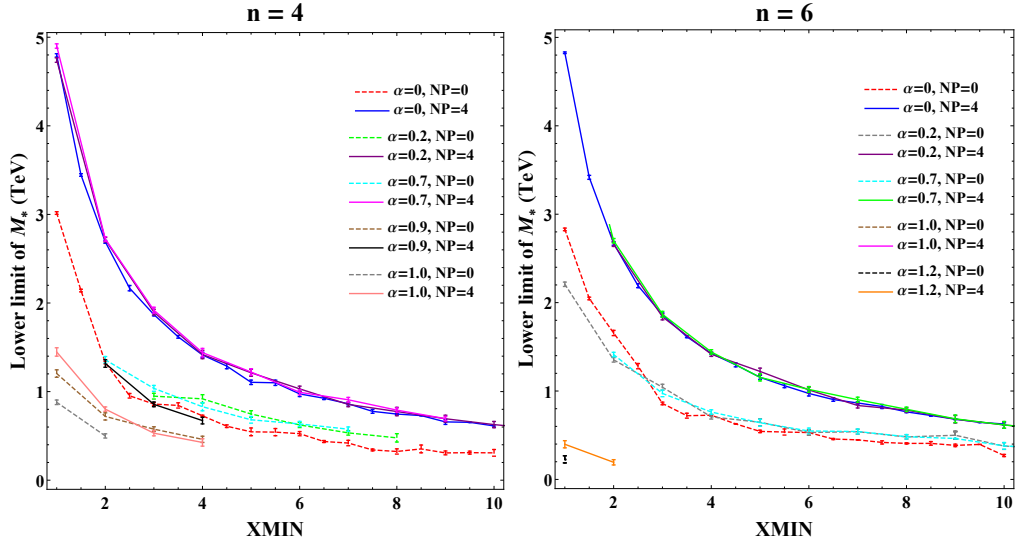


Fig. 7.9. Simulated lower limit on M_* vs. XMIN as a function of α , NP and NEXTRADIM = 4(left), and 6 (right). The limits first discussed in Section (6.2.2.2) are also shown ($\alpha = 0$).

M_* , NP and α for 4 (the left graph) and 6 (the right graph) extra dimensions. The curves at $\alpha = 0$ again represent the limits with GUP effects switched off, and as $\alpha \leq 0.7$, the limits stay almost the same as these at $\alpha = 0$, but when $\alpha \geq 0.9$, the limits become smaller.

Although the lower bounds on XMIN decrease as long as $\alpha \geq 0.9$, the lower bounds on M_{\min} at NP = 4 stay almost the same for different α 's, as shown in Fig. (7.11). Although when NP = 0, there are some variations in the M_{\min} limit, these variations can be explained by the smaller statistics as there are fewer energetic particles produced when NP = 0. The next two figures (7.12, 7.13) compare the lower bounds on M_{\min} predicted by CATFISH with those from BlackMax and CHARYBDIS2 done by the CMS Collaboration [4] and the ATLAS Collaboration

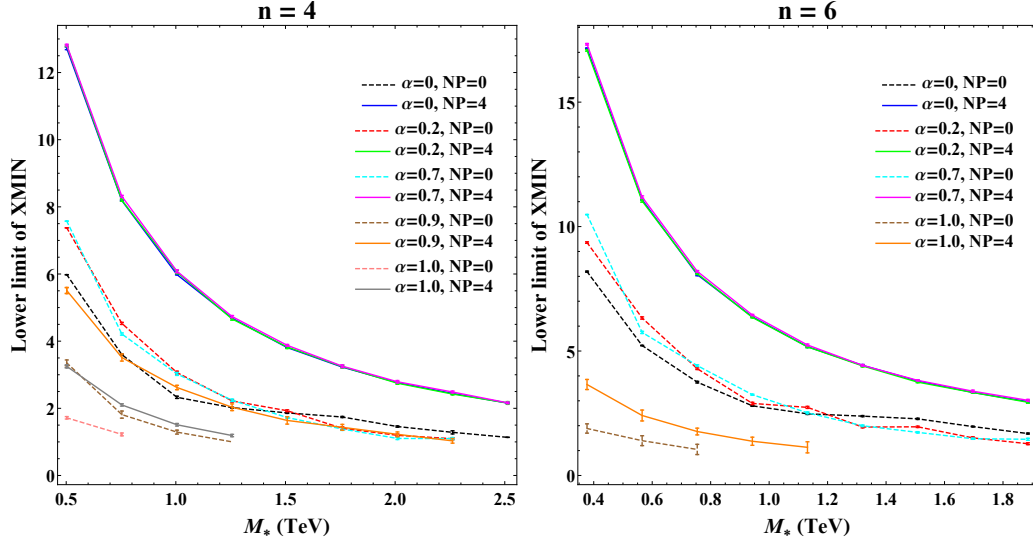


Fig. 7.10. Simulated lower limit on X_{MIN} vs. M_* as a function of α , NP and NEXTRADIM = 4(right), and 6 (left). The limits first discussed in Section (6.2.2.2) are also shown ($\alpha = 0$).

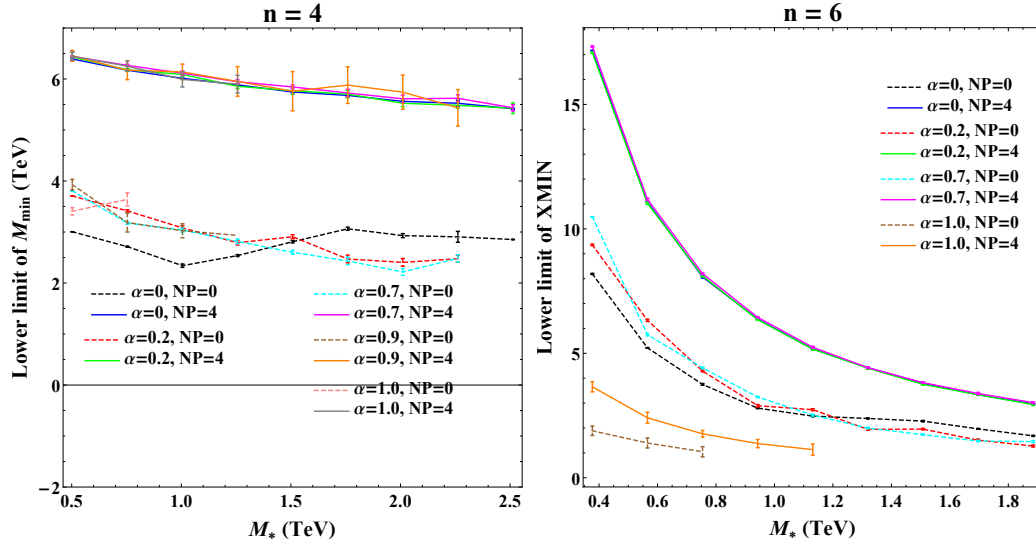


Fig. 7.11. Simulated lower limit on M_{min} vs. M_* as a function of α , NP and NEXTRADIM = 4(right), and 6 (left).

[5], respectively. Since the M_{min} limits are weakly dependent on α , the conclusion will be the same as discussed in the last two paragraphs in Section (6.2.2.2).

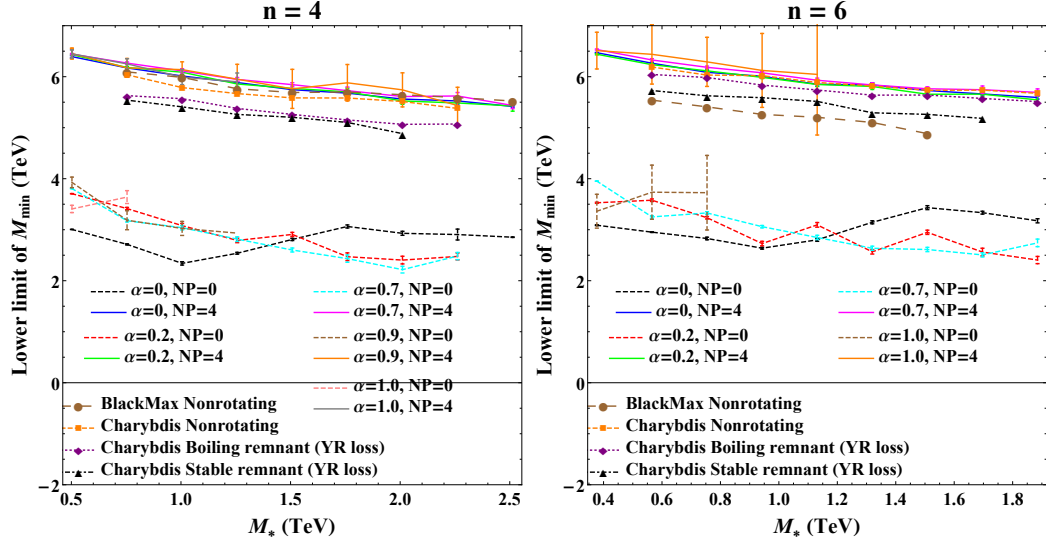


Fig. 7.12. Comparison of the predictions on lower limits of M_{\min} from CATFISH with those from BlackMax and CHARYBDIS2 at NEXTRADIM = 4 (left) and 6 (right). The results of BlackMax and CHARBDIS are extracted from Fig. 4 in Ref.[4].

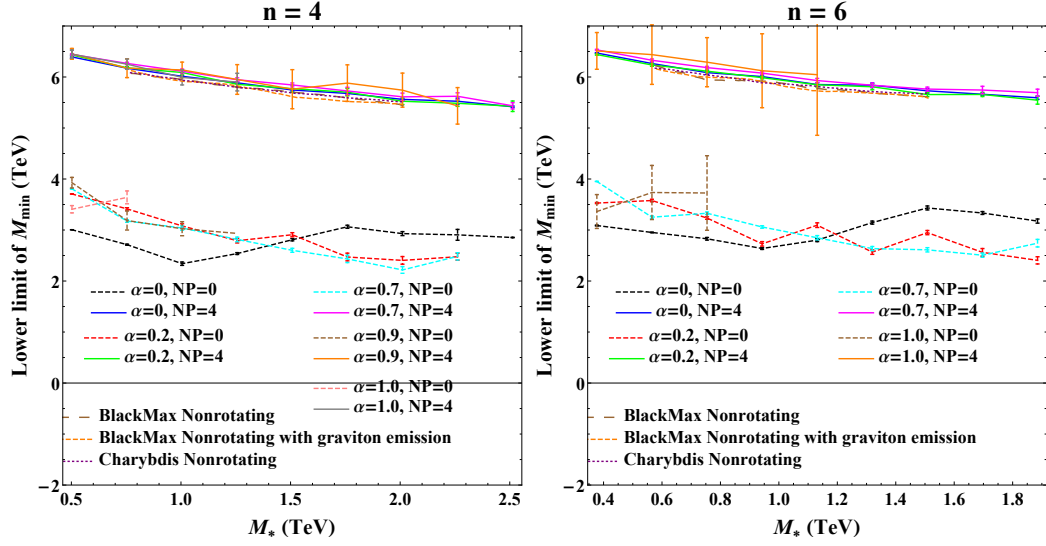


Fig. 7.13. Comparison of the predictions on lower limits of M_{\min} from CATFISH with those from BlackMax and CHARYBDIS2 at NEXTRADIM = 4 (left) and 6 (right). The results of BlackMax and CHARBDIS are extracted from Fig.'s 8 and 10 in Ref.[5].

8 Conclusion

In this work, lower limits on the fundamental Planck scale M_* and minimal BH mass M_{\min} at formation have been obtained in a vast parameter space, using experimental upper limits on the partial production cross section of microscopic BHs [4]. Various models implemented in CATFISH have been explored and different limits have been determined. These models include some combinations of physics, such as BD model, stable BH remnant or complete decay model, and GUP effects.

The results on M_* limits show that, in general, models with BH remnant give milder constraints than complete decay models. The lower limits on M_* depend on α : when $0 \leq \alpha \leq 0.7$, the limits barely vary with α ; but when $\alpha \geq 0.9$, the limits decrease quickly. These limits certainly solve the hierarchy problem, since they are less than ~ 5 TeV. In addition, they also constrain the size R of LEDs in ADD models, i.e., $R \lesssim 1.10$ nm.

The results on M_{\min} show that the lower limits for models without a BH stable remnant generally agree with earlier results by the CMS collaboration and the ATLAS collaboration based on the BlackMax and CHARYBDIS generators, and again, BH remnant models give milder constraints than complete decay models. These limits exclude the formation of more massive microscopic BH's.

REFERENCES

- [1] U. of Alabama, “Research computing,” <https://researchcomputing.ua.edu/> (2010), used since 2011.
- [2] “Alabama supercomputer center (asc),” (1989).
- [3] P. Kanti, Int. J. Mod. Phys. **A19**, 4899 (2004), arXiv:hep-ph/0402168 [hep-ph] .
- [4] S. Chatrchyan *et al.* (CMS), JHEP **07**, 178 (2013), arXiv:1303.5338 [hep-ex] .
- [5] G. Aad *et al.* (ATLAS), JHEP **08**, 103 (2014), arXiv:1405.4254 [hep-ex] .
- [6] E. A. Mirabelli, M. Perelstein, and M. E. Peskin, Phys. Rev. Lett. **82**, 2236 (1999), arXiv:hep-ph/9811337 [hep-ph] .
- [7] N. Arkani-Hamed, S. Dimopoulos, and G. R. Dvali, Phys. Lett. **B429**, 263 (1998), arXiv:hep-ph/9803315 [hep-ph] .
- [8] I. Antoniadis, N. Arkani-Hamed, S. Dimopoulos, and G. R. Dvali, Phys. Lett. **B436**, 257 (1998), arXiv:hep-ph/9804398 [hep-ph] .
- [9] N. Arkani-Hamed, S. Dimopoulos, and G. R. Dvali, Phys. Rev. **D59**, 086004 (1999), arXiv:hep-ph/9807344 [hep-ph] .
- [10] V. Khachatryan *et al.* (CMS), Phys. Lett. **B697**, 434 (2011), arXiv:1012.3375 [hep-ex] .

- [11] S. Chatrchyan *et al.* (CMS), JHEP **01**, 013 (2013), arXiv:1210.2387 [hep-ex]
.
- [12] S. Chatrchyan *et al.* (CMS), JHEP **04**, 061 (2012), arXiv:1202.6396 [hep-ex]
.
- [13] V. Khachatryan *et al.* (CMS), Phys. Rev. **D91**, 052009 (2015),
arXiv:1501.04198 [hep-ex] .
- [14] *Search for Microscopic Black Holes in Multi-Jet Final States with the ATLAS
Detector at $\sqrt{s} = 7$ TeV*, Tech. Rep. ATLAS-CONF-2011-068 (CERN,
Geneva, 2011).
- [15] G. Aad *et al.* (ATLAS), Phys. Rev. **D88**, 072001 (2013), arXiv:1308.4075
[hep-ex] .
- [16] A. Einstein, Sitzungsberichte der Königlich Preußischen Akademie der Wis-
senschaften (Berlin), Seite 844-847. (1915).
- [17] R. M. Wald, *General Relativity* (The University of Chicago Press, 1984) pp.
1–491.
- [18] S. M. Carroll, *Spacetime and geometry: An introduction to general relativity*
(San Francisco, USA: Addison-Wesley (2004) 513 p, 2004).
- [19] S. Chatrchyan *et al.* (CMS), Phys. Lett. **B716**, 30 (2012), arXiv:1207.7235
[hep-ex] .
- [20] G. Aad *et al.* (ATLAS), Phys. Lett. **B716**, 1 (2012), arXiv:1207.7214 [hep-ex]
.
- [21] M. Ajello *et al.* (Fermi-LAT), JCAP **1202**, 012 (2012), arXiv:1201.2460
[astro-ph.HE] .

- [22] C. Hanhart, J. A. Pons, D. R. Phillips, and S. Reddy, *Physics Letters B* **509**, 1 (2001).
- [23] S. Hannestad and G. Raffelt, *Phys. Rev. Lett.* **87**, 051301 (2001), arXiv:hep-ph/0103201 [hep-ph] .
- [24] V. Khachatryan *et al.* (CMS), *Phys. Rev.* **D90**, 032005 (2014), arXiv:1405.7653 [hep-ex] .
- [25] G. Aad *et al.* (ATLAS), *JHEP* **07**, 032 (2015), arXiv:1503.08988 [hep-ex] .
- [26] M. Shifman, *Crossing the boundaries: Gauge dynamics at strong coupling. Proceedings, Workshop in Honor of the 60th Birthday of Misha Shifman, Minneapolis, USA, May 14-17, 2009*, *Int. J. Mod. Phys.* **A25**, 199 (2010), arXiv:0907.3074 [hep-ph] .
- [27] M. Cavaglià, *Int. J. Mod. Phys.* **A18**, 1843 (2003), arXiv:hep-ph/0210296 [hep-ph] .
- [28] G. F. Giudice, R. Rattazzi, and J. D. Wells, *Nucl. Phys.* **B544**, 3 (1999), arXiv:hep-ph/9811291 [hep-ph] .
- [29] A. Collaboration (ATLAS Collaboration), *Search for New Phenomena in Monojet plus Missing Transverse Momentum Final States using 10 fb^{-1} of pp Collisions at $\sqrt{s}=8 \text{ TeV}$ with the ATLAS detector at the LHC*, Tech. Rep. (CERN, 2012)ATLAS-CONF-2012-147 .
- [30] C. Collaboration (CMS Collaboration), *Search for new physics in monojet events in pp collisions at $\sqrt{s}= 8 \text{ TeV}$* , Tech. Rep. CMS-PAS-EXO-12-048 (CERN, Geneva, 2013).

- [31] C. Collaboration (CMS), *Search for Large Extra Spatial Dimensions in Dielectron Production with the CMS Detector*, Tech. Rep. (CERN, 2013)CMS-PAS-EXO-12-031 .
- [32] C. Collaboration (CMS Collaboration), *Search for Extra Dimensions in Dimuon Events in pp Collisions at $\sqrt{s} = 8$ TeV*, Tech. Rep. CMS-PAS-EXO-12-027 (CERN, Geneva, 2013).
- [33] V. Khachatryan *et al.* (CMS), Phys. Lett. **B746**, 79 (2015), arXiv:1411.2646 [hep-ex] .
- [34] V. Khachatryan *et al.* (CMS), JHEP **04**, 025 (2015), arXiv:1412.6302 [hep-ex] .
- [35] V. Khachatryan *et al.* (CMS), Eur. Phys. J. **C75**, 235 (2015), arXiv:1408.3583 [hep-ex] .
- [36] G. Aad *et al.* (ATLAS), Eur. Phys. J. **C75**, 299 (2015), [Erratum: Eur. Phys. J. C75,no.9,408(2015)], arXiv:1502.01518 [hep-ex] .
- [37] G. Aad *et al.* (ATLAS), Eur. Phys. J. **C74**, 3134 (2014), arXiv:1407.2410 [hep-ex] .
- [38] C. Collaboration (CMS Collaboration), *Z' to tau tau - emu final state*, Tech. Rep. CMS-PAS-EXO-12-046 (CERN, Geneva, 2015).
- [39] C. Collaboration (CMS Collaboration), *Monophoton search*, Tech. Rep. CMS-PAS-EXO-12-047 (CERN, Geneva, 2014).
- [40] G. Aad *et al.* (ATLAS), Phys. Rev. **D91**, 012008 (2015), [Erratum: Phys. Rev.D92,no.5,059903(2015)], arXiv:1411.1559 [hep-ex] .
- [41] T. Gleisberg, F. Krauss, K. T. Matchev, A. Schaliche, S. Schumann, and G. Soff, JHEP **09**, 001 (2003), arXiv:hep-ph/0306182 [hep-ph] .

- [42] M. Nagano and A. A. Watson, *Rev. Mod. Phys.* **72**, 689 (2000).
- [43] J. L. Feng and A. D. Shapere, *Phys. Rev. Lett.* **88**, 021303 (2002), arXiv:hep-ph/0109106 [hep-ph] .
- [44] D. Kazanas and A. Nicolaidis, *General Relativity and Gravitation* **35**, 1117 (2003).
- [45] L. Anchordoqui and H. Goldberg, *Phys. Rev.* **D65**, 047502 (2002), arXiv:hep-ph/0109242 [hep-ph] .
- [46] Y. Uehara, *Prog. Theor. Phys.* **107**, 621 (2002), arXiv:hep-ph/0110382 [hep-ph] .
- [47] M. Kowalski, A. Ringwald, and H. Tu, *Physics Letters B* **529**, 1 (2002).
- [48] J. Alvarez-Muniz, J. L. Feng, F. Halzen, T. Han, and D. Hooper, *Phys. Rev.* **D65**, 124015 (2002), arXiv:hep-ph/0202081 [hep-ph] .
- [49] L. A. Anchordoqui, J. L. Feng, H. Goldberg, and A. D. Shapere, *Phys. Rev.* **D65**, 124027 (2002), arXiv:hep-ph/0112247 [hep-ph] .
- [50] A. collaboration, *Search for evidence for strong gravity in jet final states produced in pp collisions at $\sqrt{s} = 13$ TeV using the ATLAS detector at the LHC*, Tech. Rep. (CERN, 2015)ATLAS-CONF-2015-043 .
- [51] K. Schwarzschild, *Sitzungsberichte der Königlich Preußischen Akademie der Wissenschaften (Berlin)*, 1916, Seite 189-196 (1916).
- [52] R. C. Myers and M. J. Perry, *Annals of Physics* **172**, 304 (1986).
- [53] J. M. Bardeen, B. Carter, and S. W. Hawking, *Comm. Math. Phys.* **31**, 161 (1973).

- [54] B. Carter, “General relativity: An einstein centenary survey,” (Cambridge University Press, Cambridge, U.K.; New York, U.S.A., 1979) Chap. 6., pp. 294–369.
- [55] S. W. Hawking, Phys. Rev. Lett. **26**, 1344 (1971).
- [56] K. S. Thorne, *Magic Without Magic: John Archibald Wheeler*, edited by J. Klauder (Freeman, San Francisco, 1972).
- [57] P. C. Aichelburg and R. U. Sexl, General Relativity and Gravitation **2**, 303 (1971).
- [58] D. M. Eardley and S. B. Giddings, Phys. Rev. **D66**, 044011 (2002), arXiv:gr-qc/0201034 [gr-qc] .
- [59] H. Yoshino and Y. Nambu, Phys. Rev. **D66**, 065004 (2002), arXiv:gr-qc/0204060 [gr-qc] .
- [60] H. Yoshino and Y. Nambu, Phys. Rev. **D67**, 024009 (2003), arXiv:gr-qc/0209003 [gr-qc] .
- [61] H. Yoshino and V. S. Rychkov, Phys. Rev. **D71**, 104028 (2005), [Erratum: Phys. Rev.D77,089905(2008)], arXiv:hep-th/0503171 [hep-th] .
- [62] V. Cardoso, O. J. C. Dias, and J. P. S. Lemos, Phys. Rev. **D67**, 064026 (2003), arXiv:hep-th/0212168 [hep-th] .
- [63] V. Cardoso, E. Berti, and M. Cavaglià, Class. Quant. Grav. **22**, L61 (2005), arXiv:hep-ph/0505125 [hep-ph] .
- [64] M. Cavaglià, R. Godang, L. Cremaldi, and D. Summers, Comput. Phys. Commun. **177**, 506 (2007), arXiv:hep-ph/0609001 [hep-ph] .

- [65] D. M. Gingrich and K. Martell, Phys. Rev. **D78**, 115009 (2008), arXiv:0808.2512 [hep-ph] .
- [66] S. B. Giddings and S. D. Thomas, Phys. Rev. **D65**, 056010 (2002), arXiv:hep-ph/0106219 [hep-ph] .
- [67] G. L. Landsberg, J. Phys. **G32**, R337 (2006), arXiv:hep-ph/0607297 [hep-ph] .
- [68] W. G. Unruh, Phys. Rev. **D14**, 870 (1976).
- [69] S. W. Hawking, Comm. Math. Phys. **43**, 199 (1975).
- [70] C. M. Harris and P. Kanti, JHEP **10**, 014 (2003), arXiv:hep-ph/0309054 [hep-ph] .
- [71] S. Creek, O. Efthimiou, P. Kanti, and K. Tamvakis, Phys. Lett. **B635**, 39 (2006), arXiv:hep-th/0601126 [hep-th] .
- [72] A. S. Cornell, W. Naylor, and M. Sasaki, JHEP **02**, 012 (2006), arXiv:hep-th/0510009 [hep-th] .
- [73] V. Cardoso, M. Cavaglià, and L. Gualtieri, Phys. Rev. Lett. **96**, 071301 (2006), [Erratum: Phys. Rev. Lett.96,219902(2006)], arXiv:hep-th/0512002 [hep-th] .
- [74] V. Cardoso, M. Cavaglià, and L. Gualtieri, JHEP **02**, 021 (2006), arXiv:hep-th/0512116 [hep-th] .
- [75] D. K. Park, Phys. Lett. **B638**, 246 (2006), arXiv:hep-th/0603224 [hep-th] .
- [76] T. Sjostrand, S. Mrenna, and P. Z. Skands, JHEP **05**, 026 (2006), arXiv:hep-ph/0603175 [hep-ph] .

- [77] E. Boos *et al.*, in *Physics at TeV colliders. Proceedings, Euro Summer School, Les Houches, France, May 21-June 1, 2001* (2001) arXiv:hep-ph/0109068 [hep-ph] .
- [78] M. Cavaglià, *Physics Letters B* **569**, 7 (2003).
- [79] S. Dimopoulos and G. L. Landsberg, *proceedings of APS / DPF / DPB Summer Study on the Future of Particle Physics (Snowmass 2001), Snowmass, Colorado, 30 Jun - 21 Jul 2001*, eConf **C010630**, P321 (2001), [,252(2001)].
- [80] C. M. Harris, P. Richardson, and B. R. Webber, *JHEP* **08**, 033 (2003), arXiv:hep-ph/0307305 [hep-ph] .
- [81] J. A. Frost, J. R. Gaunt, M. O. P. Sampaio, M. Casals, S. R. Dolan, M. A. Parker, and B. R. Webber, *JHEP* **10**, 014 (2009), arXiv:0904.0979 [hep-ph] .
- [82] D.-C. Dai, G. Starkman, D. Stojkovic, C. Issever, E. Rizvi, and J. Tseng, *Phys. Rev.* **D77**, 076007 (2008), arXiv:0711.3012 [hep-ph] .
- [83] D.-C. Dai, C. Issever, E. Rizvi, G. Starkman, D. Stojkovic, and J. Tseng, (2009), arXiv:0902.3577 [hep-ph] .
- [84] M. Cacciari, G. P. Salam, and G. Soyez, *JHEP* **04**, 063 (2008), arXiv:0802.1189 [hep-ph] .
- [85] J. Alwall, M. Herquet, F. Maltoni, O. Mattelaer, and T. Stelzer, *JHEP* **06**, 128 (2011), arXiv:1106.0522 [hep-ph] .
- [86] S. Agostinelli *et al.* (GEANT4), *Nucl. Instrum. Meth.* **A506**, 250 (2003).
- [87] P. M. Nadolsky, H.-L. Lai, Q.-H. Cao, J. Huston, J. Pumplin, D. Stump, W.-K. Tung, and C. P. Yuan, *Phys. Rev.* **D78**, 013004 (2008), arXiv:0802.0007 [hep-ph] .

- [88] S. Hou, B. Harms, and M. Cavaglia, JHEP **11**, 185 (2015), arXiv:1507.01632 [hep-ph] .
- [89] M. Cavaglia, S. Das, and R. Maartens, Class. Quant. Grav. **20**, L205 (2003), arXiv:hep-ph/0305223 [hep-ph] .
- [90] M. Cavaglia and S. Das, Class. Quant. Grav. **21**, 4511 (2004), arXiv:hep-th/0404050 [hep-th] .
- [91] J. de Favereau, C. Delaere, P. Demin, A. Giammanco, V. Lemaître, A. Mertens, and M. Selvaggi (DELPHES 3), JHEP **02**, 057 (2014), arXiv:1307.6346 [hep-ex] .
- [92] C. Collaboration (CMS Collaboration), *Particle-Flow Event Reconstruction in CMS and Performance for Jets, Taus, and MET*, Tech. Rep. CMS-PAS-PFT-09-001 (CERN, 2009. Geneva, 2009).
- [93] M. Cacciari, G. P. Salam, and G. Soyez, Eur. Phys. J. **C72**, 1896 (2012), arXiv:1111.6097 [hep-ph] .

A Differential Geometry

In this appendix, some concepts are defined geometrically, for a 4-dimensional spacetime. The generalization to higher dimensional spacetime is straightforward. A spacetime \mathcal{M} is a differentiable manifold which is a set covered by a collection $\{U_\alpha\}$ of subsets U_α . For each subset U_α , there exists a homeomorphism ψ_α from U_α to a subset of \mathbb{R}^4 . A compatibility condition needs to be imposed on these subsets and homeomorphisms, that is, if $U_\alpha \cap U_\beta \neq \emptyset^1$, the composition $\psi_\beta \circ \psi_\alpha^{-1} : \psi_\alpha(U_\alpha \cap U_\beta) \rightarrow \psi_\beta(U_\alpha \cap U_\beta)$ is smooth.

Since $\psi_\alpha : U_\alpha \rightarrow \mathbb{R}^4$ is one-to-one, a 4-tuple (x^0, x^1, x^2, x^3) can be assigned to each point p in U_α and this tuple is called the coordinate of the point p and abbreviated as x^μ or x . The pair (U_α, ψ_α) or (U_α, x^μ) is called a coordinate system. If p is also covered by another subset U_β , then ψ_β will map p to a new 4-tuple y^μ , which is a new coordinate of p . Since both x^μ and y^μ are associated to the same point p , the y^μ are smooth functions of x^μ , i.e., $y^\mu = y^\mu(x^\nu)$.

A.1 Invariant Objects: Tensors

As introduced in Chapter 2, there are 3 basic types of tensors, which are discussed below, together with general tensors.

Scalars

A scalar is a function $f : \mathcal{M} \rightarrow \mathbb{R}$, which assigns a real number to a point p in \mathcal{M} : $f(p) \in \mathbb{R}$. Since f is a function of spacetime points, f always maps p to a

¹The intersection of U_α and U_β is not an empty set.

²Abuse of notation: x^μ represents the 4-tuple (x^0, x^1, x^2, x^3) or the μ -th component of the coordinate based on the context.

particular real number, no matter what coordinate system is used to cover p :

$$f(p) = f(x) = f(y). \quad (\text{A.1})$$

Vectors

A vector defined at a point $p \in \mathcal{M}$ is defined to be a map $v : \mathcal{F}(\mathcal{M}) \rightarrow \mathbb{R}$, where $\mathcal{F}(\mathcal{M})$ is the set of smooth functions on \mathcal{M} . In addition, v also satisfies the linearity condition and Leibnitz rule:

$$\begin{aligned} v(\alpha f + \beta g) &= \alpha v(f) + \beta v(g), \\ v(fg) &= f v(g) + v(f)g, \end{aligned} \quad (\text{A.2})$$

for any functions f, g and real numbers α, β . v is thus called a linear map. If a coordinate system (U_α, x^μ) covers p , there is a special smooth function defined on U_α , x^μ , the action of v on f at p is defined to be

$$v(f(p)) = v^\mu \frac{\partial}{\partial x^\mu} f(p) = v^\mu \frac{\partial}{\partial x^\mu} f(x), \quad (\text{A.3})$$

in which v^μ is the μ -th coordinate component of v , and $\partial/\partial x^\mu = \partial_\mu$ is called the μ -th basic vector. This definition reflects the idea that the vector fields are directional derivatives of functions. The whole collection of vectors v forms a vector space V_p at point p and ∂_μ 's constitute the coordinate basis of V_p . v can also be simply written as

$$v = v^\mu \partial_\mu. \quad (\text{A.4})$$

Tangent Vectors to Smooth Curves

Let $C : \mathbb{R} \rightarrow \mathcal{M}$ be a smooth curve defined on \mathcal{M} parametrized by t , and $p = C(0)$. Then the tangent vector T to C at p is defined according to the following relation,

$$T(f) = \left. \frac{d}{dt} f(C(t)) \right|_{t=0} \quad (\text{A.5})$$

for any smooth function f . T is also denoted by d/dt . In the coordinate system x^μ , its components are given by $T^\mu = dx^\mu(t)/dt$ at point $C(t)$ with $x^\mu(t)$ the coordinate of $C(t)$. From the definition (Eq.(A.5)), the tangent vector measures the infinitesimal displacement along the curve $C(t)$.

Given any vector field v , it is always possible to find a smooth curve $\gamma(t)$ passing through a point p at which its tangent vector is v . Moreover, the curve is also unique. Therefore, any vector represents an infinitesimal displacement.

Covectors

A covector ω at a point p is also a linear map $\omega : V_p \rightarrow \mathbb{R}$, so that it maps any vector $v \in V_p$ to a real number $\omega(v) \in \mathbb{R}$. The collection of all covectors at p is also a vector space, called V_p^* , whose basis can be chosen in the following way. Choose a coordinate system (U_α, x^μ) covering p . The basis of V_p is thus $\{\partial_\mu\}$. Then, the ν -th basic covector of V_p^* is denoted as dx^ν and behaves as $dx^\nu(\partial_\mu) = \delta_\mu^\nu$. Therefore, an arbitrary covector ω can be written as

$$\omega = \omega_\mu dx^\mu, \quad (\text{A.6})$$

with ω_μ the μ -th component, and its action on v is

$$\omega(v) = \omega_\nu dx^\nu(v^\mu \partial_\mu) = \omega_\nu v^\mu dx^\nu(\partial_\mu) = \omega_\nu v^\mu \delta_\mu^\nu = \omega_\nu v^\nu. \quad (\text{A.7})$$

Tensors

A general tensor T is a linear map which takes as arguments vectors and covectors and outputs a real number. Formally, let v_1, \dots, v_k be vectors in V_p , and $\omega^1, \dots, \omega^l$ be covectors in V_p^* , then $T(v_1, \dots, v_k; \omega^1, \dots, \omega^l)$ is a number. Since T maps k vectors and l covectors to a number, T is called a (k, l) type tensor. The components of T is defined as

$$T_{\mu_1, \dots, \mu_k}^{\nu_1, \dots, \nu_l} \equiv T(\partial_{\mu_1}, \dots, \partial_{\mu_k}; dx^{\nu_1}, \dots, dx^{\nu_l}), \quad (\text{A.8})$$

in the coordinate system x^μ .

A.2 Invariant Operations: Lie Derivative & Covariant Derivative

The evolution of a physical quantity can be determined by solving a differential equation, which involves the concept of derivative. In GR, the general covariance requires that the derivatives should also transform invariantly. There are two kinds of invariant derivatives that are important: Lie derivative and covariant derivative.

A.2.1 Lie Derivative

A.2.1.1 Smooth Maps between Manifolds, Pushforward & Pullback

A smooth map ϕ between two manifolds \mathcal{M} and \mathcal{N} is such that the composition $\varphi_\beta \circ \phi \circ \psi_\alpha^{-1} : \psi_\alpha(U_\alpha) \rightarrow \varphi_\beta(V_\beta)$ is smooth, where (U_α, ψ_α) and (V_β, φ_β) are the coordinate chart of \mathcal{M} and \mathcal{N} , respectively. ϕ relates \mathcal{M} to \mathcal{N} . In particular, when

$\mathcal{M} = \mathcal{N}$, and ϕ is one-to-one and onto, ϕ defines a transformation on \mathcal{M} . For example, translating all points along x direction by one unit in the 3 dimensional Euclidean space \mathbb{R}^3 is such a smooth map on \mathbb{R}^3 . Rotation around z axis by angle θ is another example. It is interesting to study the action of ϕ on various types of tensors. In the following, p is a point in \mathcal{M} ; v, v_1, v_2 are vector fields on \mathcal{M} ; and ω a covector field on \mathcal{N} .

Action on scalars:

Let f be a scalar on \mathcal{N} , so the composition $f \circ \phi$ maps a point $p \in \mathcal{M}$ to $\phi(p) \in \mathcal{N}$ and further to $f(\phi(p)) \in \mathbb{R}$. This composition defines the *pullback* ϕ^* : $\phi^*f = f \circ \phi$. Thus, ϕ^*f is a scalar function on \mathcal{M} .

Action on vectors:

Let v be a vector field on \mathcal{M} . The *pushforward* ϕ_*v is given by $(\phi_*v)|_{\phi(p)}(f) = v|_p(\phi^*f) = v(f \circ \phi(p))$. So ϕ_*v is a vector field on \mathcal{N} .

Action on covectors:

Let ω be a covector field on \mathcal{N} . The *pullback* $\phi^*\omega$ is a covector field on \mathcal{M} such that $(\phi^*\omega)|_p(v) = \omega|_{\phi(p)}(\phi_*v)$.

Action on metric tensor:

The metric tensor g on \mathcal{N} can be pulled back to \mathcal{M} such that $(\phi^*g)|_p(v_1, v_2) = g|_{\phi(p)}(\phi_*v_1, \phi_*v_2)$.

If $\mathcal{M} = \mathcal{N}$, Lie derivatives of various types of tensor fields can be introduced. Given a smooth vector field v on \mathcal{M} , it is possible to construct a smooth map on \mathcal{M} : let p be a point in \mathcal{M} , then there exists a unique smooth curve $\gamma(t)$ passing through p , i.e., $\gamma(0) = p$, and whose tangent is v . A smooth map ϕ_t is thus defined as $\phi_t(p) = \gamma(t)$, i.e., it maps p to $\gamma(t)$ along the integral curve of v . For instance, in \mathbb{R}^3 , the translation along x direction by one unit is a smooth map induced by

the vector field $(1, 0, 0)$, and rotation around z axis is induced by $(y, -x, 0)$. Thus, ϕ_t can be viewed as a transformation induced by the vector field v .

Now, apply the transformation ϕ_t to \mathcal{M} , which carries any p to $\phi_t(p)$, and at the same time, any tensor T at p to corresponding tensor at $\phi_t(p)$, i.e., $\phi_{t*}T$. The Lie derivative of T along v can be defined as,

$$\mathcal{L}_v T = \lim_{t \rightarrow 0} \frac{T - \phi_{-t*}T}{t}. \quad (\text{A.9})$$

In the coordinate system x^μ , the Lie derivatives of different types of tensors are

$$\mathcal{L}_v f = v(f) = v^\mu \partial_\mu f, \quad (\text{A.10})$$

$$\mathcal{L}_v u = [v, u] = (v^\mu \partial_\mu u^\nu - u^\mu \partial_\mu v^\nu) \partial_\nu, \quad (\text{A.11})$$

$$\mathcal{L}_v \omega = (v^\mu \partial_\mu \omega_\nu + \omega_\mu \partial_\nu v^\mu) \partial_\nu, \quad (\text{A.12})$$

$$\mathcal{L}_v T_{\nu_1, \dots, \nu_l}^{\mu_1, \dots, \mu_k} = v^\rho \partial_\rho T_{\nu_1, \dots, \nu_l}^{\mu_1, \dots, \mu_k} - \sum_{i=1}^k T_{\nu_1, \dots, \nu_l}^{\mu_1, \dots, \rho, \dots, \mu_k} \partial_\rho v^{\mu_i} + \sum_{j=1}^l T_{\nu_1, \dots, \rho, \dots, \nu_l}^{\mu_1, \dots, \mu_k} \partial_{\nu_j} v^\rho. \quad (\text{A.13})$$

A.2.1.2 Killing vector fields

$\mathcal{L}_v T = 0$ implies $T = \phi_{t*}T$, in other words, v induces a symmetry transformation ϕ_t for T . Now, let $T = g$, then ϕ_t is called a *symmetry transformation* of the spacetime \mathcal{M} and v is called the *Killing vector field*. From now on, a Killing vector field is denoted as χ , and $\mathcal{L}_\chi g = 0$. A manifold usually does not have any Killing vectors. If it does, there are at most $n(n+1)/2$ linearly independent Killing vectors.

A.2.2 Covariant Derivative

The second invariant operation of importance is the covariant derivative ∇ , mapping a (k, l) type tensor to a $(k, l+1)$ type tensor. It satisfies the following properties:

1. Linearity: $\nabla(\alpha T + \beta S) = \alpha\nabla(T) + \beta\nabla(S)$, for $\alpha, \beta \in \mathbb{R}$, and tensors T, S are of the same type;
2. Leibniz rule: $\nabla(TS) = T\nabla(S) + \nabla(T)S$, for arbitrary tensors T, S ;
3. ∇ commutes with contraction;
4. Action on a function f : $\nabla f(v) = \nabla_v f = v(f)$, for any vector v .

The last property deserves explanation: Since f is of type (0,0), ∇f is of type (0,1), that is, a kind of covector, which acts on vectors. Property 4 implies the consistency with the notion of vector fields as directional derivatives on scalar functions. Applying ∇ again gives $\nabla\nabla f$, which is type (0,2) and takes two vectors v, u . $\nabla\nabla f(v, u)$ is not necessarily equal to $\nabla\nabla f(u, v)$. In GR, the torsion free condition is assumed, which is the fifth property of ∇ :

5. Torsion free: $\nabla\nabla f(v, u) = \nabla\nabla f(u, v) \Leftrightarrow \nabla_v\nabla_u f = \nabla_u\nabla_v f$.

In the more familiar component form, ∇ is written as ∇_μ and Properties 4 and 5 are expressed as

$$(\nabla_\mu f)v^\mu = v^\mu\partial_\mu f \quad \Rightarrow \quad \nabla_\mu f = \partial_\mu f, \quad (\text{A.14})$$

$$\nabla_\mu\nabla_\nu f = \nabla_\nu\nabla_\mu f. \quad (\text{A.15})$$

A manifold can possess several different covariant derivatives. The relation between two arbitrary derivatives ∇_μ and $\tilde{\nabla}_\mu$ is

$$\nabla_\mu\omega_\nu = \tilde{\nabla}_\mu\omega_\nu - C^\rho_{\mu\nu}\omega_\rho, \quad (\text{A.16})$$

with $C^\rho_{\mu\nu}$ a type (1,2) tensor. $\Gamma^\rho_{\mu\nu}$ is such a special case.

A.2.2.1 Lie derivatives in terms of ∇

In terms of ∇_μ , Lie derivatives can be rewritten by replacing ∂_μ by ∇_μ . For example, in component form,

$$\mathcal{L}_v u^\mu = [v, u]^\mu = v^\nu \nabla_\nu u^\mu - u^\nu \nabla_\nu v^\mu, \quad (\text{A.17})$$

$$\mathcal{L}_v \omega_\mu = v^\nu \nabla_\nu \omega_\mu + \omega_\nu \nabla_\mu v^\nu. \quad (\text{A.18})$$

Similarly, the Lie derivative of g is

$$\mathcal{L}_v g_{\mu\nu} = v^\rho \nabla_\rho g_{\mu\nu} + g_{\rho\nu} \nabla_\mu v^\rho + g_{\mu\rho} \nabla_\nu v^\rho = g_{\rho\nu} \nabla_\mu v^\rho + g_{\mu\rho} \nabla_\nu v^\rho, \quad (\text{A.19})$$

in which Eq.(2.15) has been used. If v is a Killing vector field χ , the above expression gives the Killing equation,

$$\mathcal{L}_\chi g_{\mu\nu} = g_{\rho\nu} \nabla_\mu \chi^\rho + g_{\mu\rho} \nabla_\nu \chi^\rho = 0 \quad \Rightarrow \quad \nabla_\mu \chi_\nu + \nabla_\nu \chi_\mu = 0. \quad (\text{A.20})$$

B Geodesic Congruences

B.1 Timelike geodesic congruence

Let $\{\gamma_s(\tau)\}$ represent a congruence of timelike geodesics parametrized by an affine parameter τ and labeled by s . The tangent $T^\mu = (d/d\tau)^\mu$ to $\gamma_s(\tau)$ satisfies $T^\mu \nabla_\mu T^\nu = 0$, and the vector $S^\mu = (d/ds)^\mu$ measures the deviation from $\gamma_s(\tau)$ to nearby geodesics, so it is called the deviation vector. The set $\{\gamma_s(\tau)\}$ is thus a smooth 2 dimensional surface with coordinates (τ, s) , so T^μ commutes with S^μ ,

$$T^\mu \nabla_\mu S^\nu - S^\mu \nabla_\mu T^\nu = 0. \quad (\text{B.1})$$

A reparametrization $\tau \rightarrow a(s)\tau + b(s)$ makes it possible to set $T^\mu S_\mu = 0$, which will be assumed in the following discussion. S^μ is thus called spatial relative to T^μ . In fact, when S^μ is spatial, a further reparametrization of $\gamma_s(\tau)$ will normalize all T^μ , i.e., $T^\mu T_\mu = -1$ for all s .

The variation of S^μ along $\gamma_s(\tau)$ describes how the nearby geodesics diverge or converge as time τ flows. The rate of the change in S^μ along $\gamma_s(\tau)$ is given by,

$$T^\nu \nabla_\nu S^\mu = S^\nu \nabla_\nu T^\mu. \quad (\text{B.2})$$

So the tensor $\nabla_\nu T^\mu$ plays an important role and is named $B_{\mu\nu}$:

$$B_{\mu\nu} = \nabla_\nu T_\mu. \quad (\text{B.3})$$

$B_{\mu\nu}$ is purely spatial: $T^\mu B_{\mu\nu} = B_{\mu\nu} T^\nu = 0$. As a rank 2 tensor, $B_{\mu\nu}$ can be decomposed into its trace ρ , traceless symmetric part $\sigma_{\mu\nu}$, and antisymmetric

part $\omega_{\mu\nu}$, in such a way that,

$$B_{\mu\nu} = \frac{1}{3}\rho h_{\mu\nu} + \sigma_{\mu\nu} + \omega_{\mu\nu}, \quad (\text{B.4})$$

where $h_{\mu\nu} = g_{\mu\nu} + T_\mu T_\nu$ is the induced metric on a hypersurface spanned by all deviation vectors.

Suppose $\sigma_{\mu\nu} = \omega_{\mu\nu} = 0$, then for any deviation vector S^μ ,

$$T^\nu \nabla_\nu S^\mu = \frac{1}{3}\rho h^\mu{}_\nu S^\nu = \frac{\rho}{3}S^\mu, \quad (\text{B.5})$$

since S^μ is spatial. This expression means that the rate of change in S^μ is uniform in all directions, so ρ is called the *expansion* of the geodesic congruence. If there is no expansion, and $\omega_{\mu\nu} = 0$, over a small time period $\Delta\tau$, the deviation vector S^μ changes according to

$$T^\nu \nabla_\nu S^\mu = \sigma^\mu{}_\nu S^\nu, \quad (\text{B.6})$$

and at a later time $\tau + \Delta\tau$ can be written as $\tilde{S}^\mu = S^\mu + \sigma^\mu{}_\nu S^\nu \Delta\tau$. Since $\sigma_{\mu\nu}$ is symmetric, it can be diagonalized with eigenvalues $\lambda_i, i = 1, 2, 3$. In the coordinate system which diagonalizes $\sigma_{\mu\nu}$, $\tilde{S}^i = S^i(1 + \lambda_i \Delta\tau)$ and therefore,

$$S^\mu S_\mu = S^i S_i = \frac{(\tilde{S}^1)^2}{(1 + \lambda_1 \Delta\tau)^2} + \frac{(\tilde{S}^2)^2}{(1 + \lambda_2 \Delta\tau)^2} + \frac{(\tilde{S}^3)^2}{(1 + \lambda_3 \Delta\tau)^2}. \quad (\text{B.7})$$

Here, the time component is not written explicitly because S^μ is spatial, and $S^\mu S_\mu$ is the original length squared and is positive. This expression shows that a space which is originally spherical ($\Delta\tau = 0$, so the denominators are all 1) will deform to an ellipsoid at $\Delta\tau$, whose volume is the same as that of the sphere. Because of this, $\sigma_{\mu\nu}$ is called the *shear*. Finally, if there is neither expansion, nor shear, consider

$$T^\nu \nabla_\nu (S^\mu S_\mu) = 2S^\mu T^\nu \nabla_\nu S_\mu = 2S^\mu S^\nu \omega_{\mu\nu} = 0, \quad (\text{B.8})$$

because $S^\mu S^\nu$ is symmetric, while $\omega_{\mu\nu}$ is antisymmetric. So $\omega_{\mu\nu}$ preserves the length of S^μ , and is called the *rotation*.

It is important to study how ρ varies along $\gamma_s(\tau)$. For this purpose, the first step is to calculate

$$T^\rho \nabla_\rho B_{\mu\nu} = T^\rho \nabla_\rho \nabla_\nu T_\mu = R_{\rho\nu\mu\sigma} T^\rho T^\sigma - B^\rho{}_\nu B_{\mu\rho}. \quad (\text{B.9})$$

Contracting the above equation with $h^{\mu\nu}$ gives Raychaudhuri's equation,

$$\frac{d\rho}{d\tau} = -\frac{\rho^2}{3} - \sigma_{\mu\nu}\sigma^{\mu\nu} + \omega_{\mu\nu}\omega^{\mu\nu} - R_{\mu\nu}T^\mu T^\nu. \quad (\text{B.10})$$

Another important relation is

$$\mathcal{L}_T h_{\mu\nu} = \mathcal{L}_T g_{\mu\nu} = \nabla_\mu T_\nu + \nabla_\nu T_\mu. \quad (\text{B.11})$$

Let $\rho_{\mu\nu} = B_{(\mu\nu)}$, i.e., the symmetric part of $B_{\mu\nu}$, then,

$$\rho_{\mu\nu} = \frac{1}{2} \mathcal{L}_T h_{\mu\nu}. \quad (\text{B.12})$$

B.2 Null geodesic congruence

Having considered timelike geodesic congruence, the null geodesic congruence can now be described and the corresponding Raychaudhuri's equation can be derived. The congruence of null geodesic can be affinely parametrized by v . The tangent to $\gamma(v)$ is denoted by $k^\mu = (d/dv)$. As previously, let η^μ be the deviation vector, and $\eta^\mu k_\mu = 0$. However, there exists a gauge transformation $\eta'^\mu = \eta^\mu + \alpha k^\mu$, which makes η'^μ also a valid deviation vector for an arbitrary number α , since $k^\mu k_\mu = 0$. This observation makes the introduction of $B_{\mu\nu}$ nontrivial.

Defining $B_{\mu\nu} = \nabla_\nu k_\mu$, the rate of change in η^μ is

$$k^\mu \nabla_\mu \eta^\nu = B^\nu{}_\mu \eta^\mu. \quad (\text{B.13})$$

Since $k^\mu B_{\mu\nu} = B_{\mu\nu} k^\nu = 0$, the rate of change in η'^μ is

$$k^\mu \nabla_\nu \eta'^\nu = B^\nu{}_\mu \eta'^\mu = B^\nu{}_\mu \eta^\mu. \quad (\text{B.14})$$

Therefore, as long as two deviation vectors differ by a multiple of k^μ , their rates of change along $\gamma(v)$ are the same. This means that $B_{\mu\nu}$ actually acts on the equivalent classes of deviation vectors, which are sets of deviation vectors differing from each other by a multiple of k^μ . Let η^μ and η'^μ be two vectors in an equivalence class denoted by $\hat{\eta}^\mu$. Define a new tensor $\hat{B}_{\mu\nu}$, such that for any $\hat{\eta}^\mu, \hat{\xi}^\nu$,

$$\hat{B}_{\mu\nu} \hat{\eta}^\mu \hat{\xi}^\nu = B_{\mu\nu} \eta^\mu \xi^\nu. \quad (\text{B.15})$$

In this way, the set of the equivalent classes $\hat{\eta}^\mu$ forms a 2 dimensional vector space, and $\hat{B}_{\mu\nu}$ is decomposed in the following way,

$$\hat{B}_{\mu\nu} = \frac{1}{2} \hat{\rho} \hat{h}_{\mu\nu} + \hat{\sigma}_{\mu\nu} + \hat{\omega}_{\mu\nu}. \quad (\text{B.16})$$

Similarly, $\hat{\rho}, \hat{\sigma}_{\mu\nu}$ and $\hat{\omega}_{\mu\nu}$ are called expansion, shear and rotation, respectively. $\hat{\rho}$ is also donated simply as ρ . $\hat{h}_{\mu\nu}$ is the induced metric of the 2 dimensional vector space, and positive definite. So in an orthonormal basis $\{\hat{x}^\mu, \hat{y}^\mu\}$, $\hat{h}_{\mu\nu} = \hat{x}_\mu \hat{x}_\nu + \hat{y}_\mu \hat{y}_\nu$.

The variation of $\hat{B}_{\mu\nu}$ along $\gamma(v)$ can also be derived,

$$k^\rho \nabla_\rho \hat{B}_{\mu\nu} = (\widehat{k^\rho \nabla_\rho B_{\mu\nu}}) = (\widehat{R_{\rho\nu\mu\sigma} k^\mu k^\nu}) - \hat{B}^\rho{}_\nu \hat{B}_{\mu\rho}. \quad (\text{B.17})$$

Contraction with $\hat{h}^{\mu\nu}$ gives the Raychaudhuri's equation,

$$\frac{d\rho}{dv} = -\frac{\rho^2}{2} - \hat{\sigma}_{\mu\nu}\hat{\sigma}^{\mu\nu} + \hat{\omega}_{\mu\nu}\hat{\omega}^{\mu\nu} - R_{\mu\nu}k^\mu k^\nu. \quad (\text{B.18})$$

Let K_0 be a 2 dimensional, compact and spacelike surface whose induced metric is $\gamma_{\mu\nu}$ and the coordinate system is $\{\theta, \phi\}$. Light rays emanating from K_0 will form a null geodesic congruence. Suppose all light rays in the congruence are normal to K_0 , then after a while, at parameter value v , all photons in the congruence will locate at a different compact surface K_v . It can be shown that the area A of K_v varies, depending on θ . Let the function u be constant on the null hypersurface generated by k^μ , therefore, $k^\mu \nabla_\mu u = 0$. Name $k_\mu = -\nabla_\mu u$ so that $k^\mu k_\mu = 0$. Extend v outside of the null hypersurface in order that $\nabla_\mu v$ is defined, then $k^\mu \nabla_\mu v = (\partial_v)^\mu \nabla_\mu v = 1$. Thus, call $l_\mu = -\nabla_\mu v$. Finally, let $l^\mu = (\partial_u)^\mu$. l^μ is a null vector, due to $l^\mu \nabla_\mu v = -l^\mu l_\mu = 0$. It is also required that l^μ is normal to K_v . Together with θ, ϕ, v, u form a coordinate system, in which the metric is given by

$$g_{\mu\nu} = -l_\mu k_\nu - k_\mu l_\nu + \gamma_{\mu\nu}, \quad (\text{B.19})$$

and therefore, $\hat{h}_{\mu\nu} = \gamma_{\mu\nu}$. On the one hand, $\mathcal{L}_k g_{\mu\nu} = \nabla_\mu k_\nu + \nabla_\nu k_\mu$ so that

$$\mathcal{L}_k \hat{h}_{\mu\nu} = \mathcal{L}_k \hat{g}_{\mu\nu} = 2\hat{B}_{\mu\nu}; \quad (\text{B.20})$$

on the other hand,

$$\mathcal{L}_k \hat{h}_{\mu\nu} = \mathcal{L}_k \gamma_{\mu\nu}. \quad (\text{B.21})$$

Then the conclusion is that

$$\rho = \frac{1}{2} \hat{h}^{\mu\nu} \mathcal{L}_k \hat{h}_{\mu\nu} = \frac{1}{2} q^{\mu\nu} \mathcal{L}_k \gamma_{\mu\nu} = \frac{1}{2} q^{\mu\nu} \frac{\partial \gamma_{\mu\nu}}{\partial v}, \quad (\text{B.22})$$

where $\hat{h}^{\mu\nu}$ ($q^{\mu\nu}$) is the inverse matrix of $\hat{h}_{\mu\nu}$ ($\gamma_{\mu\nu}$). Let $\det(\gamma_{\mu\nu}) = q$, then the expansion ρ is determined by

$$\rho = \frac{1}{2q} \frac{\partial q}{\partial v} = \frac{1}{\sqrt{q}} \frac{\partial \sqrt{q}}{\partial v}. \quad (\text{B.23})$$

Integrating both sides over the surface K_v gives how fast the area changes,

$$\frac{dA}{dv} = \oint_{K_v} \frac{\partial \sqrt{q}}{\partial v} d\theta d\phi = \oint_{K_v} \rho \sqrt{q} d\theta d\phi. \quad (\text{B.24})$$

Therefore, if $\rho > 0$, K_v will expand, but if $\rho < 0$, K_v will shrink, instead.